A FRAMEWORK FOR MODELING DISCRETE DEFORMATION TWINNING IN HEXAGONAL CRYSTALS

A Dissertation

Presented to the Faculty of the Graduate School

of Cornell University

in Partial Fulfillment of the Requirements for the Degree of

Doctor of Philosophy

by

Matthew P. Kasemer

August 2018

A FRAMEWORK FOR MODELING DISCRETE DEFORMATION TWINNING IN HEXAGONAL CRYSTALS

Matthew P. Kasemer, Ph.D.

Cornell University 2018

Modeling the plastic deformation of metals has historically been achieved by considering only crystallographic slip, the dominant mode of plastic deformation. While sufficient for materials that deform primarily by means of slip, many metals may exhibit other modes of plastic deformation, and thus may not be accurately modeled by slip alone. Deformation twinning is another mode of plastic deformation, characterized by a rapid, large uniform shear of a discrete region of material, coupled with a reorientation of the crystal lattice within said region. While witnessed in metals of various crystal symmetries, metals comprised of hexagonal crystals are especially prone to exhibit twinning, as they may require twinning to accommodate generalized plasticity. Due in large part to limitations in computational capabilities, models have often ignored deformation twinning. Existing models rely on the homogenization of the responses due to both slip and twinning via a modified Taylor hypothesis, and thus fail to predict accurate local states. Additionally, these models consider twin systems as modified slip systems, obscuring the discrete nature of deformation twinning, as well as the disparity in relative speeds at which each deformation mode propagates. Advances in computational capabilities and model frameworks have allowed for the possibility to study this deformation mode in more detail. A parallelized finite element framework is uniquely suited to approach this problem, as a proven platform for modeling high fidelity, finely discretized representations of polycrystalline aggregates. A framework is presented, in which grains within a microstructure are pre-discretized - based on their crystallographic orientation -

into discrete regions that may deform by deformation twinning. A boundary value problem is solved, in which the displacement of the nodes within a twin region are rapidly mapped to their twinned location, the region's crystal lattice is reoriented via three separate schemes, and the remainder of the body deforms by means of crystallographic slip to accommodate this deformation. In this way, the extended framework retains the characteristic differences between crystallographic slip and deformation twinning in a way that existing models do not. Work is calculated due to the changes in local environments due to twinning. Changes in local stress states are discussed in light of global and local work measures and various parameters, including twin size and reorientation schemes.

BIOGRAPHICAL SKETCH

Matthew Kasemer attended the Rochester Institute of Technology in Rochester, New York, during which time he was an undergraduate researcher in solid mechanics at NASA Glenn Research Center. He graduated with a bachelor's degree in mechanical engineering with highest honors in 2012. He later earned a master's degree in mechanical engineering from Cornell University in 2015.

Dedicated to my partner, Erin, and my parents, Lynne and Greg.

ACKNOWLEDGEMENTS

Romain Quey of the École des Mines de Saint-Étienne provided me with an immense amount of support over various projects, and was instrumental in allowing for the work presented here (and much more) to come to fruition. I would also like to thank Jean-Charles Stinville, McLean Echlin, and Tresa Pollock of the University of California, Santa Barbara for sharing and explaining experimental data (heavy emphasis on the latter). Every meeting with them was provoking and fruitful, and overall they were generous collaborators. Additionally, the past and present members of the Deformation Processes Laboratory at Cornell University - including Robert Carson, Kamalika Chatterjee, Andrew Poshadel, Euan Wielewski, Darren Pagan, Mark Obstalecki, and Christopher Budrow - assisted me with a considerable amount of their time with debugging code, discussions of theory, implementation, and results, and general suggestions. The majority of my time as a graduate student was funded by the Cornell High Energy Synchrotron Source (CHESS) under NSF award DMR-1332208, and funding for portions of the work presented here was supported by the Office of Naval Research under grants N00014-12-1-0399 and N00014-16-1-2982. I would also like to thank my minor committee members, Matt Miller and Shefford Baker, for their thoughtful suggestions. Most importantly, many thanks to my committee chair, Paul Dawson, for successfully balancing the roles of advisor and mentor - affording me a rich and fulfilling tenure as a graduate student. Being a student under Paul's guidance was truly a pleasure.

TABLE OF CONTENTS

LIST OF TABLES

LIST OF FIGURES

CHAPTER 1

INTRODUCTION

Metals are the primary material used in engineering applications. Understanding their deformation response when subjected to loading is crucial in the design of materials, the design of manufacturing processes, and the design of engineering components [75]. Metals, however, are often complex materials with complex behaviors, and understanding their deformation responses is non-trivial [51, 65]. Primarily, heterogeneity in terms of a material's microstructure, as well as complex deformation responses by single crystals [28, 84], contribute to limited understanding of both the elastic and plastic responses of metals. In light of these characteristics, predicting deformation responses of metals quickly becomes unmanageable without the aid of mathematical models [86, 17]. Simulating the deformation of materials by representing their microstructures provides insight into the development of plasticity at the crystal scale [129, 85, 131], and the influence that both the microstructure and the crystal behavior have on the resulting macroscopic behavior [99]. Understanding the microstructure-property relationship of polycrystalline metals is best achieved through the use of sophisticated crystal scale finite element simulations performed on high-fidelity representations of microstructures.

Metallic single crystals may appear in many different atomic configurations, chiefly crystals that exhibit either cubic or hexagonal symmetry. Hexagonal close packed crystals are especially interesting due to their propensity to both appear in high strength structural metals (such as titanium alloys [75]), as well as exhibit a relatively high degree of anisotropy in terms of their elastic and plastic responses [126, 33, 56, 111, 18, 49, 128, 136]. Metals deform plastically primarily by means of crystallographic slip. Slip is a spatially diffuse, spatially heterogeneous mode of deformation [131], which propagates at a rate determined by the local environment, and can cause shear of an

arbitrary magnitude.

While the plastic deformation response of crystals exhibiting cubic symmetry is often successfully modeled using only a single family of crystallographic slip systems, hexagonal crystals often require multiple sets of slip systems to accommodate generalized plastic deformation [84]. The plastic behavior of many hexagonal crystals is debated - while the plastic behavior of hexagonal crystals is widely accepted to be anisotropic, debate centers on the relative strength between slip system families. Similarly, the description of the elastic response of a single hexagonal crystal requires more parameters than cubic crystals, and it is often difficult to accurately quantify single crystal elastic constants [126]. Deformation responses will vary depending on both the initial relative strengths, as well as the elastic moduli [60, 33]. As such, metals comprised of hexagonal crystals are difficult to model, and require robust experimental data to inform the model [127, 39, 61].

Lending to even further complexity, hexagonal crystals (and indeed crystals of other symmetries) may exhibit other modes of plastic deformation in addition to crystallographic slip [28, 84, 51]. Deformation twinning is a distinct mode of inelastic deformation characterized by the defined, uniform shear of a volume of material, coupled with a reorientation of the crystal lattice within the volume, which forms nearly instantaneously [26, 97]. This is in direct contrast to slip, which is spatially diffuse, has no large lattice reorientation, and propagates at a rate several orders of magnitude slower than twinning. Upon activation, the appearance of a twin has the potential to quickly change local stress states in the vicinity of the twin, as large deformation occurs coupled with the introduction of new grain boundaries (twin boundaries) [99, 130]. The introduction of new boundaries and reorientation of the crystal lattice could have effects upon the strength and ductility of the aggregate at large [97]. Simply put, deformation twinning

is vastly different from crystallographic slip in nearly every respect.

Twinning has largely been ignored in deformation models for a variety of reasons, including the propensity of most metals to deform mainly by slip and the lack of robust experimental data. Primarily, however, limitations in computational capabilities have hindered the development of computationally intensive models. The discrete nature of twins were historically difficult to represent, as models did not spatially resolve single crystals. Additionally, the presence of two deformation modes with disparate time scales renders a system analogous to a stiff differential equation [90, 116], lending to further computational complexity. This has resulted in the development of models which trade away the prediction of local responses to instead focus on accurate prediction of bulk responses [52, 119, 58]. Historic material modeling employed the Taylor hypothesis, which considered each material point to represent many single crystals [8, 88]. The response at each material point would be calculated using a homogenization technique, considering the various crystal responses at that point. Relatively recent modeling developments have led to less use of homogenization techniques in favor of fine discretization of the microstructure, such that discrete grains are modeled [12, 137, 93]. This allows for the study of heterogeneous intragrain deformation fields.

Various attempts have been made to create models to predict the deformation response due to twinning. Chief among them, models which consider twinning as a "pseudo-slip" system have emerged as the primary method to represent twinning as a deformation mode [58, 113]. Twin systems are considered at each material point as additional slip systems. The model homogenizes the deformation at a material point due to both slip and twinning by considering the "volume fractions" of the material assumed to be deforming by either deformation mode (that is, a homogenization parameter determining the contribution of each deformation mode toward the total deformation

response). While reportedly successful in predicting bulk responses such as texture evolution and volume fractions of regions that have twinned, the model fails at accurately predicting fine local deformation fields. Considering a twin system in a similar way to how slip is modeled obscures the physical differences between the two - namely by ignoring the discrete nature of twinning, and the relatively high shear rates associated with twinning. The ability to discretize a grain into multiple elements - and thus the abandonment of homogenization techniques in these types of simulations - has led to this class of model being employed beyond its intended scope.

Recent strides in both experimental and computational capabilities have afforded researchers the ability to study deformation twinning more deeply [121, 14, 123]. Experimentally, developments in high energy X-ray diffraction have facilitated the ability for the appearance of twins to be witnessed *in situ*. The development of fast digital detectors has allowed for the precise measurement of diffraction peaks associated with different grains within a microstructure [41, 85], and the ability to track crystals which may be twins associated with other crystals [120, 121]. The recent advent of high energy diffraction microscopy, or "near field" diffraction, allows for a non-destructive mapping of a material's microstructure [73, 123, 2]. In conjunction with one another, and expected advancement in both techniques, experimental observation and understanding of deformation twinning are likely to accelerate [120, 123, 2, 3].

Computational capabilities have increased such that the fidelity of microstructural representations has allowed for fine microstructural features to be represented [93]. Grains are now commonly discretized into many elements, which allows for complex local heterogeneous deformation to be studied [131, 61]. Instantiation methods have similarly been developed to rapidly and reliably instantiate and mesh these aggregates [93, 94, 92]. Crystal scale finite element frameworks [78, 77] have advanced to be both

fast and reliable - as parallelization of code has allowed for much larger simulations to be run, and confidence in existing models has grown with respect to their ability to model plastic deformation by means of crystallographic slip [60]. Indeed, the majority of contemporary simulations of the deformation of crystalline solids are performed using crystal plasticity models on three-dimensional representations of microstructures [99] - a departure from simulations performed even as late as the mid 2000s, where models were often simplified [8, 88], and microstructural representations were either low fidelity [129] or reduced to relatively small material volumes [12].

1.1 Overview of Discrete Deformation Twinning Framework

Computational increases have afforded the opportunity to approach the problem of deformation twinning in a manner previously hindered by hardware capabilities, which led to significant modeling assumptions. The focus of this dissertation is to represent deformation twinning in a fundamentally different way than the most prevalent existing modeling effort - the pseudo-slip scheme - so as to maintain distinct characteristic differences between deformation twinning and crystallographic slip. To reiterate, the pseudo-slip scheme obscures the differences between crystallographic slip and deformation twinning by ignoring twinning's discrete nature and relatively high shear rate. The framework proposed in this study intends to utilize recent computational advancements to more accurately represent deformation twinning by focusing on maintaining these fundamental differences between crystallographic slip and twinning. By eschewing the current assumptions employed in the modeling of deformation twinning, this novel framework allows for the study of reactions of neighboring regions due to deformation twinning, as well as a test bed for approaching the questions of twin nucleation and growth. Specifically, this study focuses on the pre-discretization of a three dimen-

sional polycrystalline aggregate into regions which may be considered for twinning. Motion due to twinning is considered by mapping the nodal points contained within a discrete twin region to their expected twinned location at a relatively rapid rate. In these ways, twinning is more accurately represented than in existing modeling efforts, as the main characteristic differences between crystallographic slip and deformation twinning are maintained.

To accommodate the discrete nature of deformation twins, polycrystalline aggregates are pre-discretized into lamellar regions that may be considered for twin activation at some point during deformation. To achieve this, a domain representing a sample is discretized into grains, as shown in Figure 1.1(a) (for sake of simplicity, a two dimensional sample is illustrated, though the concept is generalized for three dimensions). Grains may then be further discretized into lamellar regions (Figure 1.1(b)) utilizing recent instantiation methods developed in a previous study [61]. Lamellar regions are oriented to represent twin regions by considering the crystallographic orientation of a grain, as well as the twin system in question. A robust finite element mesh is generated (Figure 1.1(c)) for the entire aggregate, including sub-grain lamellar features. Thus, discrete regions that may be considered for deformation twinning are explicitly represented, allowing for the simulated motion of discrete twin regions, rather than considering twinning as an auxiliary slip system and homogenizing the local deformation response.

The instantiation of discrete regions considered for twinning and the construction of an attendant finite element mesh allow for the mapping of the nodal coordinates to their expected twinned locations. At some point in deformation, a twin region is considered for activation, and it's elements and nodes identified (Figure 1.2(a)). With knowledge of the crystallographic orientation of the crystal, along with the twin system in question,

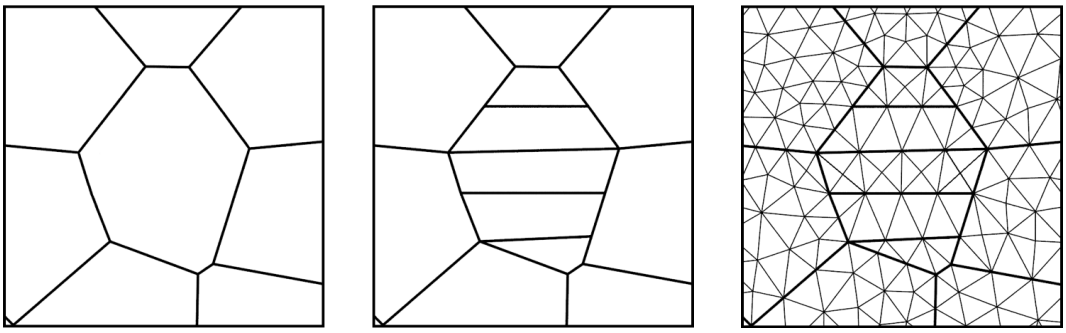

(a) (b) (c)

Figure 1.1: Illustrations depicting a two dimensional sample (a) discretized into grain structures, (b) further discretization of a single grain into lamellar sub-grain structures, and (c) attendant finite element mesh of the geometry including lamellar sub-grain structures.

the shear direction and amount of shear is known. Boundary conditions in the form of velocities are temporarily applied at the nodal points within a twin region (Figure 1.2(b)). Velocities are chosen such that the shear rate for the twin region is several orders of magnitude faster than shear rates typically associated with slip. For chosen velocities, an appropriate time step is calculated such that nodal points are mapped to their expected twinned locations (Figure 1.2(c)), and the surrounding regions react to the twin event by deforming via crystallographic slip. Here, the proposed framework differs from existing modeling efforts in that twins are considered as discrete sub-grain features rather than considered at material points, and the large relative differences in shear rates between slip and twinning is maintained, rather than obscured in a homogenization scheme.

In summary, the proposed framework aims to extend beyond the assumptions employed in current deformation twinning modeling efforts by focusing on both the insertion of discrete twins within a polycrystalline aggregate and maintaining relative rate differences between slip and twinning. A crystal plasticity finite element framework is utilized, and is uniquely suited to handle the problem of deformation twins due to both the ability to represent discrete twin regions, and to map nodal points due to twin

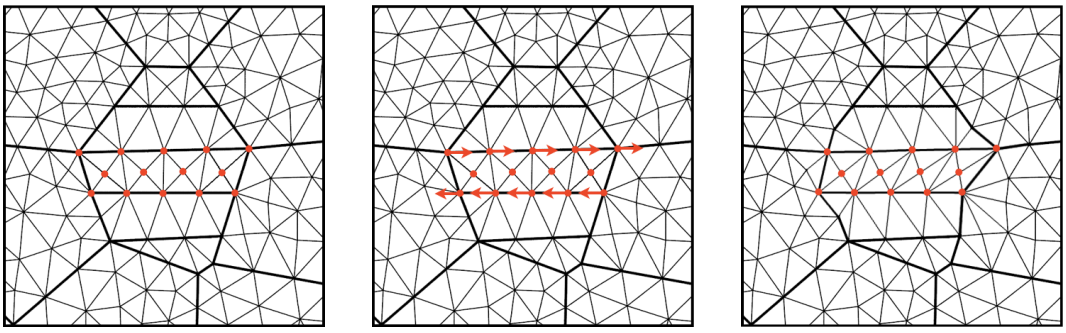

(a) (b) (c)

Figure 1.2: Illustrations depicting the (a) identification of mesh features within a twin region, (b) velocity boundary conditions applied at nodes, and (c) nodes of twin region mapped to expected twinned locations.

motion. Regions which may deform by twinning are represented in high fidelity polycrystalline aggregates by discretizing grains into lamellar regions. This is in contrast to existing methods, which simply homogenize the deformation responses due to crystallographic slip and twinning at local material points, failing to accurately represent the discrete character of twins. Motion due to twinning is achieved by mapping the nodal points of the twin region to their expected positions over a relatively short time period, and reorienting the crystal lattice within the twin region, while the surrounding regions accommodate this deformation by considering only crystallographic slip. Again, this is in contrast to existing methods, as the proposed framework maintains discrete motion mapping and relative rate disparity, which are both obscured in traditional homogenization schemes. Additionally, the wholesale reorientation of a discrete region of material essentially creates a new grain within the aggregate. This changes the spatial distribution of grains and introduces new grain to grain interactions which are known to influence the development of plasticity in an aggregate [11, 61].

By considering discrete twins, the framework allows for the detailed study of global and local effects on the deformation of a polycrystalline aggregate due to the onset of twinning. The reaction of surrounding regions due to the imposed motion of the twin re-

gion is calculated, and changes of local deformation fields around the vicinity of a twin region may be studied. Additionally, global and local energetic metrics - such as the total and plastic work due to twinning - may be calculated. The framework also serves as a testbed for studying twin nucleation and growth, and even provides an approach to the problem of transformation induced plasticity. Existing modeling methods, by considering deformation twinning as a pseudo-slip system and homogenizing the response at material points due to both deformation modes - obscures the characteristic differences between the two modes, and eliminates the possibility of studying similar phenomena in a way that the proposed framework affords.

In the following chapter (Chapter 2), background of crystallographic slip, deformation twinning, and material modeling is discussed, including existing efforts to model deformation twinning. Extension of the framework to include the ability to include discrete deformation twins is then outlined (Chapter 3), followed by results of key simulations (Chapter 4), a discussion of the results (Chapter 5), and future extensions of this study (Chapter 6). A full description of the finite element implementation may be found in Appendix A. This is followed by two studies which confirm both the validity of the existing framework with respect to crystallographic slip, as well as highlight the ability to model heterogeneous intragrain deformation (Appendices B and C), and Appendix C additionally contains a description of the instantiation method used in this study.

CHAPTER 2

BACKGROUND

This chapter is devoted to defining modes in which crystals may deform, and formalizing the terminology and methodology used and discussed in subsequent chapters. While twinning is observed in crystals of various symmetries, due to the propensity for hexagonal crystals to exhibit twinning, focus is given to hexagonal crystals over other crystal types. Discussions herein will be almost exclusively devoted to crystals exhibiting hexagonal symmetry. However, it should be noted that the theory discussed in this chapter - in general - is not limited to hexagonal crystals, and the extended framework described later in this study is not unique to any crystal type. Here, formalism related to crystallographic slip and deformation twinning in hexagonal crystals is defined. This is followed by an overview of some experimental observations of twinning and descriptions of physical character. Finally, a full description of the crystal plasticity finite element framework employed and extended in this study is presented, as well a description of the current popular method for modeling deformation twinning.

2.1 Deformation of Hexagonal Crystals

2.1.1 Slip and Twin Formalism

When a load is applied to crystals, the body at first deforms elastically - that is, the atomic lattice stretches such that the distance between atoms changes, but their location within the lattice stays the same. In the elastic regime, when load is decreased, the atoms return to their original relative order and spacings. As load is increased, however, the lattice will reach a point at which it will no longer continue to stretch, and the atoms'

positions in the lattice may change irreversibly, such that when the load is removed, the atoms no longer return to their original position. Plastic deformation of crystalline solids is often described by crystallographic slip. Figure 2.1(a) depicts a single crystal, with an enlarged view of a generic atomic lattice. When a load is applied, and the lattice can no longer accommodate elastic deformation, slip shifts the registry between crystallographic planes as depicted in Figure 2.1(b). The atomic positions shift, and the material above the slip plane shifts accordingly to accommodate the shape change due to deformation. Note that slip is spatially diffuse - in that it can occur anywhere within the crystal - and the magnitude of slip is not constrained.

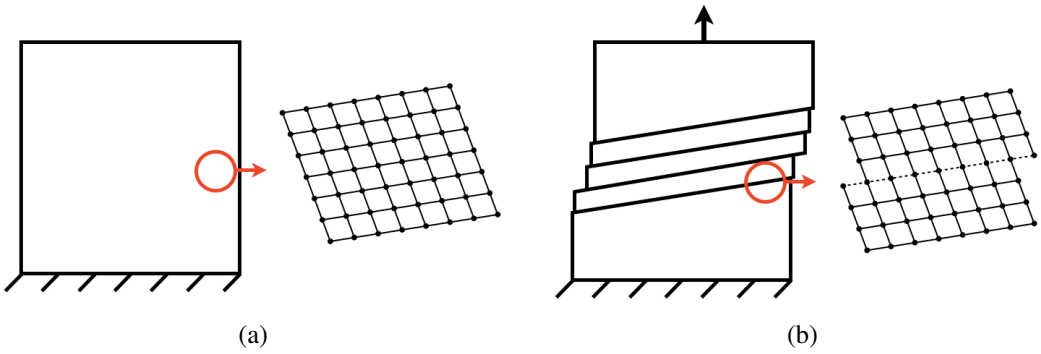

Figure 2.1: Illustrations depicting (a) a single crystal and an enlarged depiction of a generic lattice, and (b) crystallographic slip.

Plastic deformation is an isochoric process. In general, six strains are necessary to describe a strain state, though the isochoric constraint reduces the number of independent strains to five. Thus, to allow for generalized plasticity - that is, the ability to describe any shape change - a total of five linearly independent slip systems are necessary [51]. In crystals exhibiting hexagonal symmetry, three families of slip systems are often considered to meet this requirement. The most common families considered are the basal, prismatic, and pyramidal slip systems, illustrated in Figure 2.2. The basal and prismatic slip systems are referred to as $\langle a \rangle$-type slip systems - as they allow the crystals to slip only in the direction of one of the $\langle a \rangle$ axes. Similarly, pyramidal slip systems

are referred to as $\langle c + a \rangle$-type slip systems, as they allow for slip in a direction with a component aligned with the $\langle c \rangle$-axis. Slip systems are often described by the direction of slip, $\langle h\,k\,i\,l \rangle$, and the plane on which slip occurs, $\{h\,k\,i\,l\}$, using the Miller-Bravais notation (summarized in Table 2.1).

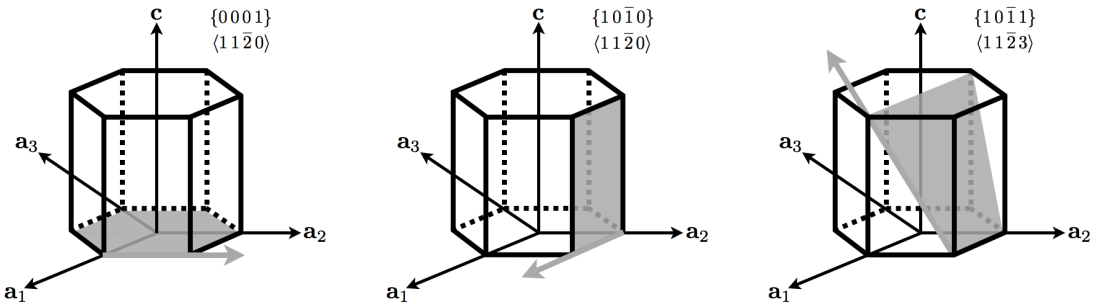

Figure 2.2: Primary slip systems of hexagonal close packed crystals.

Slip System Name	Number of Systems	m	s
Basal	3	$\{0\,0\,0\,1\}$	$\langle 1\,1\,\bar{2}\,0 \rangle$
Prismatic	3	$\{0\,0\,\bar{1}\,0\}$	$\langle 1\,1\,\bar{2}\,0 \rangle$
Pyramidal	12	$\{0\,0\,\bar{1}\,1\}$	$\langle 1\,1\,\bar{2}\,3 \rangle$

Table 2.1: Primary slip systems of hexagonal close packed crystals.

Each slip family has an associated slip strength - that is, a point at which slip is activated. Slip is commonly observed on $\langle a \rangle$-type slip systems due to their ease of activation (low strength). In some hexagonal close packed crystals, the $\langle c + a \rangle$-type systems may be difficult to activate due to a relatively high strength [75]. This relegates slip to directions perpendicular to the $\langle c \rangle$-axis, thus inhibiting general plastic deformation if only slip is considered. In these metals, deformation twinning may be observed.

Figure 2.3 illustrates a single crystal specimen undergoing deformation twinning. Note the difference between this mode of deformation and that of slip. Firstly, while the deformation associated with slip occurs between single lattice planes, in twinning, some volume of the material experiences a uniform shear (the "twin") whereas the rest of the

material remains undeformed (the "parent"). Next, the crystal lattice experiences a large reorientation in the volume that has sheared due to deformation twinning so as to mirror across the twin plane. Additionally, the magnitude of twinning is fixed, such that each twin experiences the same shear of a defined magnitude, while slip is unconstrained in this measure. Not illustrated is the fact that the shear rate due to twinning is much faster than that due to slip [99].

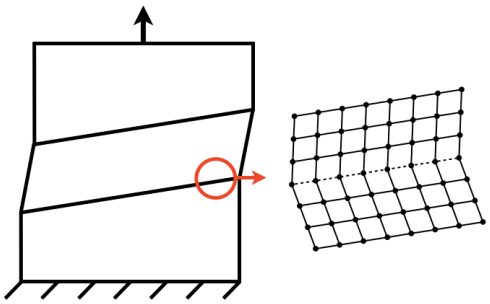

Figure 2.3: Illustration of a single crystal deforming by twinning.

Twin systems allow for the necessary deformation in the direction of the crystal $\langle c \rangle$-axis [75, 20] (representative examples shown in Figure 2.4). Similar to slip systems, twin systems may be broadly described by the direction of twin shear, $\langle h\,k\,i\,l \rangle$, and the plane on which shearing occurs, $\{h\,k\,i\,l\}$.

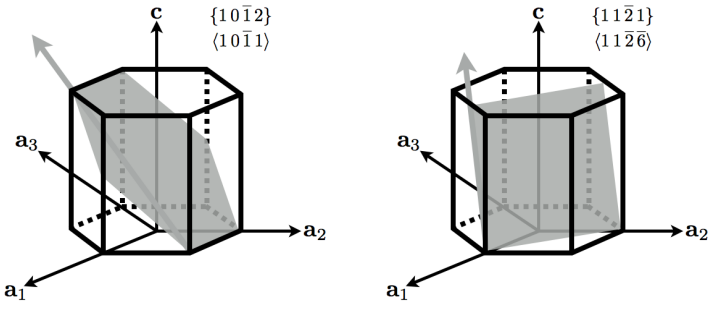

Figure 2.4: Primary twin systems of hexagonal close packed crystals.

In addition to the direction of twin shear and the twin plane (in general, η_1 and K_1,

respectively), twins may also be described in terms of a second undeformed plane (K_2 in the configuration pre-twinning, K_2' in the configuration post-twinning), a direction perpendicular to the first undeformed plane on the second undeformed plane (η_2 and η_2' in similar configurations), their width, w, and the shear magnitude, S. These planes and directions are illustrated for a generic twin in Figure 2.5. Full descriptions of the twin systems illustrated in Figure 2.4 in terms of these planes and directions are given in Table 2.2.

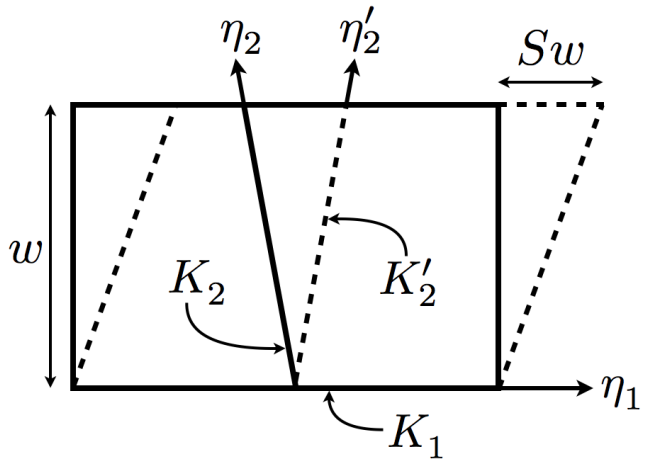

Figure 2.5: Illustration of generic twin deformation.

K_1	η_1	K_2	η_2	S
$\{1\,0\,\bar{1}\,2\}$	$\langle 1\,0\,\bar{1}\,\bar{1}\rangle$	$\{\bar{1}\,0\,1\,2\}$	$\langle 1\,0\,\bar{1}\,1\rangle$	0.167
$\{1\,1\,\bar{2}\,1\}$	$\langle 1\,1\,\bar{2}\,\bar{6}\rangle$	$\{0\,0\,0\,1\}$	$\langle 1\,1\,\bar{2}\,0\rangle$	0.638

Table 2.2: Description of primary twin systems of hexagonal close packed crystals.

Descriptions of this reorientation are often grouped into two main descriptions - so called twins of the first kind and twins of the second kind [97]. A twin of the second kind description is described as a 180° rotation of the crystal lattice about the twin shear direction, and is extremely rare (witnessed in uranium and low symmetry geological materials [22, 97]). Focusing on the twin of the first kind description, the reorientation

of the lattice is described as a 180° rotation of the crystal lattice about the twin plane normal - or, in other words, a reflection across the twin plane. Figure 2.6 depicts the parameters necessary to describe a twin of the first kind as well as the undeformed planes depicted in Figure 2.5.

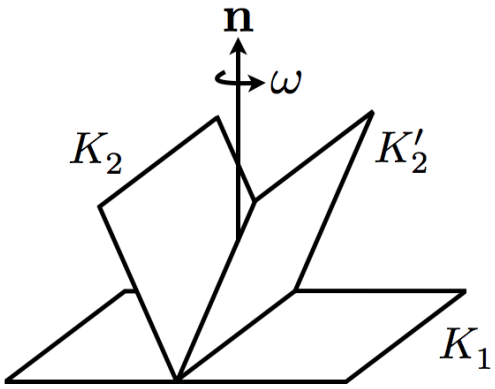

Figure 2.6: Illustration of a twin of the first kind.

The reorientation of the crystal lattice due to twinning may be very large. For hexagonal titanium crystals, twinning on the $\{1\,0\,\bar{1}\,2\}$ system produces a reorientation such that the $\langle c \rangle$-axes of the parent and twin crystal deviate by ~85° (see: Chapter 4.2). That is, a crystal originally with it's $\langle c \rangle$-axis aligned with the loading direction, upon twinning, reorients such that it's $\langle c \rangle$-axis is nearly perpendicular to the loading direction. This substantial reorientation of the crystal lattice has the potential to markedly effect the local response of the material. Figure 2.7 depicts the directional modulus of the hexagonal phase of Ti-6Al-4V as a function of the deviation of the crystal's $\langle c \rangle$-axis from the loading direction [51, 60].

Consider a crystal with its $\langle c \rangle$-axis aligned with the loading direction, which has a directional modulus of ~170GPa. Upon twinning, the crystal reorients such that it's directional modulus is much lower, only ~120GPa. Additionally, while the parent crystal is - in this case - unfavorably aligned for crystallographic slip on the weak basal and

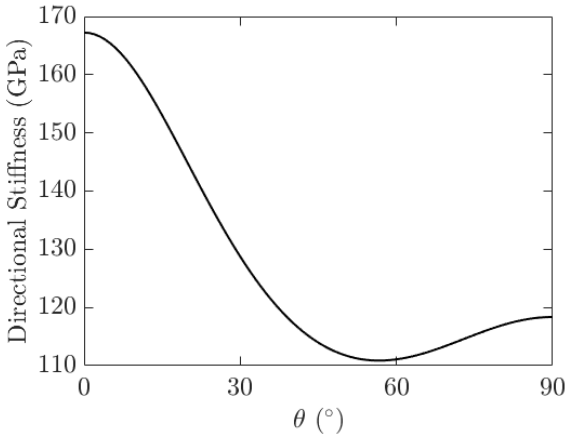

Figure 2.7: Directional modulus of the α phase of titanium alloy Ti-6Al-4V.

prismatic planes, the twinned crystal is favorably aligned for slip on the prismatic slip systems. The disparate behavior of the twinned crystal with respect to it's parent, however, will depend on a number of factors - mainly the parent crystal's orientation, twin system, crystal $\frac{c}{a}$ ratio, degree of elastic anisotropy, and degree of plastic anisotropy in terms of crystallographic slip.

2.1.2 Orientation Formalism

Hexagonal crystals are anisotropic - meaning a crystal's deformation response is dependent on the direction of loading. As such, a consistent method for describing a crystal's orientation with respect to some fixed reference is advantageous. Crystallographic orientation is often represented as a rotation to bring to bring one reference frame into coincidence with another. This rotation may be described by a rotation matrix constructed from the basis vectors of the sample frame, **e**, and the basis vectors for the crystal frame,

$\mathbf{e}'$, as:

$$\mathbf{R}_{ij}^{C,S} = \mathbf{e}_i \cdot \mathbf{e}'_j = \begin{bmatrix} \mathbf{e}_1 \cdot \mathbf{e}'_1 & \mathbf{e}_1 \cdot \mathbf{e}'_2 & \mathbf{e}_1 \cdot \mathbf{e}'_3 \\ \mathbf{e}_2 \cdot \mathbf{e}'_1 & \mathbf{e}_2 \cdot \mathbf{e}'_2 & \mathbf{e}_2 \cdot \mathbf{e}'_3 \\ \mathbf{e}_3 \cdot \mathbf{e}'_1 & \mathbf{e}_3 \cdot \mathbf{e}'_2 & \mathbf{e}_3 \cdot \mathbf{e}'_3 \end{bmatrix} \tag{2.1}$$

This rotation is in a "crystal-to-sample" convention, in which the constructed rotation is one that brings the crystal frame into the fixed sample reference frame. The function of this rotation is visually represented in Figure 2.8, in which two orthonormal bases are shown with the rotations necessary to bring each into coincidence with one another. Here, the superscript "C, S" denotes a rotation which brings a crystal reference frame into coincidence with a fixed sample reference frame, while "S, C" performs the opposite operation.

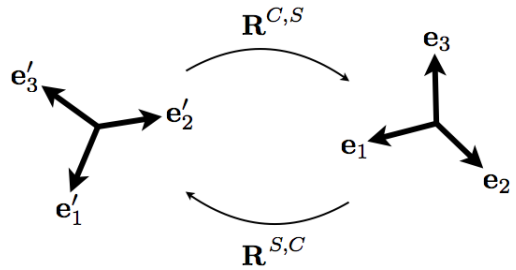

Figure 2.8: Illustration of a transformation from the crystal basis to a fixed reference basis.

Orientations may be alternatively described using angle-axis parameterizations [43]. Angle-axis parameterizations represent rotations by considering an axis of rotation, and a rotation about that axis (an example is shown above in Figure 2.6). Of the existing angle-axis parameterizations, quaternions and Rodrigues' vectors are perhaps the most useful for crystallography and twinning in some respects. First, the Rodrigues' parameterization is described as:

$$\mathbf{r} = \tan\left(\frac{\omega}{2}\right)\mathbf{n} \tag{2.2}$$

where $\mathbf{n}$ is the axis which the body is being rotated about, and ω is the amount of

rotation. Rodrigues' vectors are useful in plotting orientation distribution functions in orientation space. While Rodrigues' space is infinite, a fundamental region may be defined which bounds all unique orientations for a given crystal symmetry. Additionally, these fundamental regions are bounded by planes, unlike orientation spaces for Euler angles (see [43, 70]). Finally, a crystallographic fiber - that is, the set of orientations with a specific crystallographic direction aligned with a specific sample direction - is represented by a line in Rodrigues' space.

A quaternion is a four dimensional unit vector defined as:

$$\mathbf{q} = \begin{Bmatrix} q_0 \\ \mathbf{q}_n \end{Bmatrix} = \begin{Bmatrix} \cos\left(\frac{1}{2}\omega\right) \\ \sin\left(\frac{1}{2}\omega\right)\mathbf{n} \end{Bmatrix} \tag{2.3}$$

Quaternions are advantageous due to the ease in finding products of multiple rotations, as well as the fact that quaternion orientation space is finite (limited to the surface of a four-dimensional sphere).

Descriptions of conversions between many orientation parameterizations - including rotation matrices, Rodrigues' vectors, and quaternions - are summarized in [100].

2.1.3 Deformation Twinning Observations

Deformation twinning has been witnessed experimentally in a wide variety of metals [26], including cubic metals [24, 98, 110, 108] and hexagonal metals [21, 102, 124, 5, 138, 135, 123]. Twinning was historically witnessed primarily in crystals exhibiting hexagonal symmetry. Cubic crystals were thought not to experience deformation twinning until the mid-1960s [97], when a number of researchers witnessed the formation of twins in face centered cubic crystals [24, 98], and continued work has reaffirmed the crystal's ability to deform by twinning [110, 108]. Body centered cubic crystals may

also exhibit twinning [48], though it is often observed at very low temperatures [97, 99]. Twinning has also been observed in other materials (such as geologic materials), or crystals exhibiting lower symmetry (e.g., orthorhombic uranium [22]).

For decades, researchers have utilized a number of techniques to witness twins - including optical microscopy [96, 6], transmission electron microscopy [48, 79], electron backscatter diffraction [124, 14], neutron diffraction [21], and high energy X-ray diffraction [64, 121, 15, 122, 2]. The latter two methods have been employed in more recent years, especially high energy X-ray diffraction. The former two experimental techniques have largely been used to determine the character of twins. Figure 2.9 details two historic micrographs (reproduced from [96] and [6]) showing twins forming in metals comprised of crystals exhibiting hexagonal symmetry. The twins in Figure 2.9(b) are bounded by parallel planes, and thus are of the lamellar type. Some twins also may form where the twins terminate at a singular point at their ends, referred to as lenticular twins. Figure 2.9(a) details both lamellar and lenticular twins - note how the larger twins stay planar throughout their lengths, even when terminating at a grain boundary, whereas some of the smaller twins experience a reduction in thickness as they approach their terminal points.

Electron backscatter diffraction additionally affords the ability to measure orientations of crystals, thus providing validation of twin orientation relationships [14]. Utilizing a combination of electron backscatter diffraction and high resolution digital image correlation allows for the study of straining on surfaces, and the investigation of surface strain states near twin tips. It has been observed that areas of high stress concentrations form in the vicinity of the tip of a deformation twin, extending into neighboring grains [4]. High resolution electron microscopy [135] affords information concerning the reorientation of the crystal lattice at a much smaller scale. Figure 2.10 (reproduced from

[135]) details an example crystal lattice reorientation across a twin boundary. Note the mirroring of the crystal lattice across the twin boundary.

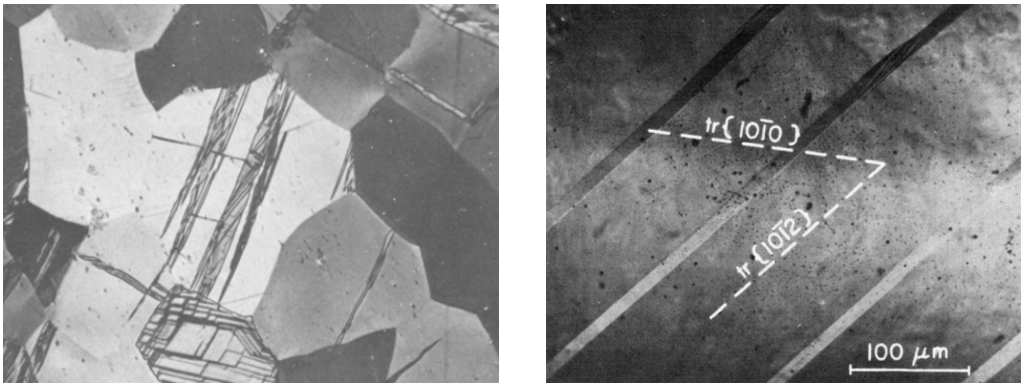

(a) (b)

Figure 2.9: Historic optical micrographs of (a) $\{1\,1\,\bar{2}\,2\}$ twins in polycrystalline zirconium, reproduced from [96], and (b) $\{1\,0\,\bar{1}\,2\}$ twins in single crystal titanium, reproduced from [6].

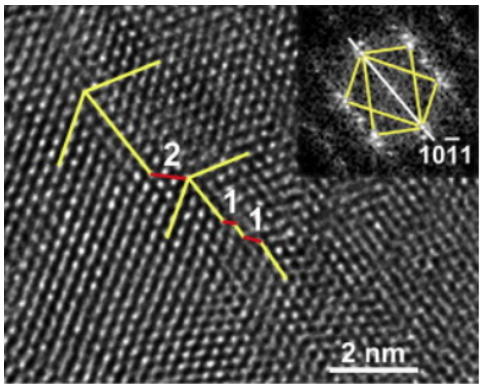

Figure 2.10: High resolution electron microscopy image of a crystal lattice with twin boundaries marked for a magnesium-titanium alloy with hexagonal crystal symmetry (reproduced from [135]).

Some observations have suggested that the development of plasticity by means of crystallographic slip may be arrested within twins, or at least restrict slip to planes nearly parallel to the twin planes [58, 102, 99]. This is proposed as an effect of the hardening of the twin region [102] by means of a combination of both a Hall-Petch effect, and the so called Basinski mechanism [13, 59] which describes an increase in slip strength

within a twin. Portions of the parent grain neighboring the twin must accommodate the deformation, and as such twins may continue to grow, or the surrounding body deforms by means of crystallographic slip. In some cases, voids or cracks may form if the body is otherwise unable to accommodate the formation of the twin [97, 122].

Roters outlines three main factors proposed to be linked to the formation of deformation twins - temperature and strain rate, grain size, and stacking fault energy [99]. These mechanisms are also outlined by Christian [26]. Reported findings on temperature dependence seem to be conflicting, with trends pointing both to a positive correlation between temperature and the formation of twins [76], and a negative correlation [16]. Similarly, literature is inconclusive on the role that strain rate plays in the formation of twins. Materials with relatively low stacking fault energies are often observed to be prone to deform by twinning, and it has been proposed that stacking fault energy decreases as temperature decreases. Indeed, few models have been proposed, and the most popular (described later in Chapter 2.3) considers twins to activate in the same way as slip systems - that is, when the resolved shear stress reaches a threshold - often with no regard to the above mentioned factors. Christian discusses this pseudo-slip proposal, detailing various studies with conflicting results [26].

Many of the methods described above are performed on surfaces of specimens, and performed *ex situ* - that is, after deformation has occurred. Ideally, *in situ* tests would be performed to gather data on the formation of deformation twins in real time. Specifically, high energy X-ray diffraction and high energy diffraction microscopy hold the greatest promise in developing experimental data sets to study deformation twinning. High energy X-ray diffraction allows for the deduction of grain average stress states for polycrystalline aggregates [41, 85, 131]. Twins may be observed to appear as new diffraction peaks in high energy X-ray diffraction experiments [120]. Developments

and improvement of the high energy diffraction microscopy method [73, 2, 127] could allow for the precise spatial locations of twins to be deduced. In conjunction, these methods have the ability to provide information concerning local grain-averaged stress states prior to twinning, and the knowledge of when and where deformation twins form [123]. This data, though not necessarily deterministic in terms of twin initiation, could be coupled with simulations to better understand possible nucleation mechanisms.

In summary, observations of deformation twins provide insight into their character in terms of their shape, as well as quantitative measures such as the shear due to twinning and the reorientation of the lattice. However, observations have yet to provide conclusive evidence as to the mechanism of twin nucleation or propagation. Whatever mechanism drives the formation of twins, a robust test-bed must be developed to simulate responses of discrete twins to gain better insight into their local effects so as to better understand why they occur.

2.2 Crystal Plasticity Finite Element Method

In this section, the crystal plasticity finite element framework considering only crystallographic slip is discussed. The framework herein uses a rate dependent restricted slip model [8] and Voce type hardening law [65] to predict the deformation of single crystals due to slip. Initially developed employing a Taylor hypothesis, and intended to predict texture evolution, these models were later implemented to predict the deformation of polycrystals in full field simulations [78, 77], assuming isotropic elasticity. Further developments extended the framework to include anisotropic elastic behavior and the ability to model intragrain deformation responses by finely discretizing single crystals (foregoing the Taylor hypothesis), and it was eventually employed on realis-

tic representations of microstructures [81, 11, 129, 41, 93, 132]. Here, the kinematics of deformation are discussed, followed by the constitutive models employed, the state evolution equations, and a brief description of the solution method (finite element implementation). This framework serves as the basis for the current study, and extension to include deformation by means of twinning is described in later a later chapter (Chapter 3).

2.2.1 Kinematics

Deformation and motion of material is achieved through an elastic stretch, a rotation, and plastic deformation. The total deformation gradient for a material point is decomposed into these three components (elastic, $\mathbf{F}^e$, plastic, $\mathbf{F}^P$, and a rotation, $\mathbf{F}^R$ - shown schematically in Figure 2.11):

$$\mathbf{F} = \mathbf{F}^e\mathbf{F}^R\mathbf{F}^P \tag{2.4}$$

The elastic portion of deformation is assumed to be composed of small elastic strains, $\mathbf{E}^e$, and is approximated by:

$$\begin{aligned} \mathbf{F}^e &= \mathbf{I} + \mathbf{E}^e \\ \text{where } &\|\mathbf{E}^e\| << 1 \end{aligned} \tag{2.5}$$

To better accommodate rate dependence of plastic flow in the numerical implementation, kinematics may also be considered in a rate form. To this end, the velocity gradient, $\mathbf{L}$, is deduced from the deformation gradient:

$$\mathbf{L} = \dot{\mathbf{F}}\mathbf{F}^{-1} \tag{2.6}$$

where "˙" denotes the time rate of change of a given variable - in this case the rate of change of the deformation gradient. The velocity gradient is decomposed into the

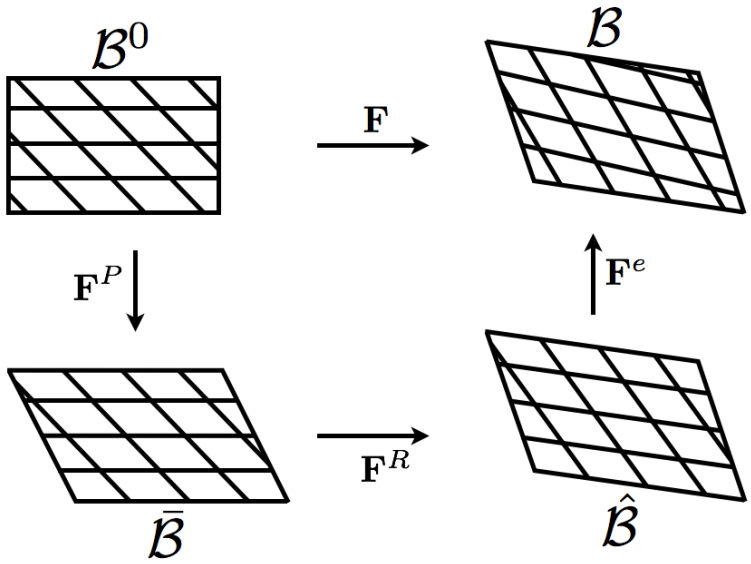

Figure 2.11: Illustration depicting kinematic decomposition of the deformation and motion of material.

deformation rate, **D**, and spin, **W**:

$$\mathbf{L} = \mathbf{D} + \mathbf{W} \tag{2.7}$$

Substituting Equation 2.4 into Equation 2.6, and separating the deformation rate into its hydrostatic and deviatoric components yields expanded forms of the deviatoric deformation rate and the spin (note that the small elastic strain assumption in Equation 2.5 has been employed):

$$\begin{aligned} \mathbf{D}' &= \dot{\mathbf{E}}^{e'} + \hat{\mathbf{D}}^{P'} + \mathbf{E}^{e'}\hat{\mathbf{W}}^{P} - \hat{\mathbf{W}}^{P}\mathbf{E}^{e'} \\ \text{and } \mathbf{W} &= \hat{\mathbf{W}}^{P} + \mathbf{E}^{e'}\hat{\mathbf{D}}^{P'} - \hat{\mathbf{D}}^{P'}\mathbf{E}^{e'} \end{aligned} \tag{2.8}$$

where "′" denotes the deviatoric component of a given variable. The plastic portions of the deviatoric deformation rate and the spin are transformed to the plastic intermediate configuration (denoted by "ˆ") - illustrated in Figure 2.11 - by means of the rotation portion of the deformation gradient:

$$\begin{aligned} \hat{\mathbf{D}}^{P'} &= \mathbf{F}^{R}\mathbf{D}^{P'}\mathbf{F}^{R^T} \\ \text{and } \hat{\mathbf{W}}^{P} &= \mathbf{F}^{R}\mathbf{W}^{P}\mathbf{F}^{R^T} \end{aligned} \tag{2.9}$$

2.2.2 Constitutive Equations

The elastic portion of deformation is governed by Hooke's law,

$$\boldsymbol{\tau} = \mathbf{C}(\mathbf{r})\mathbf{E}^e \tag{2.10}$$

where the Kirchhoff stress, $\boldsymbol{\tau}$, is related to the elastic strain through the use of a fourth order anisotropic stiffness tensor, $\mathbf{C}$, which is reduced to reflect the symmetry of the crystal [84]. Additionally, orientation dependence of the stiffness tensor is included by means of the Rodrigues parameterization, $\mathbf{r}$, of a crystal's orientation.

Plasticity is governed by a rate-dependent restricted slip model. The plastic portion of the velocity gradient is decomposed into the plastic deformation rate and the plastic spin in a similar fashion to Equation 2.7. The plastic deformation rate, $\hat{\mathbf{D}}^{P'}$, is a linear combination of simple shearing modes:

$$\begin{aligned} \hat{\mathbf{D}}^{P'} &= \sum_k \dot{\gamma}^k \hat{\mathbf{P}}^k \\ \text{where } \hat{\mathbf{P}}^k &= \text{sym}\left(\hat{\mathbf{s}}^k \otimes \hat{\mathbf{m}}^k\right) \end{aligned} \tag{2.11}$$

where $\dot{\gamma}^k$ denotes the shearing rate on a slip system, k, and $\hat{\mathbf{P}}^k$ is the symmetric portion of a slip system's Schmid tensor - constructed using a slip system's slip direction, $\hat{\mathbf{s}}^k$, and plane normal, $\hat{\mathbf{m}}^k$. Slip systems commonly considered for hexagonal close packed crystals are shown in Figure 2.2. The plastic spin is defined as:

$$\begin{aligned} \hat{\mathbf{W}}^P &= \dot{\mathbf{F}}^R \mathbf{F}^{R^T} + \sum_k \dot{\gamma}^k \hat{\mathbf{Q}}^k \\ \text{where } \hat{\mathbf{Q}}^k &= \text{skw}\left(\hat{\mathbf{s}}^k \otimes \hat{\mathbf{m}}^k\right) \end{aligned} \tag{2.12}$$

where $\hat{\mathbf{Q}}^k$ is the skew portion of the Schmid tensor.

The shearing rate of a given slip system is defined using a power law expression to introduce rate dependence (controlled by m), and relates the shearing rate on a slip

system to the resolved shear stress of a system, τ^k:

$$\begin{aligned} \dot{\gamma}^k &= \dot{\gamma}_0 \left(\frac{|\tau^k|}{g^k} \right)^{\frac{1}{m}} \operatorname{sgn}(\tau^k) \\ \text{where } \tau^k &= \operatorname{tr}(\hat{\mathbf{P}}^k \boldsymbol{\tau}') \end{aligned} \tag{2.13}$$

Here, the shearing rate on a slip system is scaled by the fixed-state strain rate scaling coefficient, $\dot{\gamma}_0$, and is dependent on a slip system's current strength, g^k.

2.2.3 State Evolution

The state of a given point in a material is described using the current crystallographic orientation and the current slip system strengths. The evolution equations of these variables are cast in a rate form. First, the evolution of the orientation of a crystal is again written in terms of its Rodrigues parameterization:

$$\dot{\mathbf{r}} = \frac{1}{2} \left(\boldsymbol{\omega} + (\boldsymbol{\omega} \cdot \mathbf{r}) \, \mathbf{r} + \boldsymbol{\omega} \times \mathbf{r} \right) \tag{2.14}$$

where $\boldsymbol{\omega}$ is defined using the plastic portion of spin:

$$\boldsymbol{\omega} = \operatorname{vect} \left(\hat{\mathbf{W}}^P - \sum_k \dot{\gamma}^k \hat{\mathbf{Q}}^k \right) \tag{2.15}$$

Second, evolution of each slip system strength is defined using a Voce hardening assumption:

$$\begin{aligned} \dot{g}^k &= h_0 \left(\frac{g_s^k(\dot{\gamma}) - g^k}{g_s^k(\dot{\gamma}) - g_0^k} \right)^n \dot{\gamma} \\ \text{where } g_s^k(\dot{\gamma}) &= g_{s0}^k \left(\frac{\dot{\gamma}}{\dot{\gamma}_{s0}} \right)^{m'} \text{ and } \dot{\gamma} = \sum_k |\dot{\gamma}^k| \end{aligned} \tag{2.16}$$

Isotropic hardening is assumed, such that the evolution of hardening of one slip system causes all other slip systems to harden at the same rate. In other words, the single crystal yield surface is assume to expand equally in all directions. The instantaneous

rate of evolution is controlled by the strength hardening rate coefficient, h_0, the current slip system strength, g^k, the initial strength, g_0^k, the saturation strength, g_s^k, and the non-linear Voce exponent, n. Furthermore, the saturation strength depends on deformation rate according to a power-law relation with the net rate of slip, $\dot{\gamma}$.

2.2.4 Implementation

The above models are implemented in a parallelized finite element framework. Here, the basics of the algorithm are discussed to achieve a sense of how the method approximates solutions to the problems above. A complete description of the implementation can be found in Appendix A.

Broadly speaking, the domain of the polycrystal - including the interior features (i.e., grain boundaries) - is discretized into a finite element mesh, comprised of elements and nodes. Each element of the mesh is assigned a crystallographic orientation, crystallographic phase, and hardness values based on the grain in which it resides. Boundary conditions are assigned to nodes on surfaces of the polycrystal's domain domain. As the implementation is cast in a rate form, essential velocity boundary conditions are applied at nodes (traction boundary conditions are not implemented in the current framework). The existing framework also assumes that nodes assigned essential velocity boundary conditions retain those assignments throughout the course of deformation (though they may be scaled in magnitude or reversed in direction).

A solution scheme is outlined below, and a flowchart of the main solution steps of a simulation step are shown in Figure 2.12. Here, the velocity field, V, nodal coordinates, X, crystal rotation $\mathbf{F}^R$, and crystal hardness, g, are all considered in a global form. For a given simulation step, n, and a change in time over said step, Δt:

1. Make guess for velocity field, $V_n = V_g$
    - If $n = 1$, use solution of V from isotropic viscoplastic solution
    - If $n > 1$, use converged solution of from previous step, V_{n-1}
2. Estimate new nodal coordinates, $X_g = X_{n-1} + \Delta t V_g$
3. Compute velocity gradient at each element
4. Iterate to calculate crystal rotations, $\mathbf{F}_i^R$, and hardnesses, g_i
    - For each element, iterate on stress state:
    - If $n = 1$, use stress guess from isotropic viscoplastic solution
    - If $n > 1$, use converged stress from previous step
    - Recompute $\mathbf{F}_i^R$, g_i
    - Check convergence based on norms of $\mathbf{F}_i^R$, g_i
5. Compute new velocity field, V_i
6. Check residual
    - If converged, continue with current V_i
    - If not, return to step 2 with $V_g = V_i$
7. Update the velocity field, nodal points, and state for the end of the time step, n
    - $V_n = V_i$
    - $X_n = X_{n-1} + \Delta t V_i$
    - $\mathbf{F}_n^R = \mathbf{F}_i^R$, $g_n = g_i$

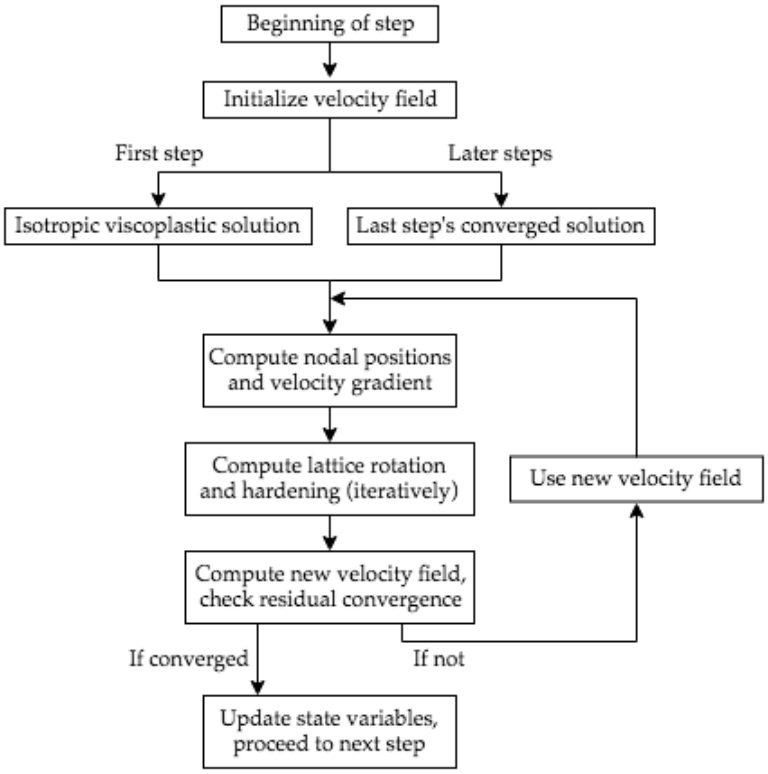

Figure 2.12: Flowchart depicting the overarching steps of a time step in a simulation.

2.3 Existing Twinning Modeling Efforts

The model described in Chapter 2.2, again, considers only crystallographic slip as a means to model plastic deformation. Attempts have been made, however, to include twinning as a mode of plastic deformation in similar frameworks. These existing models are limited in scope due to simplifications necessary in light of historic computational limitations. This section will briefly summarize the dominant existing model for considering deformation twinning in a crystal plasticity framework.

In an effort to approximate the bulk deformation response of a material that deforms by means of both slip and twinning, a model that considers the deformation of a material

point by a simultaneous combination of both deformation modes has been developed that considers twinning in a similar fashion as slip. Building on previous work [52, 119], Kalidindi is credited with popularizing the pseudo-slip model [58]. This class of model or variations thereof are perhaps among the most widely used to represent twinning in materials in crystal plasticity simulations [113, 47, 103, 134, 109, 27, 83, 67, 25, 72, 1, 54, 29, 3, 7, 74]. It is an attractive choice, due in large part to its ease in implementation and marginal computational cost (when compared to modeling plasticity by means of slip only). This class of model appears in various forms, and has been extended since its inception - including extension to model transformation induced plasticity [130]. For sake of brevity, a summary of Kalidindi's original formulation is discussed here.

Generally speaking, the model considers twinning as a modified additional family of slip systems with an associated critical resolved shear stress - hence the term "pseudo-slip". A fraction of each material point is assumed to deform solely by slip, while the remainder fraction of the material point is assumed to have twinned. The deformation response of a material point is then homogenized by considering these fractions as the weights for the contribution of each deformation mode to the total deformation response. The magnitude of the volume fraction that is considered to have twinned is evolved over the course of deformation. The model does not consider spatially discrete deformation twins, and the relative rate disparity between twinning and slip is obscured due to homogenization of the deformation responses. This, in turn, prohibits the detailed study of local deformation responses due to the onset of twinning, and instead only affords an averaged view of deformation due to both slip and twinning.

The base framework in which this type of model is implemented is similar to that described in Chapter 2.2, and thus only large deviations from the methodology described above are highlighted.

The deformation gradient is again decomposed into an elastic stretch, a rotation, and a contribution due to plasticity (identical to Equation 2.4). Different in this framework is that the material point is considered split into two regions or "volume fractions" - those which have twinned and those which have not - that contribute to the plastic portion of deformation (shown schematically in Figure 2.13). The illustration shows a twin boundary represented by a dashed line. Casting kinematics again in a rate form, the

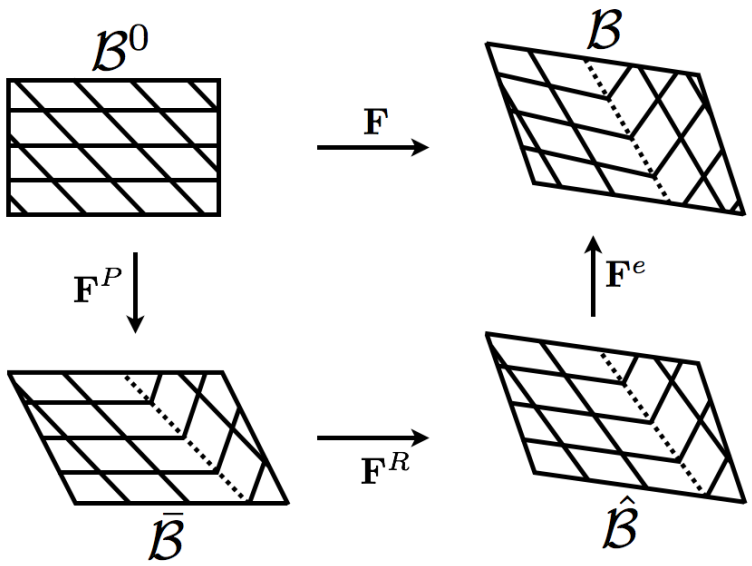

Figure 2.13: Illustration depicting kinematic decomposition of the deformation and motion of material including twinning at a material point (twin "boundary" denoted by dashed line).

plastic velocity gradient is a combination of both deformation modes, slip and twinning:

$$\mathbf{L}^P = \left(1 - \sum_{\beta}^{n^{tw}} f^{\beta}\right) \sum_{k}^{n^{s}} \dot{\gamma}^k \mathbf{S}^k + \sum_{\beta}^{n^{tw}} \dot{f}^{\beta} \gamma^{tw} \mathbf{S}^{\beta} + \sum_{\beta}^{n^{tw}} f^{\beta} \left(\sum_{k}^{n^{s}} \dot{\gamma}^k \mathbf{S}^k \right) \tag{2.17}$$

where n^s and n^{tw} are the number of slip systems (each represented by k) and the number of twin systems (each represented by β), respectively. Additionally, f^{β} refers to the fraction of the crystal that has twinned for a given twin system, γ^{tw} refers to the shear associated with twinning, and $\mathbf{S}$ is the Schmid tensor for the slip or twin systems. Consequently, the first term represents the portion due to slip in regions that have not

twinned, the second term represents the portion due to twinning, and the final term represents the portion due to slip in regions that have twinned. It is here that we see that the volume fraction described above is not a true material volume - as discrete twins are not modeled - but rather a value used to homogenize the deformation response at a given material point.

The Cauchy stress, $\mathbf{T}$, for either the un-twinned material ("pt") or twinned material ("tw") are defined as:

$$\begin{aligned} \mathbf{T}^{pt} &= \mathbf{C}(\mathbf{r}^{pt})\mathbf{E}^{e} \\ \mathbf{T}^{tw} &= \mathbf{C}(\mathbf{r}^{tw})\mathbf{E}^{e} \end{aligned} \tag{2.18}$$

where $\mathbf{E}^{e}$ is the elastic strain at the material point, and the reorientation of the twinned portion of the material point is accounted for in the rotation of the stiffness tensor. The stress is then averaged over the material point, considering the fraction of the material point that is considered to have twinned:

$$\mathbf{T} = \left(1 - \sum_{\beta} f^{\beta}\right)\mathbf{T}^{pt} + \sum_{\beta} f^{\beta}\mathbf{T}^{tw\beta} \tag{2.19}$$

where f^{β} is the volume fraction of the grain that has twinned, and $\mathbf{T}^{tw\beta}$ is the Cauchy stress for the β^{th} twin system.

For Equation 2.17, the shear rate of the slip systems may be calculated with any relevant relationship - a power law relationship (Equation 2.13) is the most common choice. Hardening may be evolved as well. The rate of change volume fraction of the crystal that has twinned is calculated using a rate dependent power law (in a similar fashion to how slip rates are calculated):

$$\dot{f}^{\beta} = \begin{cases} \dfrac{\dot{\gamma}}{\gamma^{tw}}\left(\dfrac{\tau^{\beta}}{g^{\beta}}\right)^{\frac{1}{m}} & \tau^{\beta} > 0 \text{ and } \displaystyle\sum_{\beta}^{n^{tw}} \leq f^{max} \\ 0 & \tau^{\beta} \leq 0 \text{ and } \displaystyle\sum_{\beta}^{n^{tw}} > f^{max} \end{cases} \tag{2.20}$$

where variables are similar to those described in Equation 2.13. Note that the dependence on the resolved shear stress is unidirectional. In other words, the volume fraction only evolves (read: the crystal twins) only if the parent grain is sheared in one direction, or twinning only occurs in one direction related to a twin system (as opposed to slip, which can happen in either direction for a given slip system). Additionally, the model is dependent on some maximum volume fraction of a crystal that can have twinned, f^{max}. At some point, the model assumes twinning is arrested within a grain.

Historically, a simulated polycrystal would be discretized such that one material point would represent a number of discrete grains, with the solution homogenized considering the responses from various crystals at each material point. Considering this, this model was relatively sophisticated when implemented into such frameworks. However, computational capabilities have increased such that each grain may now be discretized into many material points rather than vice versa, and consequently such homogenization may not be entirely appropriate. In other words, full field simulations with finely discretized grains aim to capture intragrain deformation heterogeneity, while homogenization techniques were developed to capture only bulk response. While this pseudo-slip approach to twinning may succeed in predicting the bulk response and some local effects due to twinning (volume fraction, and perhaps even average stress), the model fails to provide refined results. Additionally, by considering twinning as an auxiliary slip system, the physical differences between deformation twinning and crystallographic slip are relaxed. Namely, the discrete nature of twinning is not considered, and the disparate shear rates between slip and twinning are obscured.

Variations on this model have also been extended to a method intended to model texture evolution in Rodrigues' orientation space. Initially developed considering only crystallographic slip [68, 69, 70], the method aims to capture trends in terms of tex-

ture evolution by foregoing full-field modeling, and instead focuses on the reorientation trajectories of crystals in orientation space. The model proves accurate in determining the reorientation of crystals to preferential orientations when subjected to various macroscopic loadings. The model was extended [82] to include twinning in a fashion similar to above, by considering twin systems as pseudo-slip systems, and to track volume fractions in orientation space. The model predicts "sources" and "sinks" - that is, orientations of a grain that twins (source) to a new orientation (sink). Sources are orientations which exhibit increasing twin volume fractions. Results may be used to predict macroscopic stress states [66]. This model, however, only predicts texture evolution, and purposefully ignores local effects due to twinning by instead focusing directly on bulk trends.

CHAPTER 3

A FRAMEWORK FOR DISCRETE DEFORMATION TWINNING

This chapter is devoted to outlining the necessary steps to include the ability to model discrete deformation twins in the existing framework described in Chapter 2.2. As the implementation relies heavily on the existing framework, only the points that differ will be outlined here.

The existing framework is shown to be a robust tool in predicting deformation due to crystallographic slip in the studies presented in Appendices B and C. The study presented in Appendix B demonstrates good correlation between the model and experimental results in terms of the initiation of slip activity within a polycrystalline aggregate. The study further indicates that the spatial arrangement of grains has large effects on the development of plasticity, and must be included to accurately model the plastic response at this scale. The study presented in Appendix C introduces a novel multilevel tessellation method to represent sub-grain morphological features, including the discretization of grains into lamellar regions used to represent a second crystallographic phase. Results of simulations performed on these multilevel tessellations further indicate that the spatial arrangement of both grains and crystallographic phases play important roles in the development of plasticity. The results of both studies provide confidence in the existing framework, allowing for the extension to include discrete deformation twins, as well as further indication that discrete twins - which will alter the spatial arrangement of grains in an aggregate - are necessary for modeling deformation twinning.

The aim of the extended framework is to construct the ability to insert discrete deformation twins via into a polycrystalline aggregate at relatively high shear rates. This is achieved by considering discrete lamellar regions which may twin by pre-discretizing a polycrystalline aggregate via a multilevel tessellation approach described in Appendix

C - used here to represent regions which may be considered for twinning, rather than pre-existing microstructural features. During a twin event, the defined shear due to twinning is applied to a discrete region, and the crystal lattice is reoriented within the region - all over a time step short enough to provide shear rates several orders of magnitude faster than those associated with crystallographic slip. The framework distinguishes itself from the primary existing method for augmenting slip with deformation twinning described in Chapter 2.3, which ignores the deformation of discrete regions and the large disparity between shear rates associated with slip and twinning. Here, both deformation twinning and crystallographic slip are considered distinct, rather than a single modified deformation mode. This uniquely allows for the study of complex local deformation responses due to the onset of twinning in ways that existing frameworks do not afford, as the motion of a discrete region due to twinning is prescribed, and the reaction of the surrounding aggregate is modeled.

This chapter is divided into a section describing the pre-discretization of a polycrystalline aggregate into regions which may twin, and a section describing the framework for inserting twins at arbitrary points in deformation.

3.1 Discretization of Twin Regions

The cornerstone of the extended framework presented in this study is the ability to discretize single grains into regions which may be considered as twin regions at some point in deformation. Upon discretization of a domain into grains and possible twin regions, an attendant finite element mesh is constructed, and the framework controls the elements and nodes of an appropriately shaped twin region. The deformation due to twinning may be applied, thus, to discrete regions (described in Chapter 3.2), maintaining a key dif-

ference between crystallographic slip and twinning. In short, a multilevel tessellation method (Appendix C.3.1) is employed to discretize a domain into a number of grains and to further discretize grains into regions which may be considered for deformation twinning. A finite element mesh is constructed for the resulting geometry.

Cottrell described the phenomenon of a region undergoing deformation twinning as "...lamella in a stressed crystal deforms into a new orientation which is related symmetrically about some simple crystal plane or axis to the orientation of the undeformed parts of the crystal" [28]. Indeed, various experimental studies of deformation twins (Chapter 2.1.3) have witnessed twins forming in regions bounded roughly by parallel planes, or lamellar regions. While twins of different shapes are known to form (e.g., lenticular twin regions), this present study focuses entirely on deformation twins of the lamellar type.

Focusing on lamellar twins allows for the use of existing frameworks to instantiate samples with twin regions. The multilevel tessellation method described in Appendix C.3 established the ability to discretize domains into lamellae by means of the insertion of successive parallel planes into arbitrary domains. Finite element meshes are generated for these complex regions. Figure C.5 details a multilevel tessellation in which lamella are instantiated to represent a material's second phase morphology. Steps 3 and 4 (Figures C.5(c) and C.5(d), respectively) are of particular importance, as they illustrate the discretization of domains (colonies in the referenced figures) using parallel planes, and the concatenation of all subsequent domains into a polycrystal.

Similarly, grains may be discretized prior to simulation to include lamella intended here to represent twin regions. Figure 3.1 details a flowchart of how a multilevel tessellation is employed to instantiate twin regions. A first level of tessellation is generated (Laguerre or Voronoi) to represent grains in a polycrystal (Figure 3.1(a)). At this point,

successive levels of tessellations may be generated to represent finer details of the microstructure (e.g., sub-grains, colonies, etc.). For this study, sub-grain structures are not considered, and consequently only grains are considered.

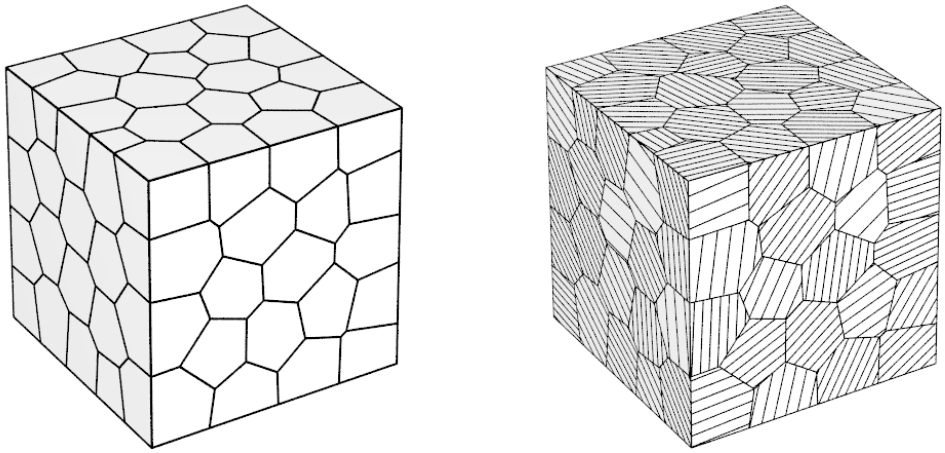

(a) (b)

Figure 3.1: A domain discretized into (a) grains, and (b) further discretization into candidate twin regions.

The final level of tessellation is to generate lamellar regions within grains (or sub-grains, colonies, et. cetera) to represent twin regions (Figure 3.1(b)). Twin regions are generated using planar slices, which are defined by plane normals. This requires a knowledge of the region's crystallographic orientation - as well as the twin system being represented - to calculate the twin plane normal in the sample reference frame. Here, knowledge of the reciprocal lattice vector will be employed to calculate the twin plane normal given the Miller-Bravais values for a given twin plane.

First, the crystal basis is defined (Figure 3.2) in a reference basis (an orthonormal

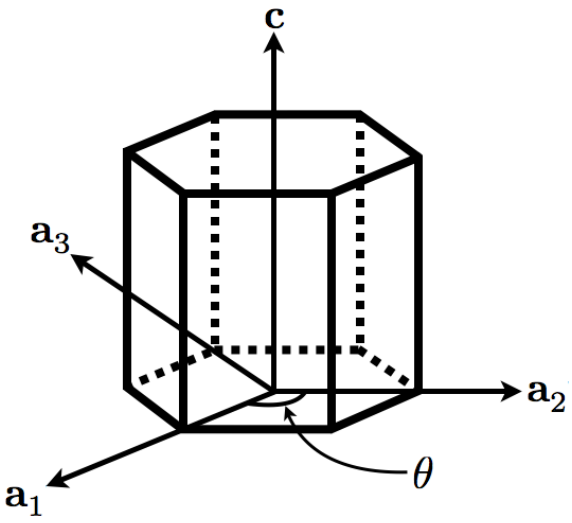

Figure 3.2: Illustration of basis vectors for an hexagonal crystal.

basis, **e**):

$$\begin{aligned} \mathbf{a}_1 &= \mathbf{e}_1 \\ \mathbf{a}_2 &= \cos(\theta)\,\mathbf{e}_1 + \sin(\theta)\,\mathbf{e}_2 \\ \mathbf{c} &= \frac{c}{a}\mathbf{e}_3 \end{aligned} \tag{3.1}$$

where $\theta = 120°$, and $\frac{c}{a}$ is the aspect ratio of the crystal [51]. Note, $\mathbf{a}_3$ is a redundant axis as it is not linearly independent, and is thus ignored.

The reciprocal basis is constructed from the crystal basis:

$$\begin{aligned} \mathbf{b}_1 &= \frac{2\pi}{V_b}(\mathbf{a}_2 \times \mathbf{c}) \\ \mathbf{b}_2 &= \frac{2\pi}{V_b}(\mathbf{c} \times \mathbf{a}_1) \\ \mathbf{b}_3 &= \frac{2\pi}{V_b}(\mathbf{a}_1 \times \mathbf{a}_2) \end{aligned} \tag{3.2}$$

$$\text{where } V_b = \mathbf{a}_1 \cdot (\mathbf{a}_2 \times \mathbf{c})$$

and the reciprocal lattice vector is constructed from the reciprocal basis and the Miller-Bravais indices for a plane, $\{h\,k\,i\,l\}$:

$$\mathbf{g}_{hkl} = h\mathbf{b}_1 + k\mathbf{b}_2 + l\mathbf{b}_3 \tag{3.3}$$

A plane normal in real space is defined as the normalized reciprocal lattice vector for that crystallographic plane:

$$\mathbf{n}_{hkl}^{C} = \frac{\mathbf{g}_{hkl}}{||\mathbf{g}_{hkl}||} \tag{3.4}$$

Finally, with knowledge of the crystallographic orientation, and thus the ability to construct a rotation matrix from the crystal to the sample frame, $\mathbf{R}^{C,S}$, the plane normal for a given crystallographic plane and crystallographic orientation is deduced:

$$\mathbf{n}_{hkl}^{S} = \mathbf{R}^{C,S}\mathbf{n}_{hkl}^{C} \tag{3.5}$$

This may be calculated for the twin plane normals of any number of twin systems for a given grain. Procedurally, to instantiate a polycrystal with a pre-determined number of grains, an orientation set is first generated, with a number of discrete crystallographic orientations equal to the number of grains. The twin plane normals are then calculated for each discrete orientation. These normals are used to instantiate the polycrystal. A tessellation is created, in which each grain, having been assigned a discrete orientation from the orientation set, is discretized into twin regions using the appropriate twin plane normals. Polycrystals are generated using the Neper software package [92].

Theoretically, a domain can be divided using any number of sets of planes with associated normals. Practically, however, this presents challenges. Figure 3.3 illustrates the primary challenge on three circular, planar crystals. The first crystal (Figure 3.3(a)) is shown subdivided into lamellar regions, while the second and third crystals (Figures 3.3(b) and 3.3(c)) are subdivided into two or three separate sets of lamellar regions, respectively, all defined by normals, $\mathbf{n}$. The highlighted region (red circle in Figure 3.3(b)) of the second crystal shows the intersection of two lines. Including more planes increases the number of intersections, and the probability of low-angle intersections, as shown in the highlighted region of Figure 3.3(c). These regions will necessitate meshes with selective refinement in regions of low-angle intersections, as well as undesirable

elements with poor aspect ratios (which often leads to premature simulation failure). This concept is even further complicated when extended to three dimensions, as more complex intersections may form.

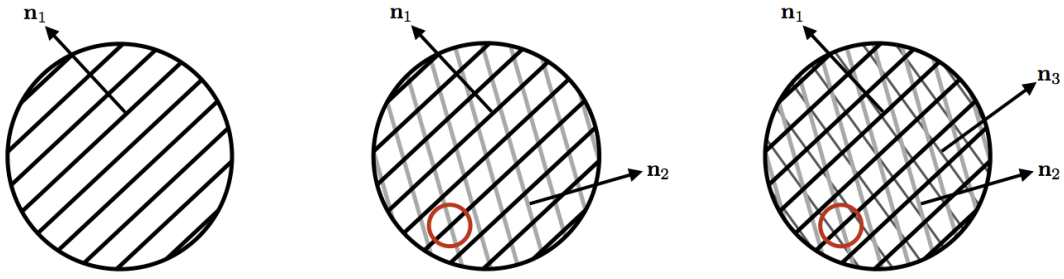

(a) (b) (c)

Figure 3.3: Illustration depicting planar crystals subdivided using (a) a single set of parallel lines, (b) two sets of parallel lines, and (c) three sets of parallel lines.

Experience gained in the study outlined in Appendix C provided insight on the instantiation of microstructures with embedded lamella. The intersection of lamellar planes invariably led to poorly formed elements and mesh refinement near intersection points. Simulations with finely discretized lamella in every colony failed at relatively low strains, as the mesh could not accommodate large deformations. Low quality elements tended to deform in ways that would lead to the calculation of negative determinants of the Jacobian at quadrature points, causing the simulation to fail. The solution employed in that study was to discretize colonies with a selective lamellar width ("thin-wide" stacking of neighboring lamella) to minimize the number of intersections, which can be seen in Figure C.5(d).

Consequently, in this study, grains are divided using only a single set of twin regions (similar to Figure 3.3(a)). This facilitates the creation of a mesh comprised of high-quality elements, removing the challenges associated with poor meshes. The twin

system chosen for this present study is the $\{1\,0\,\bar{1}\,2\}$ twin system. Twin plane normals are calculated with this in mind. Were a grain to necessitate the instantiation of multiple systems, selective lamellar width could be employed, but would limit twins to a single spatial location - illustrated in Figure 3.4. This would, additionally, only help for perhaps two twin systems, and instantiation of three or more systems would still be difficult. This method, however, is advantageous if the twin system and twin location are known *a priori* by means of some experimental data - mesh size will be reduced, decreasing simulation completion time, and the number of intersections will be reduced, increasing the quality of the mesh.

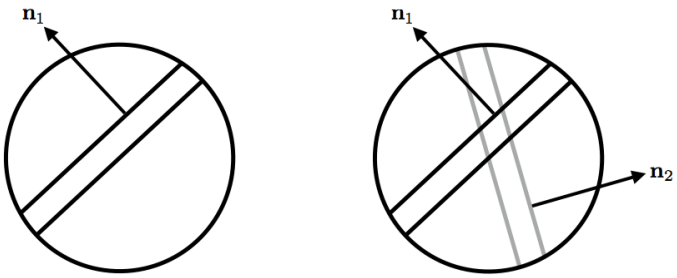

Figure 3.4: Illustration depicting planar crystals subdivided using (a) a single twin system with selective lamellar width, and (b) two twin systems with selective lamellar width.

In summary, a multilevel tessellation method is employed to discretize a domain into grains, and subsequently discretize grains into regions which may be considered for deformation twinning. Discretization of twin regions is achieved by calculating the twin plane's normal in the sample frame, with knowledge of the twin system and crystallographic orientation of the parent grain. Only a single twin system is considered in each grain so as to reduce the complexity of the geometry. This ensures the formation of a finite element mesh with reduced over-refinement, and a reduction of poorly formed elements. The pre-discretization of grains into lamellae which may be considered for

twinning during deformation simulation is unique, and is necessary to predict the local responses due to the onset of twinning. This improves upon existing models, which fail to consider the discrete nature of deformation twins, and instead simply homogenize deformation responses due to both slip and twinning at local material points even in finely resolved simulations.

3.2 Description of Framework

This section outlines the framework to insert deformation twins given a finite element mesh of a domain discretized into lamellar regions. The section is divided into two portions, one describing the imposition of the shear on a twin region by applying temporary velocity boundary conditions to the nodes within a lamellar region, and the other describing the reorientation of the crystal lattice within the twin region to the expected orientation. The body, otherwise, is permitted to deform by means of crystallographic slip, utilizing the existing crystal plasticity finite element framework to approximate the solution.

Treating deformation twinning as a boundary value problem with imposed essential boundary conditions enforcing the correct motion - and thus correct mapping of nodal points to their twinned location - allows the solver to model the response of the material surrounding the twin region. Motion is imposed, the twin reoriented, and the surrounding aggregate responds to the deformation. In this way, local states are predicted in a way that is not captured by existing frameworks. Existing methods apply a simple shear associated with twinning to local material points (more accurately, a homogenization of shear due to slip and shear due to twinning), rather than considering discrete regions, and as such, the surrounding material's reaction at this scale is not properly predicted.

Additionally, the imposition of motion due to twinning may be applied at a rate several orders of magnitude faster than typically exhibited by crystallographic slip. This, too, is an improvement of existing twin modeling schemes, which obscure the differences in shear rates between slip and twinning by homogenizing the response at local points.

3.2.1 Application of Boundary Conditions

The discretization of a sample into grains and lamellar twin regions, as described in the previous section, leads to the generation of an accompanying finite element mesh. The discretization of lamellar twin regions, consequently, allows for the consideration of a subset of elements and nodes associated with individual twin regions with an appropriate geometric morphology. To properly apply the motion due to twinning to a specific region, the nodal points within a region are considered. In short, this section describes how the nodal points are moved to their expected twin locations. This is achieved by temporarily applying essential boundary conditions to the nodes within a twin region such that the nodal points are properly mapped to their expected locations.

The crystal plasticity finite element framework, as currently constructed, accepts essential velocity (as the framework is cast in a rate form) boundary conditions. For an ordinary simulation - such as the uniaxial tension of a single crystal in the shape of a rectangular prism discretized into a finite element mesh (Figure 3.5(a)) - velocity boundary conditions are applied to two opposing surfaces. So called "grip" boundary conditions, for example, are intended to hold the area of the two opposing surfaces fixed, while one of these surfaces is held motionless and the other is the extension surface. Velocity boundary conditions are applied as components in the sample basis directions. For each node, that is, velocities are given as $\mathbf{v}_x$, $\mathbf{v}_y$, and $\mathbf{v}_z$, where x, y, and z are

the sample directions. As such, imposed velocities can be visualized as triads of their components.

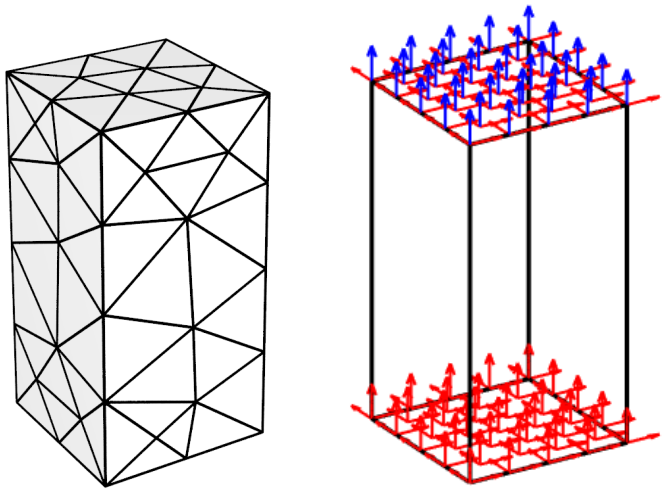

(a) (b)

Figure 3.5: (a) Mesh of a single crystal instantiation, and (b) applied velocity boundary conditions at surface nodes, where red arrows denote zero velocities and blue arrows denote non-zero velocities.

Figure 3.5(b) shows the the applied grip boundary conditions on the surface nodes. Note that the triads depicting the boundary conditions appear not only at the element vertices, but at the mid-node locations as well, as the framework utilizes quadratic elements. The nodes on the bottom surface are fixed in all directions, while the nodes on the top surface have velocities applied such that the top surface extends away from the bottom surface yet is fixed in the other directions, satisfying the intended purpose of this style of boundary condition as described above.

For ordinary simulations, nodes which are given applied boundary conditions retain them throughout the course of the simulation. To apply the motion of a region due to deformation twinning, however, this restriction is temporarily relaxed. Boundary conditions are adaptively placed on the nodes that reside within or on the boundary of a region to be twinned. Velocities are held constant for nodes in the twin region until

the nodes within the region reach their expected twinned locations. During this time, all other nodes with applied boundary conditions are temporarily held in a fixed position (that is, all velocities at these nodes are temporarily set to zero).

Figure 3.6(a) shows a single crystal discretized into lamellar regions, and its attendant finite element mesh is shown in Figure 3.6(b). Grip boundary conditions are initially applied to the mesh (similar to Figure 3.5(b)). At some point in deformation when a twin is inserted, the grip conditions are temporarily held at zero, while boundary conditions are applied to any twin region (Figure 3.6(c)). When the twin motion is complete, boundary conditions are returned to normal (again, similar to Figure 3.5(b)), and the simulation continues. Note that the twin boundary conditions are shown to all

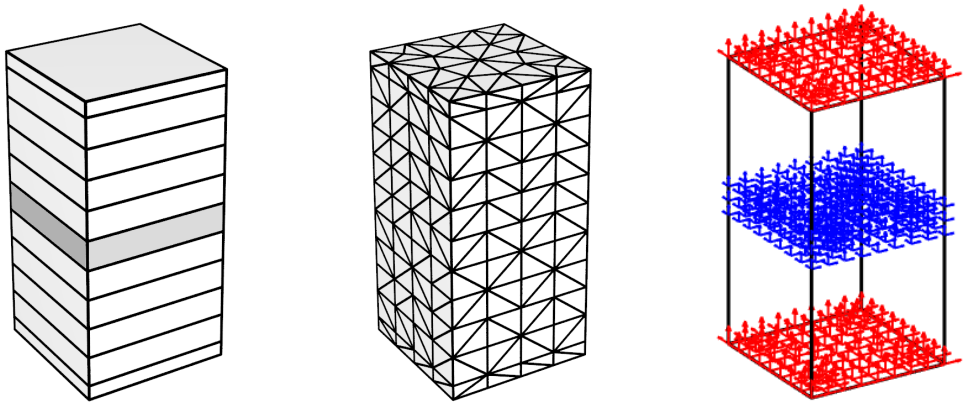

(a) (b) (c)

Figure 3.6: (a) Single crystal discretized into lamella, with example twin highlighted, (b) its mesh, and (c) boundary conditions during deformation twinning motion.

be non-zero. In general this is true, though there exists special cases. Consider, for instance, a twin with its normal and shear directions aligned with two of the coordinate axes. As the twin motion is only in the shear direction, the boundary conditions for the twin would have non-zero components only in that direction - the other two would be fixed.

The essential velocity boundary conditions imposed on the nodes within a twin region are calculated as follows: first the deformation gradient for a deformation twin is defined as [82]:

$$\mathbf{F}_{tw} = \mathbf{I} + S\left(\mathbf{d}^{tw} \otimes \mathbf{n}^{tw}\right) \tag{3.6}$$

where S is the shear magnitude, $\mathbf{d}^{tw}$ is the shear direction, and $\mathbf{n}^{tw}$ is the twin plane normal (associated with S, η_1, and K_1, respectively, in Table 2.2). The shear magnitude is constant for a given twin system, the twin normal is calculated in the same manner as in Chapter 3.1, and the shear direction is directly calculated from its Miller-Bravais indices with knowledge of the crystal basis and the orientation of the crystal.

Within a twin region, $\mathbf{d}^{tw}$ and $\mathbf{n}^{tw}$ are calculated for every element. As some misorientation will likely develop within a region prior to twinning, elements within a region will have different values for $\mathbf{d}^{tw}$ and $\mathbf{n}^{tw}$, and thus different values for the calculated $\mathbf{F}_{tw}$. To ensure compatibility of elements within a twin region, the same deformation gradient is applied to all elements within a region. This assumption is inconsequential if the development of misorientation within a region is small - valid at lower strains, certainly at strains below macroscopic yield. Volume weighted averages for the shear direction and twin plane normal are calculated so as to arrive at only a single value of $\mathbf{F}$ to be applied to all elements within the region:

$$\begin{aligned}
\mathbf{d}^{tw}_{avg} &= \left\langle \mathbf{d}^{tw} \right\rangle = \frac{1}{V}\sum_{i}^{n_{elem}} V_i^{el}\mathbf{n}_i^{tw} \\
\mathbf{n}^{tw}_{avg} &= \left\langle \mathbf{n}^{tw} \right\rangle = \frac{1}{V}\sum_{i}^{n_{elem}} V_i^{el}\mathbf{d}_i^{tw} \\
\text{and } \mathbf{F}_{tw} &= \mathbf{I} + S\left(\mathbf{d}^{tw}_{avg} \otimes \mathbf{n}^{tw}_{avg}\right)
\end{aligned} \tag{3.7}$$

where V is the total volume of the twin region, n_{elem} is the number of elements in a twin region, and V_i^{el}, $\mathbf{d}_i^{tw}$, and $\mathbf{n}_i^{tw}$ are the volume, calculated shear direction, and calculated twin plane normal for the i^{th} element within a twin region.

For all nodes within a twin region, the final location due to the twinning motion, $\mathbf{x}_{tw}$ is calculated:

$$\mathbf{x}_{tw} = \mathbf{F}_{tw}\mathbf{x} \tag{3.8}$$

where $\mathbf{x}$ is a vector of the Cartesian coordinates for a node within the twin region prior to twinning. Thus, the nodal displacement is:

$$\mathbf{u}_{tw} = \mathbf{x}_{tw} - \mathbf{x} \tag{3.9}$$

To facilitate convergence in the solver, the total displacement is achieved incrementally over a number of steps, n_{steps}:

$$\mathbf{u}_{incr} = \frac{\mathbf{u}_{tw}}{n_{steps}} \tag{3.10}$$

where each step has an equal time step, Δt. Finally, nodal velocities, $\mathbf{v}_{tw}$, are calculated:

$$\mathbf{v}_{tw} = \frac{\mathbf{u}_{incr}}{\Delta t} \tag{3.11}$$

The time steps are chosen to be several orders of magnitude smaller than normal, such that the twin is inserted relatively rapidly, maintaining the difference in shear rates between deformation twinning and crystallographic slip.

In summary, motion due to twinning is applied to individual twin regions by considering the nodal points within said regions. The nodal points are mapped to their expected twinned locations via the application of essential boundary conditions in the form of nodal velocities. These velocities are found with knowledge of the parent crystal's crystallographic orientation and the twin system in question, via the calculation of the expected nodal displacement due to twinning, and the assumed time step for the twin motion to be applied. The twin motion is applied over a number of incremental steps to aid in convergence of the solution. Application of twin motion to a discrete region

via essential boundary conditions ensures that a discrete region of the aggregate experiences the proper motion associated with a twin event. This is unique among existing twin modeling efforts, as existing models consider the shear due to twinning only at material points rather than across discrete regions.

3.2.2 Lattice Reorientation

In combination with the deformation associated with twinning, the crystal lattice within the twin region experiences a large reorientation. During a twinning event, the orientation of the twin must be calculated based on the parent grain's orientation and the twin system in question. The orientation of the crystal is described using a rotation from the crystal to the sample frame, $\mathbf{R}^{C,S}$ (see: Chapter 2.1.2). Orientations are considered for each element in the mesh. As such, all calculations below operate on values for each element within a twin region.

At some point in deformation, the current orientation of the crystal is likely to change due to some rotation of the lattice, $\mathbf{F}^R$. The current orientation, $\mathbf{R}^{C,S}$, is thus described as a function of the initial orientation, $\mathbf{R}_0^{C,S}$:

$$\mathbf{R}^{C,S} = \mathbf{R}_0^{C,S}\mathbf{F}^R \tag{3.12}$$

Upon twinning, the lattice reorients to a specific configuration. Focusing on the twin of the first kind description, the reorientation of the lattice is described as a reflection of the crystal lattice about the twin plane (or, mathematically, a 180° rotation about the twin plane normal, Figure 2.6). This reorientation of a crystal's rotation matrix is described by van Houtte [52] as:

$$\mathbf{R}_{tw}^{C,S} = \boldsymbol{\Theta}\mathbf{R}_{pt}^{C,S} \tag{3.13}$$

where $\mathbf{R}_{tw}^{C,S}$ is the orientation of the twin region, $\mathbf{R}_{pt}^{C,S}$ the current orientation of the parent grain which twins at some time step, and $\boldsymbol{\Theta}$ is:

$$\boldsymbol{\Theta} = 2\boldsymbol{\nu} - \mathbf{I} \tag{3.14}$$

where $\boldsymbol{\nu}$ is constructed as the dyadic product between the direction cosines of the twin plane normal.

For ease of implementation, this same rotation is better represented by an angle-axis parameterization, especially the quaternion. The rotation for a twin of the first kind, $\mathbf{q}_{tw}$, is represented by a quaternion with $\omega = 180°$ and $\mathbf{n} = \mathbf{n}_{tw}$, which reduces to:

$$\mathbf{q}^{tw,pt} = \begin{Bmatrix} 0 \\ \mathbf{n}^{tw} \end{Bmatrix} \tag{3.15}$$

Similar to Equation 3.13, the reorientation of the lattice due to twinning is defined as the quaternion product between the reorientation rotation and the orientation of the crystal that is twinning:

$$\mathbf{q}^{tw} = \mathbf{q}^{tw,pt}\mathbf{q}^{pt} \tag{3.16}$$

where $\mathbf{q}^{pt}$ is the orientation of the crystal prior to twinning, converted from $\mathbf{R}^{C,S}$ of Equation 3.12. Similarly, $\mathbf{q}^{tw}$ may be converted back to a rotation matrix, $\mathbf{R}^{tw}$.

At this point, current values for the orientation of the lattice and the necessary rotation from the initial orientation may be update in Equation 3.12, such that:

$$\begin{aligned} \mathbf{R}^{C,S} &= \mathbf{R}^{tw} \\ \text{and } \mathbf{F}^{R} &= \left(\mathbf{R}_0^{C,S}\right)^T \mathbf{R}^{tw} \end{aligned} \tag{3.17}$$

Here, the current orientation is set to the twinned orientation, and the necessary rotation is a combination of the twin reorientation and the reorientation accrued prior to the twin event.

As the deformation of twin is applied over a number of steps as described in the previous section, various schemes are considered for reorientation of the lattice due to twinning:

1. Pre-reorientation
    - The lattice is reoriented at the first step imposing twin motion, and held fixed throughout the imposition of the twin motion
2. Post-reorientation
    - The lattice is reoriented at the final step imposing twin motion
3. Incremental reorientation
    - The lattice is incrementally reoriented at each step such that it reaches the twinned orientation after all twin steps

Each of these reorientation schemes are non-physical. Pre-reorientation and post-reorientation are both unrealistic, as the lattice orientation does not suddenly jump at the beginning or end of the twin motion. Similarly, an incremental reorientation is unrealistic as the lattice does not physically rotate about the twin plane to reach a twinned orientation (the twin of the first kind reorientation description is merely a construct, not an actual lattice motion). Instead, the crystal lattice is imperfect during the twin motion, as dislocations deform the lattice throughout the motion until arriving at their new position as a "perfect" lattice with a new crystallographic orientation. Discrete dislocations are not considered in this framework, as it follows a continuum approach to material modeling. Implementing multiple reorientation schemes, however, allows for the study of their effect on results, considering the pre-twin and post-twin states.

In summary, the crystallographic orientation within a discrete twin region is reoriented based on the crystallographic orientation of the parent grain and the twin system in question. This essentially creates new apparent grain boundaries, which will effect the deformation fields both inside and outside of the twin region. As the twin motion is applied over a number of incremental steps, various reorientation schemes are considered to arrive at the final twinned orientation. Again, this is a consequence of considering discrete twin regions rather than homogenizing responses as in existing modeling schemes, which would not allow for the consideration of new grain to grain interactions.

3.2.3 Calculation of Work

Existing twin modeling schemes - by homogenizing the deformation response at local points - only allow for the calculation of average work rates at local points. The presented framework, however, allows for more precise calculations of both local (element by element) or global energy metrics. This, in turn, allows for the possibility to study of the energy associated with a twinning event in a way that existing models do not afford.

The work rate for a given deformation step of a simulation is defined using work conjugate pairs [17] of the Cauchy stress and either the deformation rate or the plastic deformation rate (whether calculating the total work rate, $\dot{W}$, or the plastic work rate, $\dot{W}^P$, respectively). Equation 3.18 details the calculation of the work rates for the each element following standard integration over an element by means of Gauss quadrature.

$$\begin{aligned} \dot{W} &= \sum_{i}^{n_{qp}} w_i J_i \left(\boldsymbol{\sigma}_i : \mathbf{D}_i\right) \\ \dot{W}^P &= \sum_{i}^{n_{qp}} w_i J_i \left(\boldsymbol{\sigma}_i : \mathbf{D}_i^P\right) \end{aligned} \tag{3.18}$$

where n_{qp} is the number of Gauss quadrature points in the element. Additionally w_i is

the quadrature weight, J_i is the determinant of the Jacobian, $\boldsymbol{\sigma}_i$ is the Cauchy stress, and $\mathbf{D}_i/\mathbf{D}_i^P$ the total and plastic deformation rate tensors, all evaluated at the quadrature points of a given element, i. The expressions $\boldsymbol{\sigma}_i : \mathbf{D}_i$ and $\boldsymbol{\sigma}_i : \mathbf{D}_i^P$ are the inner products between the Cauchy stress and the deformation rate tensors. A total work rate is calculated for the entire polycrystal, where n_{el} is the number of elements:

$$\begin{aligned} \dot{W}_{tot} &= \sum_{j}^{n_{el}} \dot{W}_j \\ \dot{W}_{tot}^P &= \sum_{j}^{n_{el}} \dot{W}_j^P \end{aligned} \tag{3.19}$$

Work rates are calculated using the stresses and deformation rates printed at the end of a deformation step. As such, the work for a given step is approximated given the time step, Δt, using the trapezoidal rule:

$$\begin{aligned} W_{step} &= \frac{\Delta t}{2}\left(\dot{W}_{tot} + \dot{W}_{tot_n}\right) \\ W_{step}^P &= \frac{\Delta t}{2}\left(\dot{W}_{tot}^P + \dot{W}_{tot_n}^P\right) \end{aligned} \tag{3.20}$$

where the quantities $\dot{W}_{tot_n}$ and $\dot{W}_{tot_n}^P$ are the work rates at the end of the previous deformation step.

Additionally, with the work rate and the work known for every time step and for every element, the global and local changes in temperature may be approximated. Assuming that the work is entirely converted to heat, the work is related to a change in temperature as:

$$\Delta T = \frac{W}{\rho V C_p} \tag{3.21}$$

where W is the work for a region, ρ is the density of the material (assumed to be constant for titanium at $\sim 4430 \frac{\text{kg}}{\text{m}^3}$), V is the volume of a region, and C_p is the specific heat (which is again assumed to be constant for titanium at $\sim 540 \frac{\text{J}}{\text{kg K}}$ [30]).

3.2.4 Implementation

Figure 3.7 illustrates the flow of a simulation in which deformation twinning is imposed on a region. After an arbitrary number of deformation steps, a twin is inserted. After initialization of the first twin step, but prior to iteration for the solution, the boundary conditions are altered to impose the motion of the twin. This is only done on the first step, as the boundary conditions remain unchanged until reverted back to the original boundary conditions on the last twin step. Otherwise, the solver progresses as it normally would. Various paths are shown for the three different reorientation schemes (denoted as "R.S." in the flowchart).

The extended framework relies heavily on the existing crystal plasticity finite element framework described in Chapter 2.2. Little is changed to the finite element implementation detailed in Appendix A, as the solution method in the extended framework relies on the existing constitutive models. Consequently, detailed discussion of implementation is omitted, as it is largely redundant. Essentially, the only necessary changes to the existing routines are to impose new boundary conditions and reorient the lattice (described in the previous two sections) at some point in deformation to insert the twin, and to revert back to the original boundary conditions to continue the deformation of the entire polycrystal after the twin motion has been imposed.

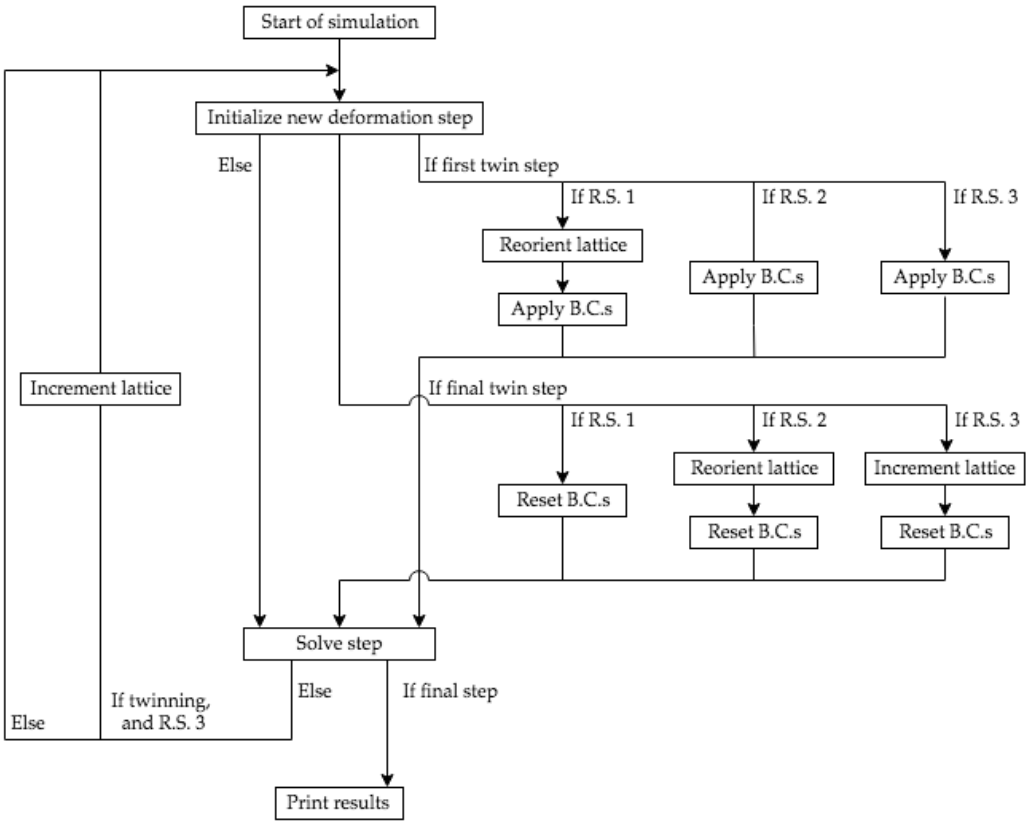

Figure 3.7: Flowchart depicting insertion of deformation twin during a simulation.

CHAPTER 4

SIMULATIONS AND RESULTS

This chapter begins with an outline of the simulations performed and their conditions, followed by representative results. Instantiations, changes to instantiations, and model parameters are chosen, and their values discussed. Next, results are shown, beginning with a single crystal simulation to clearly highlight the ability to map the motion of the twin on a mesh and reorient the crystal within the mesh. The following sections then focus on a polycrystalline instantiation to study the effects of a twin embedded in an aggregate. Results from various simulations are shown, including those with changes in the reorientation scheme, changes in twin width, and changes in the spatial location of the twin within a grain.

4.1 Simulations

To probe various aspects of the deformation twinning framework, various cases are investigated. As such, various instantiations are produced. First, a single crystal instantiation is constructed. The domain is chosen as a rectangular prism of initial lengths $l_x = l_y = 1\text{mm}$ and $l_z = 2\text{mm}$ and twin regions of width $w = 0.1\text{mm}$. The same orientation is assigned to all lamellar regions within the domain to produce a single crystal. The orientation of the crystal is chosen as (in the Rodrigues' parameterization):

$$\mathbf{r} = \begin{pmatrix} 0.0 \\ 0.0 \\ -0.2679 \end{pmatrix} \tag{4.1}$$

which corresponds to a rotation of -30° about the crystal's $\langle c \rangle$-axis. The crystallographic orientation is chosen such that the $\langle c \rangle$-axis is aligned with the tensile direction,

and the twin direction is in the sample $x - z$ plane, as illustrated in Figure 4.1. Indeed, the twin plane normal and shear direction are calculated as:

$$\mathbf{n}^{tw} = \begin{pmatrix} 0.6757 \\ 0.0 \\ 0.7372 \end{pmatrix}, \mathbf{d}^{tw} = \begin{pmatrix} -0.7372 \\ 0.0 \\ 0.6757 \end{pmatrix} \tag{4.2}$$

For the single crystal simulations, a twin is inserted at a point near the center of the sample.

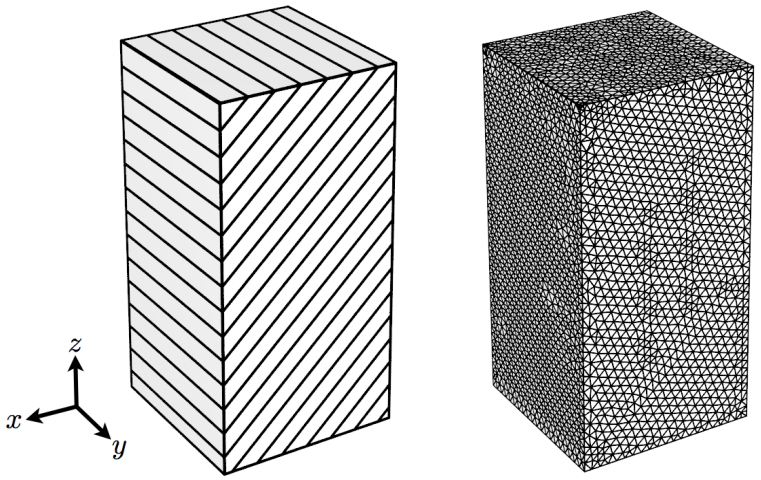

(a) (b)

Figure 4.1: (a) Single crystal discretized into lamella, and (b) its mesh.

A Laguerre tessellation is employed to create an aggregate of grains for use in simulations of twins embedded in polycrystalline aggregates. The tessellation is constructed in a cubic domain of initial edge length $l = 1$mm. The Laguerre target distributions for grain size and shape are set to Dirac distributions in an effort to create an equiaxed microstructure (Figure 4.2(a)). A single grain is chosen for inspection as it resides near the center of the aggregate (Figure 4.2(b)).

The grain's orientation is set to the same orientation in Equation 4.1, such that when discretized into twin regions (Figure 4.3), it has the same twin normal and shear di-

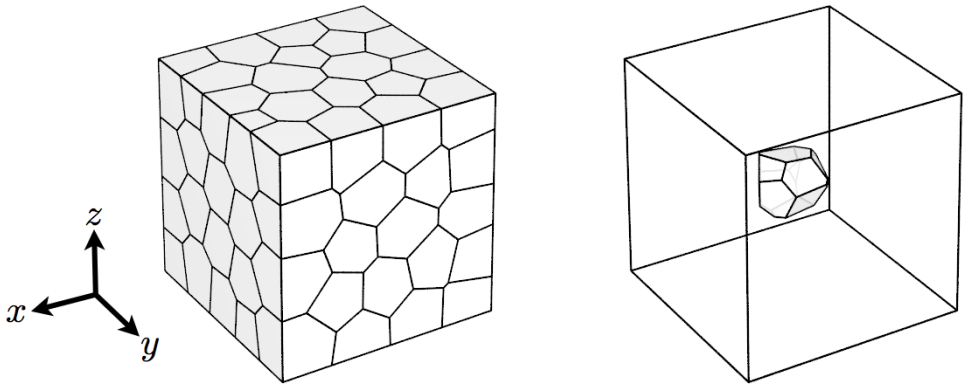

(a) (b)

Figure 4.2: (a) A domain divided into grains, (b) a single grain at the center of the aggregate (shown at its location in the domain), which may be further discretized into twin regions.

rection described in Equation 4.2. Other grain orientations in the aggregate are chosen at random - that is, the aggregate is otherwise assumed to have a uniform orientation distribution. As an aside, Laguerre tessellations with multiple grains may also be used to represent twins embedded within a single crystal by simply assigning the same orientation to all grains within the aggregate. Multiple instantiations are produced with various twin region widths. Figure 4.3 shows the center grain of the polycrystal shown in Figure 4.2(a) discretized into twin regions of widths w = 0.0025mm, w = 0.005mm, and w = 0.01mm.

While Ti-6Al-4V does not exhibit deformation twinning due to its high aluminum content [75], its model parameters are chosen for this study. This is done as Ti-6Al-4V possesses elastic and plastic parameters that are representative of a large class of hexagonal crystals - specifically in the character of the directional elastic modulus [126], and relative initial slip system strengths [33]. The high relative strength of the pyramidal system (nearly twice that of the basal system) would - in similar alloys - facilitate the development of deformation twinning. Additionally, Ti-6Al-4V exhibits little harden-

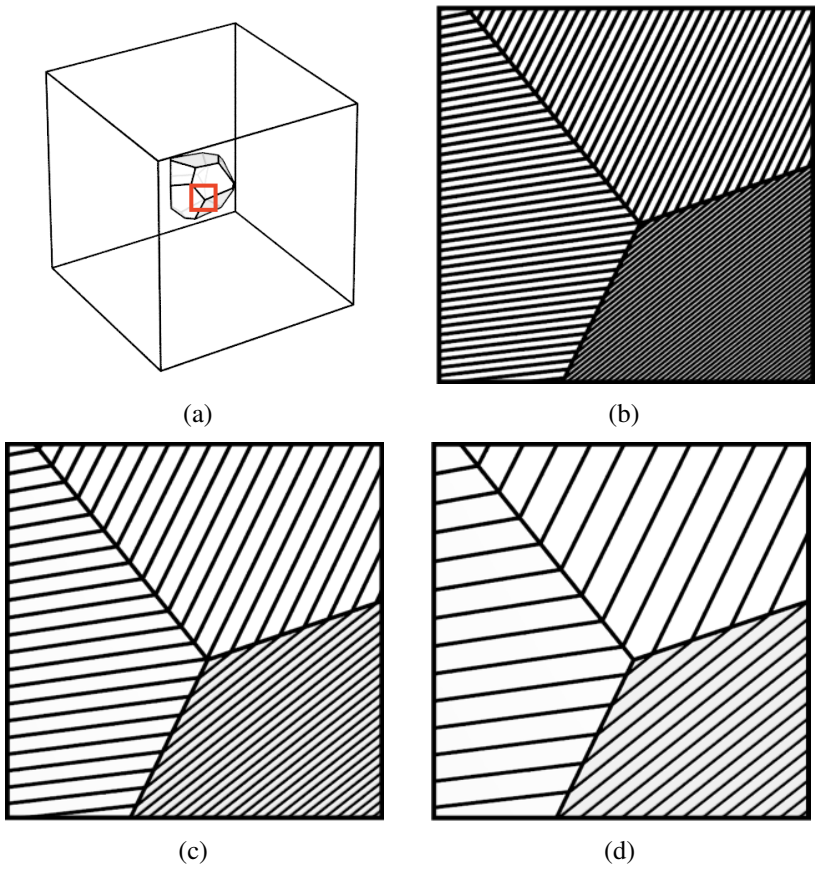

Figure 4.3: (a) Grain (with region of interest highlighted) discretized into twin widths of (b) $w = 0.0025$mm, (c) $w = 0.005$mm, and (d) $w = 0.01$mm.

ing, thus reducing that complication in the present study. Simulation parameters are detailed in Chapter B.2.2, summarized in Tables B.2.2, B.3 (Strength Set 1), and B.5.

In all cases, only the $\{1\,0\,\bar{1}\,2\}$ twin system is considered when instantiating twin regions. All samples are extended in the "z" direction of the sample frame. Grip boundary conditions, as described in Chapter 3.2.1 are employed for all simulations. All instantiations are extended in their "z" directions with velocities of $v_z = 0.01\frac{\text{mm}}{\text{s}}$. Each simulation with gage length $l = 1$mm is performed with the time steps (displacement steps) listed Table 4.1 (simulations with gage length $l = 2$mm follow the same steps, though each Δt is double that listed). Note that different time steps are necessary to achieve the same macroscopic strain due to the different gage lengths. The table is divided with a

horizontal line at the point at which the twins are inserted - 0.5% macroscopic strain.

The strain state at which twins are inserted is chosen at an arbitrary point in the macroscopic elastic regime, as plastic flow begins prior to macroscopic yield (Appendix B), and twins have been witnessed activating prior to the pyramidal slip system. Twins are inserted over a number of steps, $n_{steps} = 10$, with time steps of $\Delta t = 0.0001$s, such that the twin is inserted over a total time of $t = 0.001$s. Recall, the extension of the polycrystal is momentarily paused during the insertion of a twin.

Note that after the twin is inserted, a number of relatively small time steps are taken to aid in convergence of the solver. The deformation path for the simulations performed with gage length $l = 1$mm is illustrated in Figure 4.4. Results are printed at the end of every step listed in Table 4.1.

Step Numbers	Δt (s)	ϵ_{macro} (%)
1-5	0.100	0.500
6-10	0.001	0.505
11	0.005	0.510
12	0.040	0.550
13	0.050	0.600
14-27	0.100	2.000

Table 4.1: Deformation paths used in simulations with gage length $l = 1$mm.

4.2 Results of Single Crystal Simulations

The simulation of the single crystal specimen allows the inspection of the twin state without the complication of neighboring grains. Specifically, the reorientation and motion of the twin may be confirmed. The orientation described in Equation 4.1 describes a crystal with its $\langle c \rangle$-axis aligned with the sample's "z" direction (a deviation of 0°). The

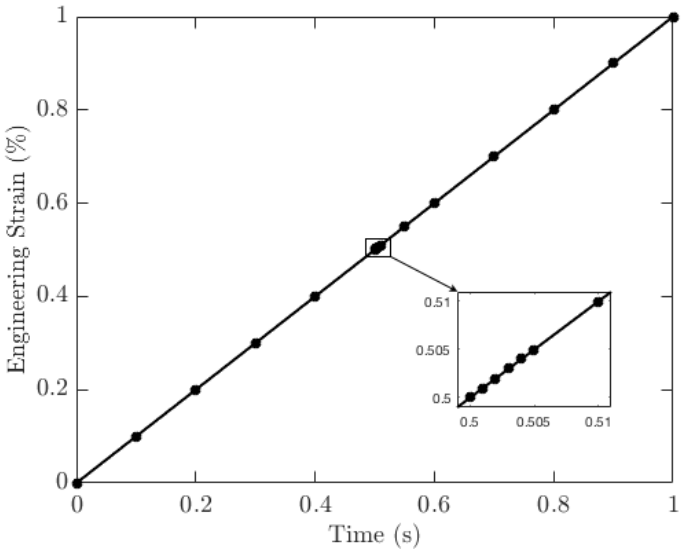

Figure 4.4: Illustration of load steps taken in simulations (specifically with gage length l = 1mm).

expected twin orientation for the assumed twin system is:

$$\mathbf{r} = \begin{pmatrix} -0.2455 \\ 0.9162 \\ -0.2679 \end{pmatrix} \tag{4.3}$$

This orientation has a $\langle c \rangle$-axis deviation of approximately 85° for the $\{1\,0\,\bar{1}\,2\}$ twin system. In other words, the crystal is expected to rotate such that the $\langle c \rangle$-axes of the twin and the parent grain are spread by 85°. This value is constant for a fixed $\frac{c}{a}$ ratio and twin system.

Average orientations for the parent grain and twin are gathered after the twin event (at the ends of step 6 in Table 4.1). Table 4.2 lists these orientations, and the calculated deviation between the $\langle c \rangle$-axes of the parent grain and twin. This is seen visually in Figure 4.5, which shows a twin in a three dimensional polycrystal. Displacements are exaggerated to highlight the deformation due to twinning.

Results indicate that the simulated spread between the $\langle c \rangle$-axes of the simulations

R.S.	Parent $\mathbf{r}_{avg}$	Twin $\mathbf{r}_{avg}$	Deviation (°)
1	$\begin{pmatrix}-0.0006\\0.0024\\-0.2679\end{pmatrix}$	$\begin{pmatrix}-0.2406\\0.9252\\-0.2599\end{pmatrix}$	85.2913
2	$\begin{pmatrix}-0.0007\\0.0028\\-0.2679\end{pmatrix}$	$\begin{pmatrix}-0.2393\\0.9133\\-0.2619\end{pmatrix}$	84.4864
3	$\begin{pmatrix}-0.0007\\0.0024\\-0.2679\end{pmatrix}$	$\begin{pmatrix}-0.2411\\0.9247\\-0.2621\end{pmatrix}$	85.2172

Table 4.2: Average parent grain and twin orientations immediately after insertion of deformation twin in a single crystal specimen for the various reorientation schemes (R.S.). Deviation refers to the angle between the $\langle c \rangle$-axes of the crystals.

performed with each reorientation scheme. In each case, the spread is calculated to within a degree of the expected spread of 85°. Generally, slight variation from the theoretical value is to be expected, considering the development of misorientation in the parent grain that is likely to occur during the application of the twin. Furthermore, variation between the spreads calculated for each reorientation scheme is expected, as the development of misorientation in the parent grain during the application of the twin is dependent on the interaction between the twin and the parent grain.

The motion of the twin is also inspected to confirm that the proper shear due to twinning is applied. The nodal points of the twin region after the twin event are considered (at the beginning of step 6 in Table 4.1). Expected displacements are calculated using the deformation gradient calculated using $\mathbf{n}^{tw}$ and $\mathbf{d}^{tw}$ in Equation 4.2, and a shear of $S = 0.167$. Expected and actual displacement magnitudes are compared, and results in the form of a linear regression correlation coefficients, r, are presented in Table 4.3.

Considering the simulated displacements of the nodes within the twin region and the theoretical motions reveals correct motion mapping. Table 4.3 shows that both the displacement directions and magnitudes of the nodes within the twin region are cor-

	R.S. 1	R.S. 2	R.S. 3
r_{mag}	1	1	1
r_{dir}	1	1	1

Table 4.3: Correlation coefficients for the displacement magnitudes, r^2_{mag}, and directions, r^2_{dir}, calculated for the various reorientation schemes (R.S.)

rectly mapped using the boundary conditions described in Chapter 3.2.1. Comparing the expected motion to the motion predicted by the simulation reveals that there is a one-to-one correlation. This confirms that the boundary conditions are applied properly, and the solver correctly maps the motion of the twin. Figure 4.5, additionally, shows that the motion is accommodated by the remainder of the mesh. Reorientation schemes did not effect the results of the twin motion, as they do not effect the applied boundary conditions.

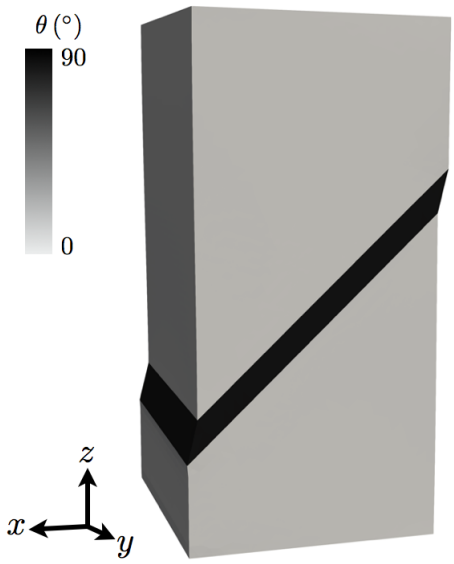

Figure 4.5: Deviation of the crystal $\langle c \rangle$-axis from the loading direction, θ, at the point directly after the twinning event plotted on the deformed mesh (exaggerated 3x). Results from simulation performed with reorientation scheme 1.

Overall, results indicate that the motion due to deformation twinning is correctly implemented. Additionally, each reorientation scheme is considered valid in terms of

their ability to set the twin's orientation within reasonable degrees of accuracy. Investigation of twins embedded in polycrystalline aggregates can proceed with confidence in the framework's ability to insert deformation twins.

4.3 Results of Polycrystal Simulations

Results of the simulations performed on polycrystalline aggregates are summarized here. First, results showing the reorientation of the crystal lattice within the twin region are presented (Figures 4.6 and 4.7). Three dimensional visualizations of the grain after twinning is shown in Figure 4.8, where the deformation is exaggerated to highlight the deformation due to twinning on a complex, three dimensional domain. This is followed by a presentation of the stress field prior to the twinning event (Figure 4.9), and the stress field after the twinning event on an interior slice of the polycrystal at its center, looking at the "$x - z$" plane (Figures 4.10, 4.11, and 4.12), for polycrystals instantiated with twin regions of width $w = 0.0025$mm, $w = 0.005$mm, and $w = 0.01$mm, respectively. Figures 4.10, 4.11, and 4.12 additionally detail the results depending on which reorientation scheme is employed. Figure 4.13 shows the von Mises stress on a different slice through the sample (at its center, looking at the "$y - z$" plane), to highlight the complex three dimensional stress state surrounding the twin region.

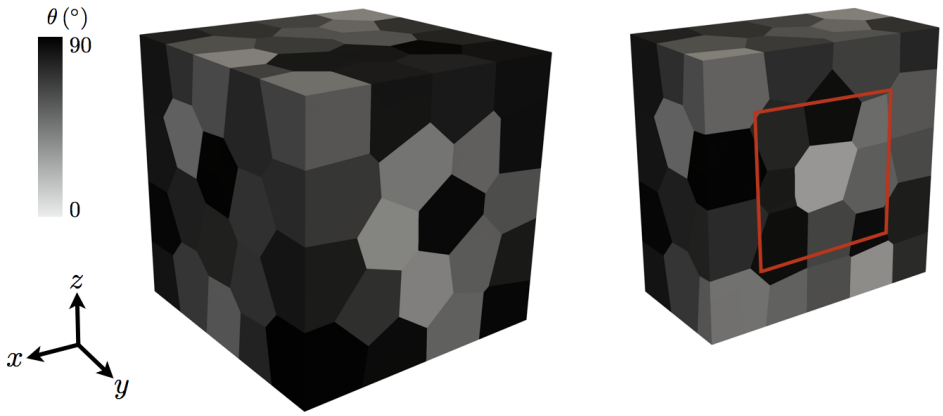

(a) (b)

Figure 4.6: (a) Aggregate, and (b) slice through the center of the aggregate with approximate region of interest outlined, detailing the deviation of the crystal $\langle c \rangle$-axis from the loading direction, θ.

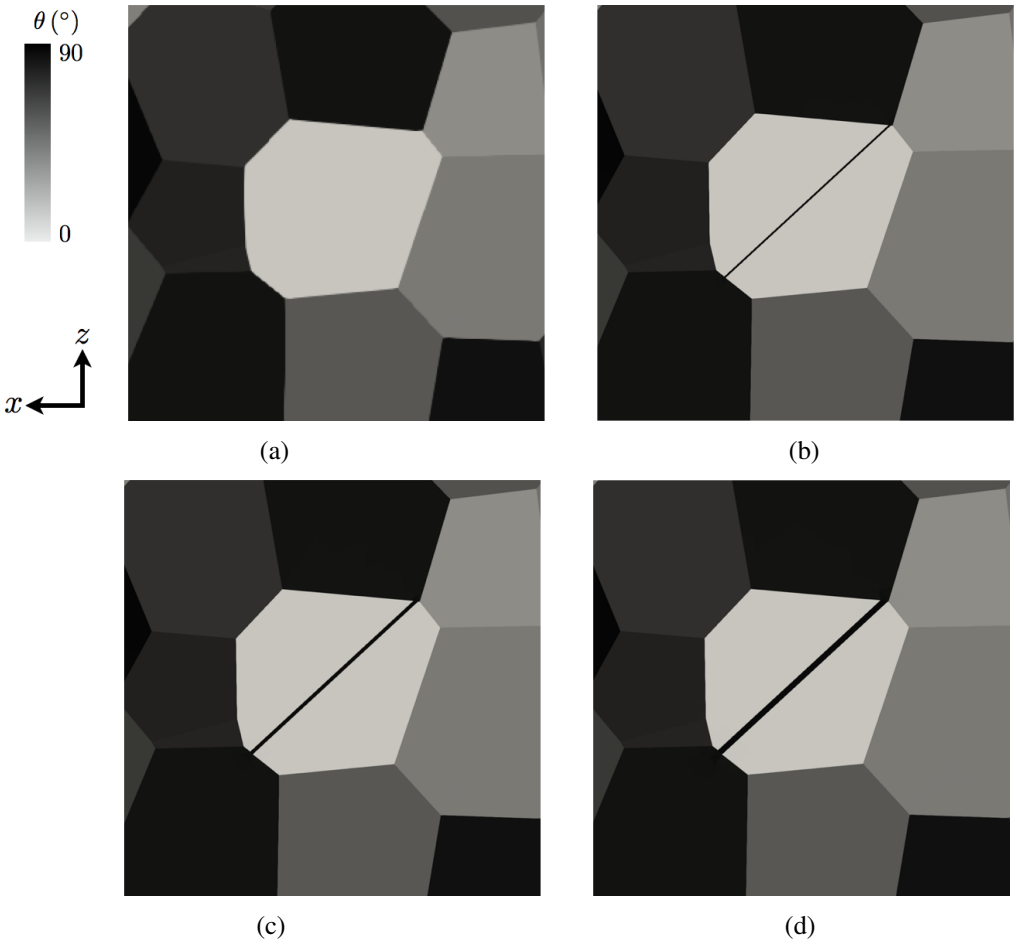

Figure 4.7: (a) Enlargement of grain discretized for twinning, from the same slice as Figure 4.6. Results from simulations employing reorientation scheme 1 and a twin width of (b) w = 0.0025mm, (c) w = 0.005mm, and (d) w = 0.01mm.

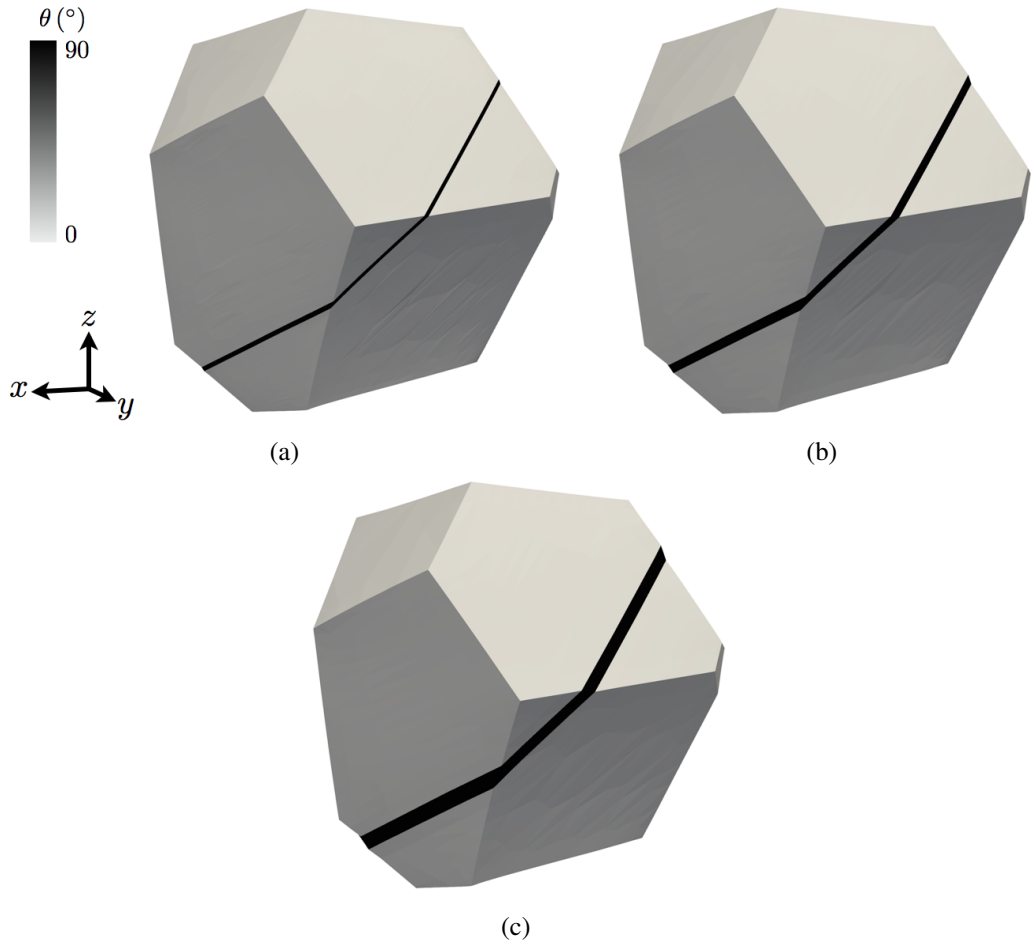

Figure 4.8: Three dimensional visualization of the deviation of the crystal $\langle c \rangle$-axis from the loading direction, θ, at the point directly after the twinning event plotted on the deformed mesh (exaggerated 3x). Results from simulations employing reorientation scheme 1, and a twin width of (a) $w = 0.0025$mm, (b) $w = 0.005$mm, and (c) $w = 0.01$mm. Refer to Figure 4.3 for visualizations of undeformed structures.

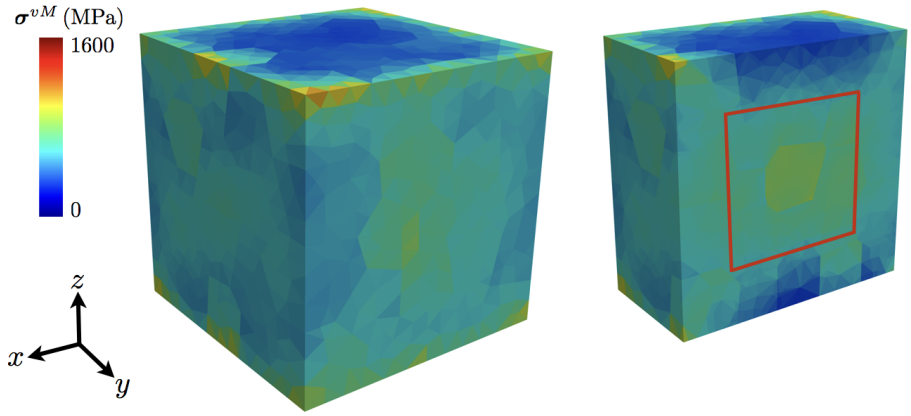

(a) (b)

Figure 4.9: (a) Aggregate, and (b) slice through the center of the aggregate with approximate region of interest outlined, detailing the von Mises stress prior to twinning.

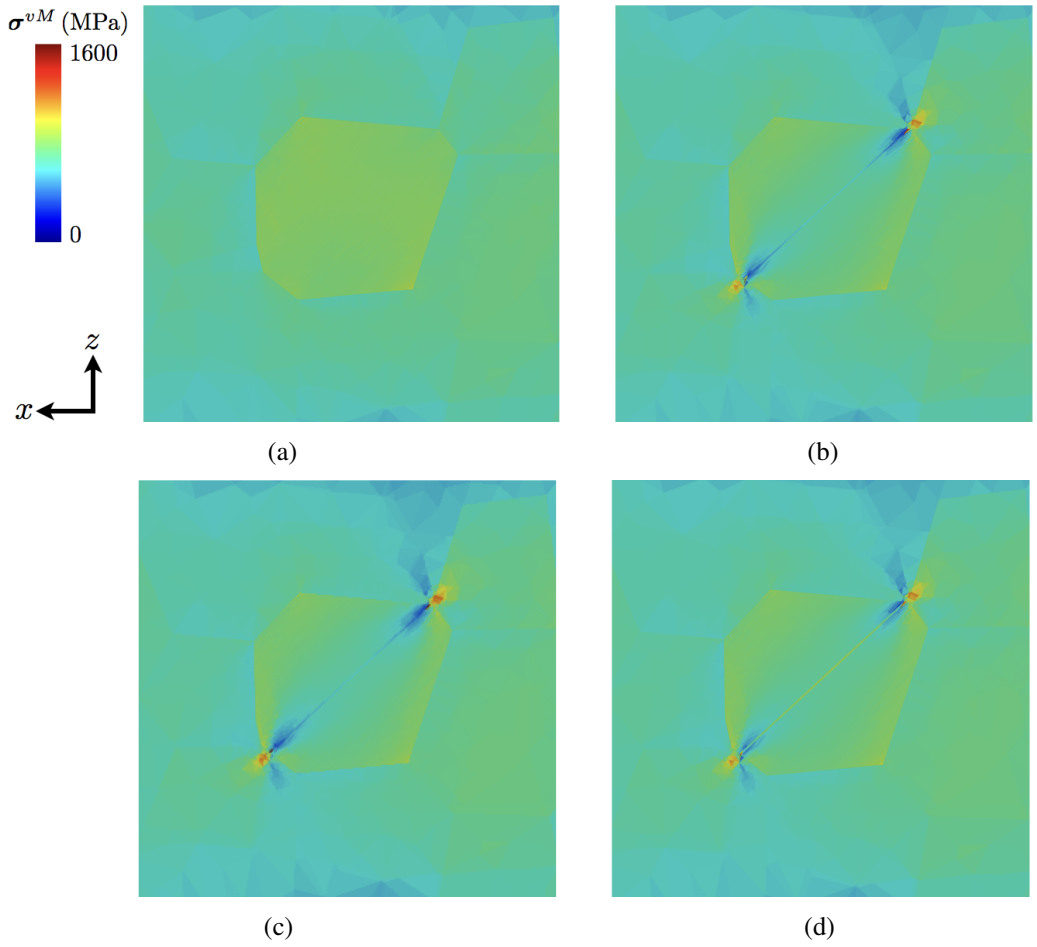

Figure 4.10: (a) Enlargement of grain discretized for twinning detailing the von Mises stress prior to twinning, and the von Mises stress after twinning for the simulations with twin width w = 0.0025mm employing (b) reorientation scheme 1, (c) reorientation scheme 2, and (d) reorientation scheme 3.

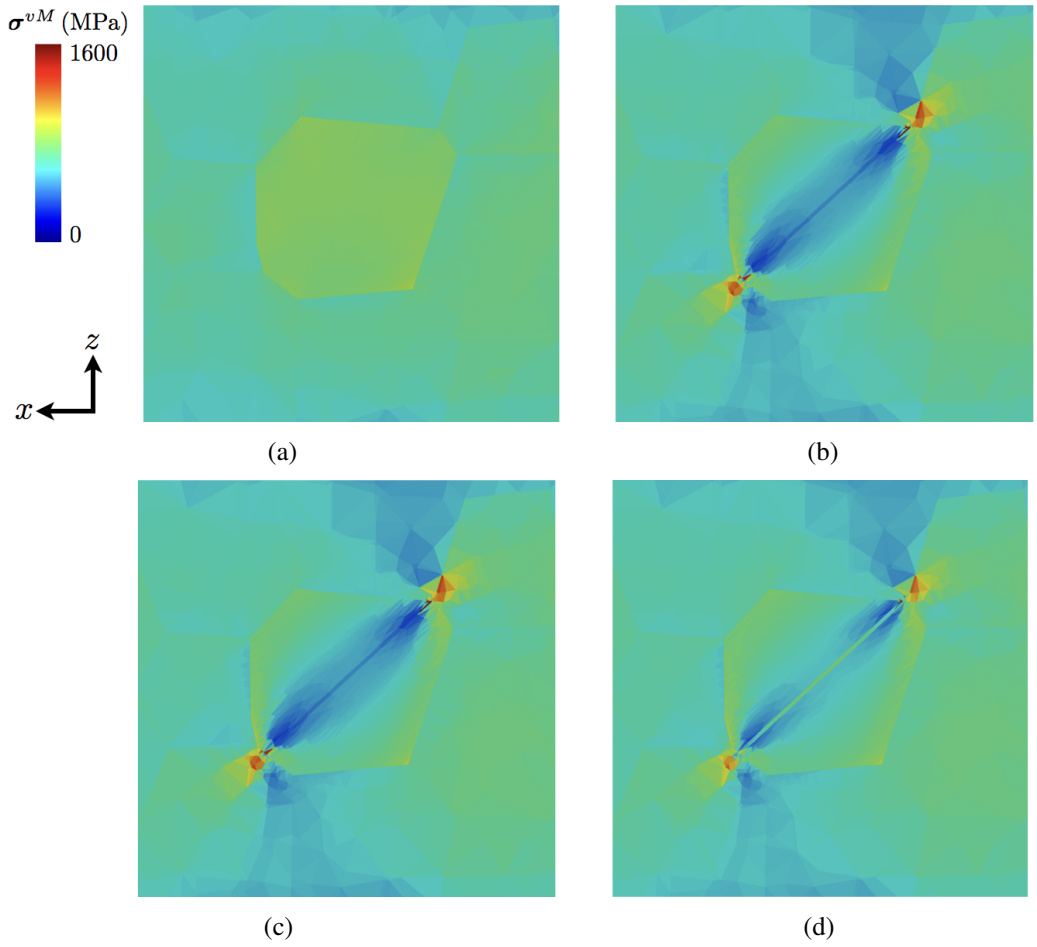

Figure 4.11: (a) Enlargement of grain discretized for twinning detailing the von Mises stress prior to twinning, and the von Mises stress after twinning for the simulations with twin width w = 0.005mm employing (b) reorientation scheme 1, (c) reorientation scheme 2, and (d) reorientation scheme 3.

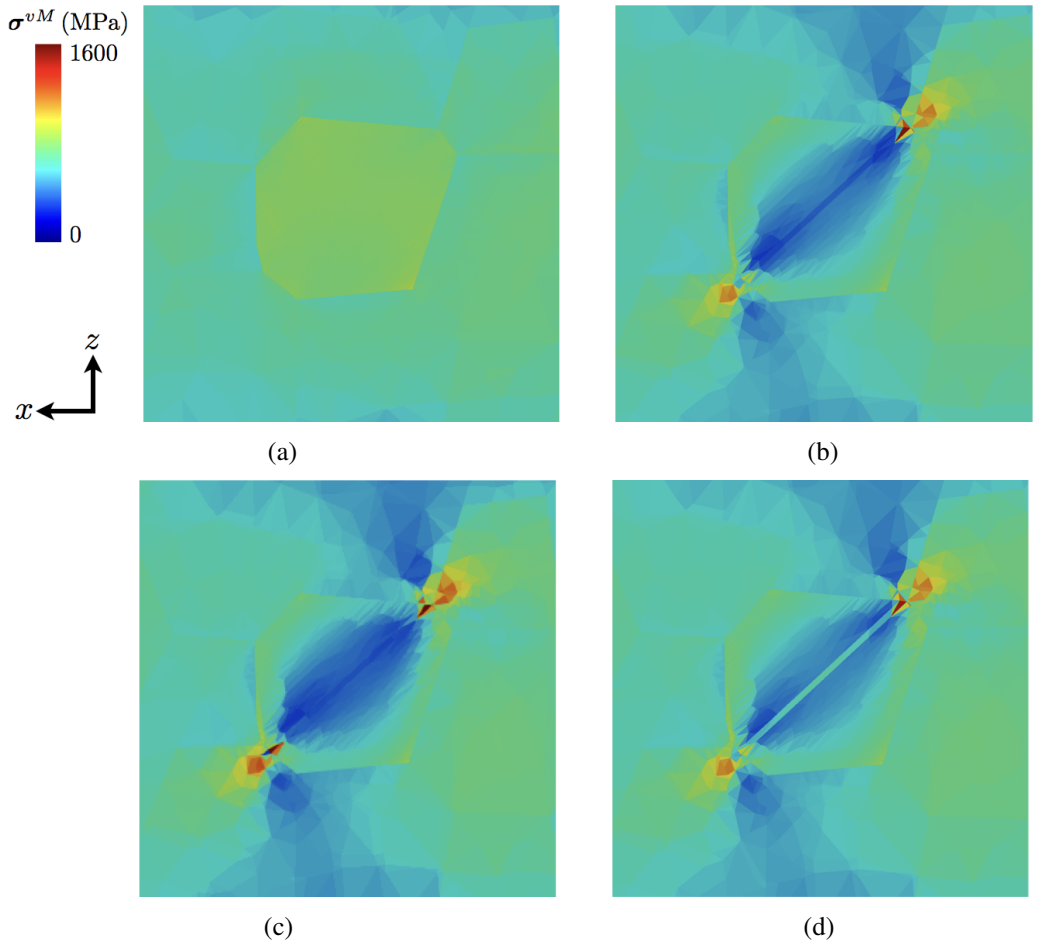

Figure 4.12: (a) Enlargement of grain discretized for twinning detailing the von Mises stress prior to twinning, and the von Mises stress after twinning for the simulations with twin width w = 0.01mm employing (b) reorientation scheme 1, (c) reorientation scheme 2, and (d) reorientation scheme 3.

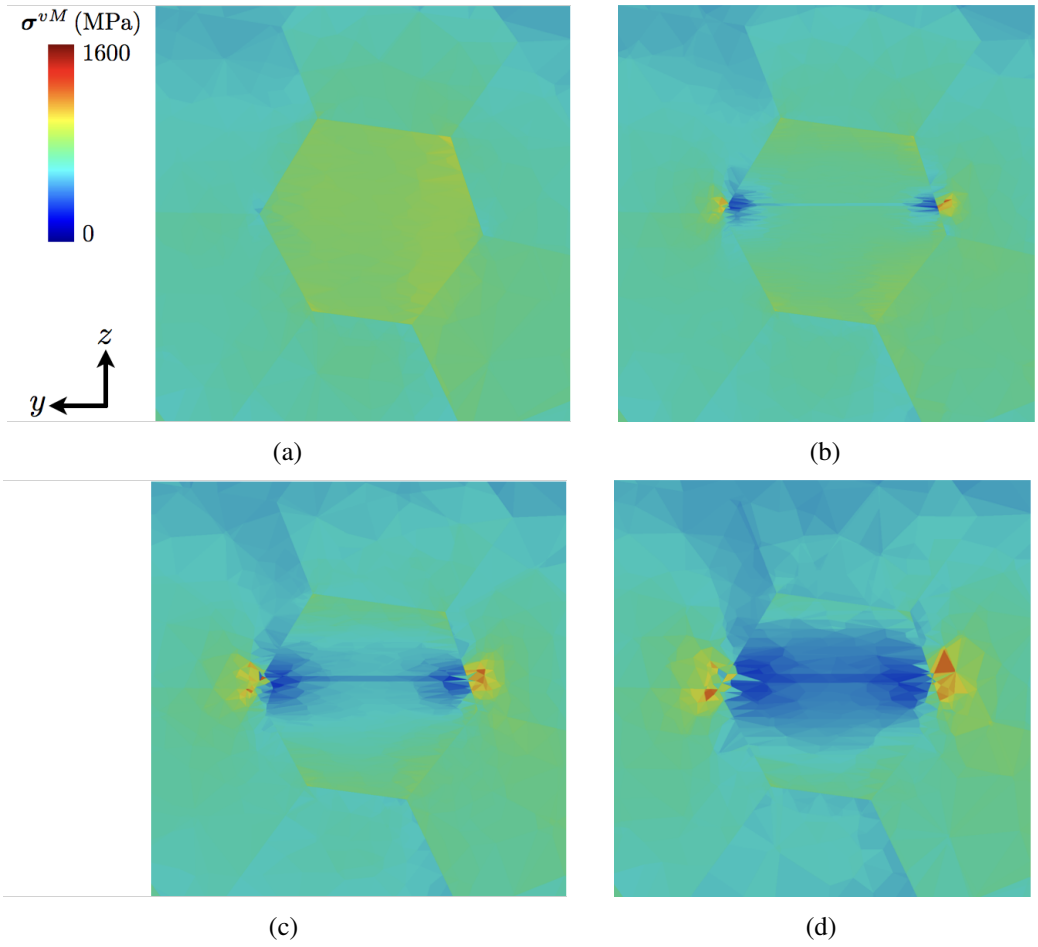

Figure 4.13: (a) Enlargement of grain discretized for twinning detailing the von Mises stress prior to twinning, and the von Mises stress after twinning for the simulations employing reorientation scheme 1, and a twin width of (b) $w = 0.0025$mm, (c) $w = 0.005$mm, and (d) $w = 0.01$mm.

CHAPTER 5

DISCUSSION

This chapter is devoted to the discussion of simulation results. Sections below detail descriptions and considerations of the simulations detailed in the previous chapter. First, stress states are investigated, followed by considerations of the work required to insert twins, and finally the calculation of slip activity within twin regions.

5.1 Stress Observations

Visualizing the von Mises stress allows for a qualitative comparison between the simulations performed with various twin widths and reorientation schemes. Figures 4.10, 4.11, and 4.12 show that the various reorientation schemes produce stress fields that are of similar qualitative character. High stress concentrations are observed at the twin tips, supporting some experimental observations [4]. Additionally, Figure 4.13 details the von Mises stress on a different slice through the polycrystal, perpendicular to the slice used in Figures 4.10, 4.11, and 4.12. This highlights the fact that the twin produces stress concentrations around its entire perimeter, rather than just at the twin tips.

Note the decrease in the effective stress in the parent grain around the twin region (compare to the stress state prior to twinning) which appears regardless of which reorientation scheme is used. While similar, there are clear qualitative differences. To quantify these differences, the average effective stress within the twin region and parent grain directly after twinning is calculated, and compared against the average effective stress in the parent grain prior to twinning (calculated to be approximately 810MPa). Table 5.1 shows the average von Mises stress within the twin region for each twin width

considered, as well as each reorientation scheme, while Table 5.2 shows the same information but for the parent grain. Stress states are likely different due to the evolution

	σ_{vM} (MPa)		
w (mm)	R.S. 1	R.S. 2	R.S. 3
0.0025	518	604	732
0.005	457	585	659
0.01	444	546	609

Table 5.1: Average von Mises stress within the twin region directly after twinning for the various simulations.

	σ_{vM} (MPa)		
w (mm)	R.S. 1	R.S. 2	R.S. 3
0.0025	720	706	721
0.005	647	630	650
0.01	588	580	595

Table 5.2: Average von Mises stress within the parent grain directly after twinning for the various simulations.

of the stress states due to the employment of various reorientation schemes. Each simulation experiences the same nodal motion when the twin is applied, though the crystal lattice is constrained in various ways depending on which reorientation scheme is employed. Reorientation schemes 1 and 2 reorient the lattice entirely in one step, while reorientation scheme 3 reorients incrementally. While the first 2 schemes consider only the prior orientation and the final orientation, the third scheme considers many orientations in between - which means the incremental calculation of stress at crystallographic orientations which could increase the stress. This potentially explains why reorientation scheme 3 consistently produces higher average stresses within the twin region than the other two reorientation schemes for this specific test.

Inspecting the stress components reveals more information concerning the stress field after the twinning event. This is best viewed by transforming the stress states to a coordinate system aligned with the characteristic twin directions. A frame, $\mathbf{e}^{tw}$ is

chosen, where $\mathbf{e}_1^{tw} = \mathbf{d}^{tw}$ and $\mathbf{e}_2^{tw} = \mathbf{n}^{tw}$. Figure 5.1 shows the component of stress in the direction of shear (the "11" component in the transformed frame) for simulations performed with reorientation scheme 1 after twinning (step 6 on Table 4.1). Results from the simulations employing the other reorientation schemes are omitted for the sake of brevity, but follow similar trends concerning the tension and compression regions at the twin tips. Note the arrows approximating the motion of the twin. Areas of tension

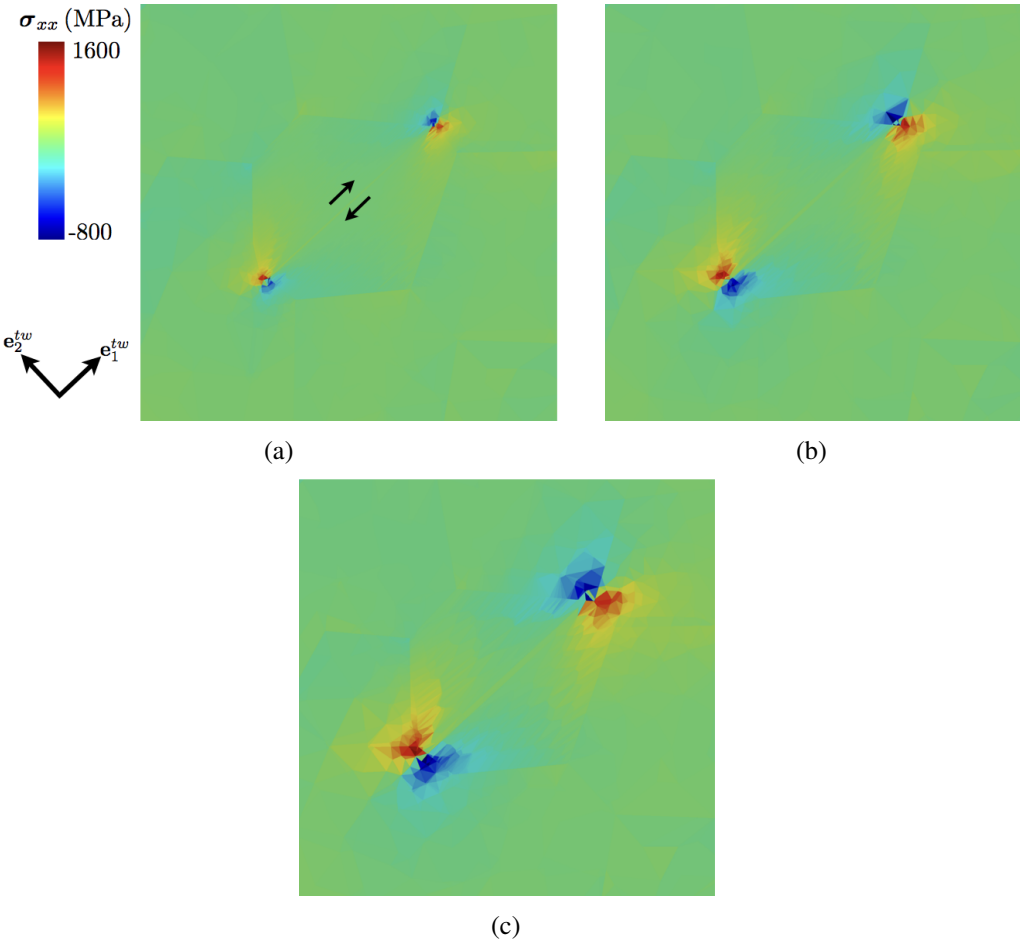

Figure 5.1: Component of stress along the direction of shear, for simulations employing reorientation scheme 1, with twin width (a) $w = 0.0025$mm (with arrows approximating the direction of motion for the twin region), (b) $w = 0.005$mm, and (c) $w = 0.01$mm.

and compression are caused at the twin tips extending into the neighboring grains, due to the opposing motion on either side of the twin region. As twin width is increased,

the volume effected by this motion is increased. Larger areas of neighboring grains are witnessed to have higher tensile or compressive stresses than the aggregate at large.

Viewing the resolved shear stress on the twin system after the twin event gives a comparison to similar studies on two dimensional mediums. In a study on two dimensional crystals utilizing a fast Fourier transform (FFT) solution method, Arul Kumar [71] notes that the resolved shear stress on the twin system experienced a drop within the twin region, and a sharp increase near the twin tips immediately after the twinning event. This is reproduced in full field studies utilizing a finite element scheme.

Figure 5.2 shows the resolved shear stress along a line through the center of the twin in the twin direction for simulations performed with a twin width of $w = 0.01$mm and employing the various reorientation schemes, while Figure 5.3 shows the same information for simulations with various twin widths employing only reorientation scheme 1. Boundaries of the twin regions are roughly shown with dashed lines. In general - the resolved shear stress on the twin system drops within the twin region, but experiences a sharp increase in neighboring grains.

The magnitude of the average drop is dependent on which reorientation scheme is employed, but more importantly on the width of the twin. Simulations performed with thinner twin widths experience a smaller average drop in the resolved shear stress within the twin region than those performed with wider twin widths (compare Figures 5.3(a) and 5.2(a)). Beyerlein assumes the driving mechanism for twin formation is the resolved shear stress on the twin plane (employing a pseudo-slip approach for twin nucleation). They postulate that a drop in the resolved shear stress within the twin region indicates an aversion to twin growth. As the macroscopic load is increased, and the resolved shear stress on the twin system increases, it reaches a threshold such that twin growth is favorable. Under this hypothesis, results here indicate the thin twin's possible ability

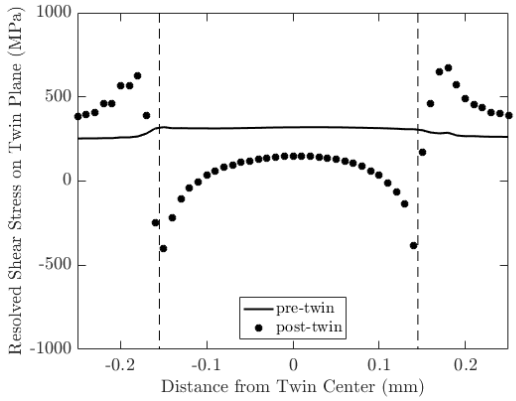

(a)

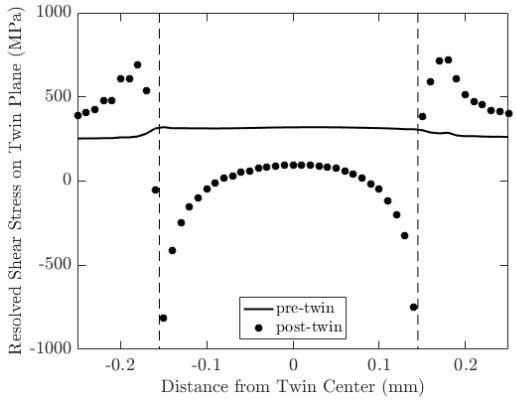

(b)

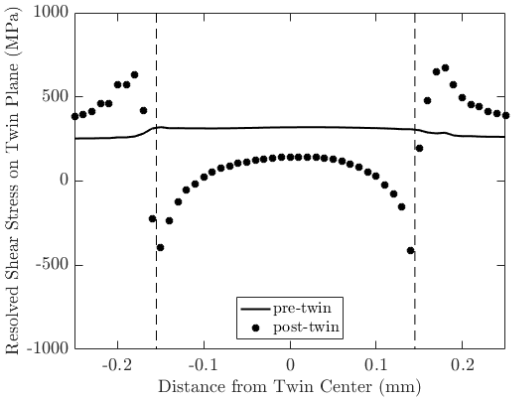

(c)

Figure 5.2: Resolved shear stress for the twin system along a line through the center of the twin in the twin direction, for simulations performed with twin width $w = 0.01$mm, employing (a) reorientation scheme 1, (b) reorientation scheme 2, and (c) reorientation scheme 3.

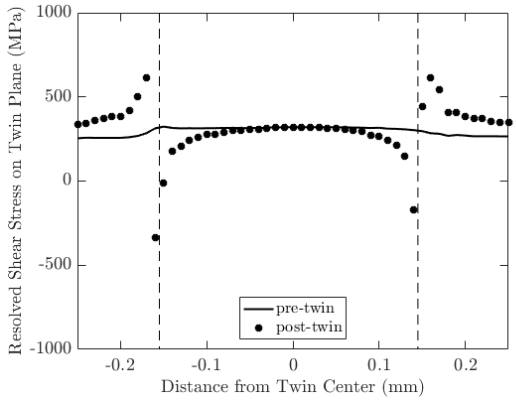

(a)

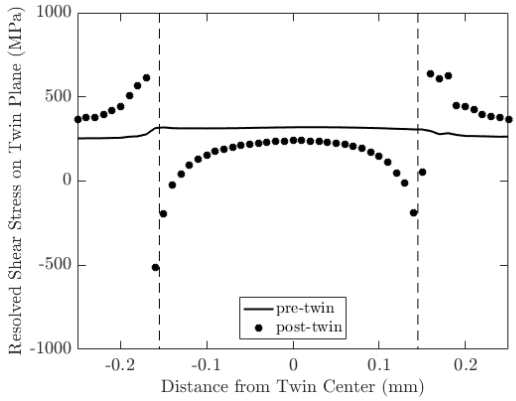

(b)

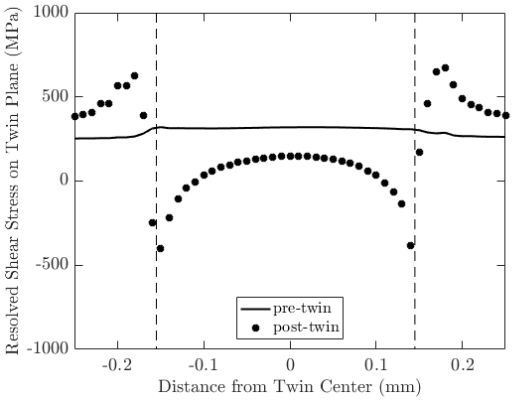

(c)

Figure 5.3: Resolved shear stress for the twin system along a line through the center of the twin in the twin direction, for simulations employing reorientation scheme 1 and performed with twin width (a) $w = 0.0025$mm, (b) $w = 0.005$mm, and (c) $w = 0.01$mm.

to grow, as there are regions in the twin with almost no drop in resolved shear stress. It is important to note that regardless of the driving mechanisms for twin nucleation or growth, results here concerning the stress states compare well to two dimensional studies (at least at the center of the twin).

The stresses in neighboring grains due to the twin motion, of course, will depend on the crystallographic orientations of the neighboring crystals. The maximum resolved shear stress on the twin systems in neighboring grains will almost certainly be dependent on the disparity between orientations of the crystal experiencing twinning and its neighbors. This is witnessed in crystals exhibiting crystallographic slip, where slip transmits across grain boundaries. In the case of slip, two grains must have similar orientations ("low angle boundaries") for slip to transmit across boundaries [37, 36].

5.2 Work Observations

Deformation twinning may be inspected in light of the amount of work required to impose the deformation associated with twinning over a discrete region. The total and plastic work rate is calculated at the end of every deformation step, and the work is integrated through time by means of a trapezoidal integration scheme (see: Chapter 3.2.3). The entire body is considered, rather than local subsets, so as to understand the energetic effect twin insertion has on the polycrystal as a whole. Of interest is the amount of work taken to activate a twin, and with this in mind, the change in work and plastic work is calculated between steps 5 and 6. Table 5.3 summarizes results from all simulations.

Inspecting trends with respect to changes in twin width reveals that the amount of work (both total and plastic) necessary to insert a twin at this point in deformation in-

	W (mJ)			W^P (mJ)		
w (mm)	**R.S. 1**	**R.S. 2**	**R.S. 3**	**R.S. 1**	**R.S. 2**	**R.S. 3**
0.0025	0.0178	0.0185	0.0152	0.0190	0.0209	0.0155
0.005	0.0380	0.0395	0.0329	0.0395	0.0432	0.0325
0.01	0.0689	0.0713	0.0607	0.0661	0.0720	0.0548

Table 5.3: Change in work and plastic work between deformation steps 5 and 6, calculated for simulations with a twinning event.

creases as twin width increases. This is expected, as larger volumes of material are displaced, and larger portions of the polycrystal are effected by the onset of twinning. Changes in reorientation scheme, too, have an effect on the calculated work. Reorientation schemes 1 and 2 have very similar total and plastic values, though reorientation scheme 2 is consistently marginally higher in both measures. Reorientation scheme 3, however, consistently measures lower than the other two reorientation schemes, especially in the plastic work measure.

Work is dominated by the work due to plasticity - which considers the plastic deformation rate tensor, and thus the deformation due to crystallographic slip. For each twin width and each reorientation scheme, the plastic work accounts for the majority of the work calculated over the polycrystal. This implies that during the twin event, the body is deforming largely by crystallographic slip so as to accommodate the deformation due to twinning. Note how in some instances (e.g., $w = 0.01$mm, reorientation scheme 2) the plastic work is greater than the total work, which indicates that the elastic work is negative over the time the twin is inserted. In this case, more work due to elastic unloading occurs during the onset of twinning than due to continued elastic loading over the entire polycrystal. In cases where the plastic work accounts for the majority of the total work, this indicates that the work due to elastic loading is nearly equal to the work due to elastic unloading over the entire domain, as they effectively cancel one another out.

Due to the nature of the integration technique, work calculations may be overestimated if abrupt elastic unloading occurs. A switch from a positive work rate to a negative work rate over a deformation step causes error in the integrated work. Numerical integration techniques will fail to capture the true negative work over a step, as the switch from a positive work rate to a negative work rate creates a saw-tooth curve, which is difficult to integrate using established techniques. This may be remedied by taking smaller time steps, thus finer resolving the work rate curve and allowing for more accurate integration. Consequently, the total work presented in Table 5.3 is likely an overestimate.

In addition to the simulations performed with a twinning event, simulations are conducted in which a twin is not inserted between steps 5 and 6. This allows for a comparison between simulations considering deformation through various modes. Though no twin is inserted, and thus all three simulations are seemingly identical, changes in the twin width lead to necessary changes in the finite element mesh. As such, slight variations in calculated values for work are expected in the three simulations performed with no twin insertion. These values are summarized in Table 5.4.

w **(mm)**	W **(mJ)**	W^P **(mJ)**
0.0025	0.0064	0.0000
0.005	0.0064	0.0000
0.01	0.0065	0.0000

Table 5.4: Change in work and plastic work between deformation steps 5 and 6, calculated for simulations without a twinning event.

The calculation of work serves to provide a possible path to determine when a twin event may occur. The framework allows for the possibility of two simulations to be performed concurrently - one in which the body deforms at certain points by means of deformation twinning, and one in which the body deforms entirely by crystallographic

slip. Integrated values for various metrics (e.g.: work, elastic relaxation, or others) may be compared between the two simulations *at each deformation step*, and the mode of deformation that is energetically favorable may be chosen as the path which the simulation continues on.

For the simulations performed, insertion of a twin of any size, and the employment of any reorientation scheme requires more work than in simulations without a twinning event. Indeed, the total work is an order of magnitude higher over the twin step. This may be expected, as the twin was inserted well before the onset of macroscopic plasticity. Localized plastic deformation has yet to become substantial at this point in loading, as the plastic work calculated for simulations without a twinning event was consistently negligible over that time step. A large deformation that relies on plasticity to accommodate the shape change may not compete in terms of an energetic measure to a body deforming nearly entirely elastically.

In these simulations, a twin is inserted in an arbitrary crystal, embedded in an arbitrary aggregate, at an arbitrary point in deformation. No care is taken to simulate a "real" event. As such, it cannot necessarily be expected that the work calculations would indicate a favorable event. This, however, provides a map for possible indication of twin nucleation.

Additionally, the change in temperature for a polycrystal at large is calculated per Equation 3.21. Table 5.5 summarizes the average change in temperature over the entire polycrystal due to a twinning event, as well as the maximum local change. As twin width increases, the average temperature increase in the polycrystal increases. Incremental reorientation of the crystal lattice, additionally, generally leads to a lower temperature increase than the other reorientation schemes.

	Global ΔT (C)			Local ΔT (C)		
w **(mm)**	**R.S. 1**	**R.S. 2**	**R.S. 3**	**R.S. 1**	**R.S. 2**	**R.S. 3**
0.0025	0.0074	0.0077	0.0064	43.7	42.6	47.0
0.005	0.0159	0.0165	0.0138	50.5	50.5	50.6
0.01	0.0288	0.0298	0.0254	36.4	33.7	37.2

Table 5.5: Average change in temperature due to twinning event for the entire polycrystal ("Global"), and the maximum local temperature change ("Local").

The maximum local increase in temperature is seen to be far greater than the average increase in temperature over the entire polycrystal. This is expected, as the twinning event - and the work associated with the event - is highly localized. Results indicate that the maximum temperature increase may be locally significant. This could necessitate the investigation of temperature dependent constitutive relations and evolution equations, though the magnitude of the maximum temperature increase is still relatively low, even in this worst-case scenario (assuming all work is translated to heat).

5.3 Slip Observations

While some studies postulate that the development of slip within twin regions after the twin event may be arrested [99], the current framework allows the body to continue deforming by means of slip everywhere in the domain. To investigate the consequences of this assumption, the effective plastic deformation rate is considered:

$$D^P_{eff} = \sqrt{\frac{2}{3}\left(\mathbf{D}^P : \mathbf{D}^P\right)} \tag{5.1}$$

Figures 5.4 and 5.5 detail the effective plastic deformation rate on the mesh at 2.0% macroscopic strain for simulations performed with various reorientation schemes, and for simulations performed with various twin widths, respectively.

As the plastic deformation rate is clearly non-zero in the twin region at a point later

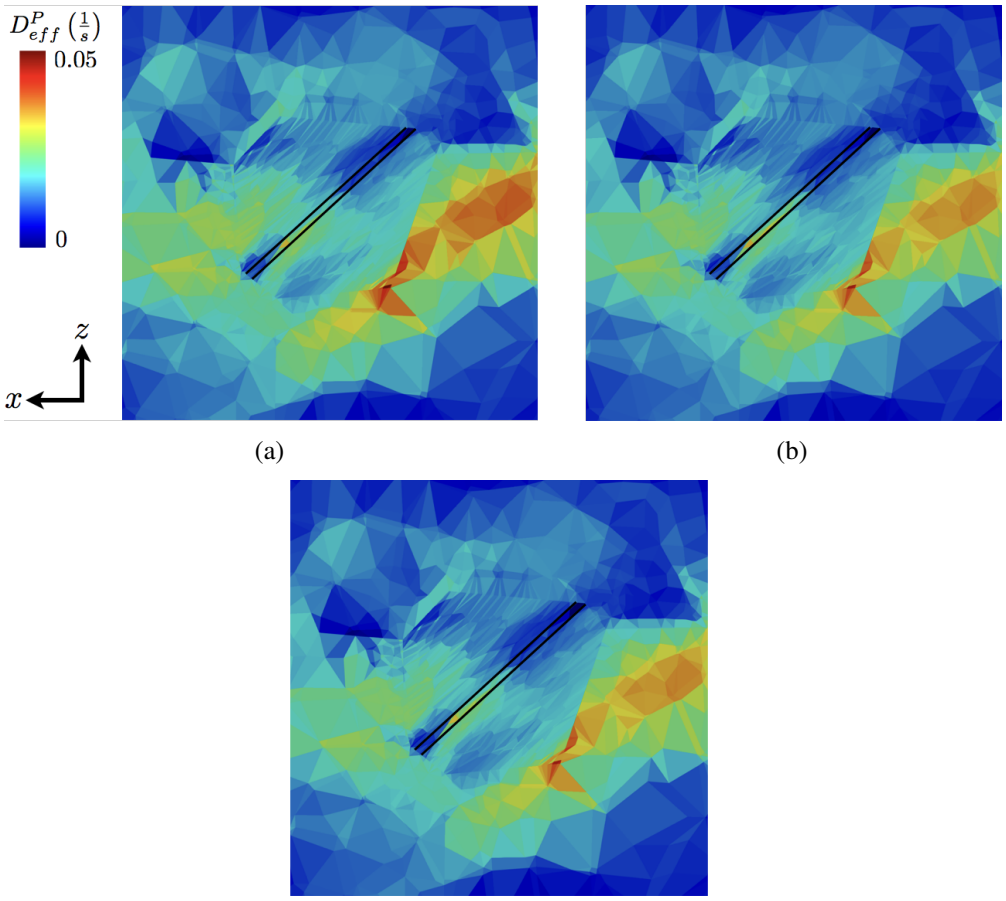

(a) (b)

(c)

Figure 5.4: Effective plastic deformation rate at 2.0% macroscopic strain, for simulations twin width w = 0.01mm employing (a) reorientation scheme 1, (b) reorientation scheme 2, and (c) reorientation scheme 3. Approximate twin boundaries are highlighted.

in deformation, twin region continues to deform by means of crystallographic slip. Table 5.6 details the volume fraction of the twin region considered to have active slip systems at 2.0% strain, calculated according to Equation C.11. As the model is currently formulated, there is no explicit term that would lead to the arrested development of slip within a twin region. Additionally, mechanical constraints due to the stress fields surrounding the twin do not lead to states in which the twin naturally experiences a prohibition of slip activity.

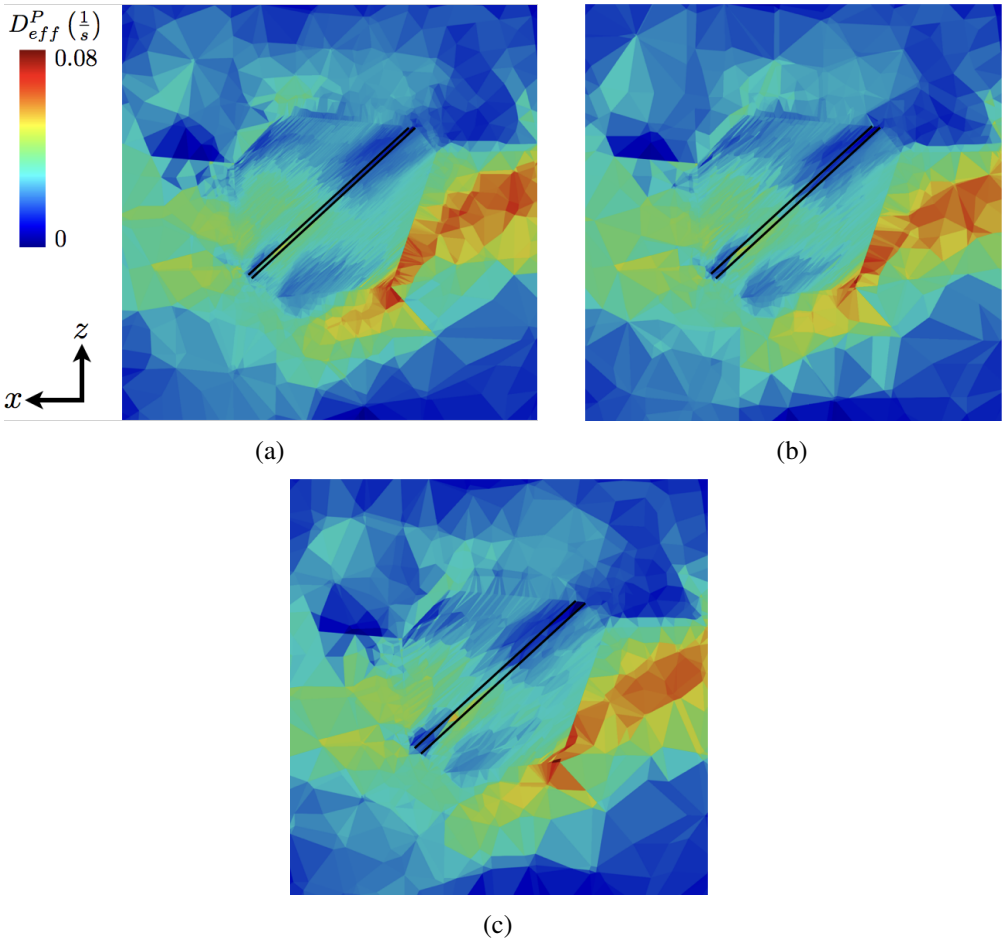

(a) (b)

(c)

Figure 5.5: Effective plastic deformation rate at 2.0% macroscopic strain for simulations employing reorientation scheme 1, with twin width (a) w = 0.0025mm, (b) w = 0.005mm, (c) w = 0.01mm. Approximate twin boundaries are highlighted.

	Volume Active (%)		
w **(mm)**	**R.S. 1**	**R.S. 2**	**R.S. 3**
0.0025	93.5	93.3	90.5
0.005	90.7	91.4	84.1
0.01	90.3	91.4	86.4

Table 5.6: Volume fraction of twin deforming by crystallographic slip at 2.0% macroscopic strain.

Figure 5.6 shows histograms detailing the volume fraction of the twin region deforming by each slip family for simulations performed with various twin widths.

Investigating the slip systems active at 2.0% macroscopic strain reveals that slip is generally dominated by the prismatic family of slip systems. This indicates that slip is occurring across the width of the twin. In some instances - particularly when reorientation scheme 3 is employed, volume fractions may sum to values greater than 100%. This indicates that the twin region is deforming by polyslip. Since the prismatic and pyramidal slip systems are active in large volume fractions of the twin region, this indicates the volume is deforming largely by polyslip comprised of these two systems.

Chapter 2.1.3 details theory which postulates the possible apparent hardening of slip systems within the twin region. Results here indicate no natural occurrence of arrested twin development. Indeed, slip is not restricted to be confined to the twin region, as shear on prismatic planes is predicted, which contradicts some theoretical thought. Insertion of multiple twins within a grain could have some effect on the development of plasticity between twin regions, though the study conducted in Appendix C indicates that this may not occur naturally do to mechanical constraints imposed on the system due to the spatial arrangement of grains and phases. However, should future experimental data definitively prove apparent hardening within twin regions or parent grains, the framework could be modified to force the hardening of slip systems to arrest the development of plasticity after a twin event.

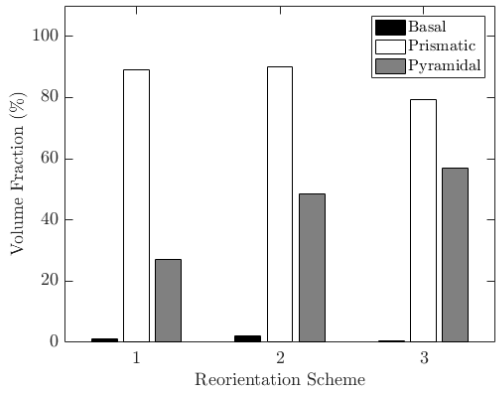

(a)

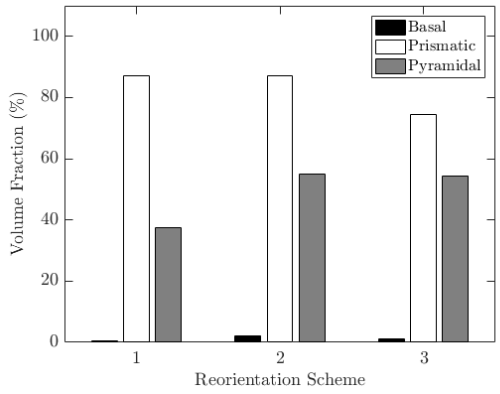

(b)

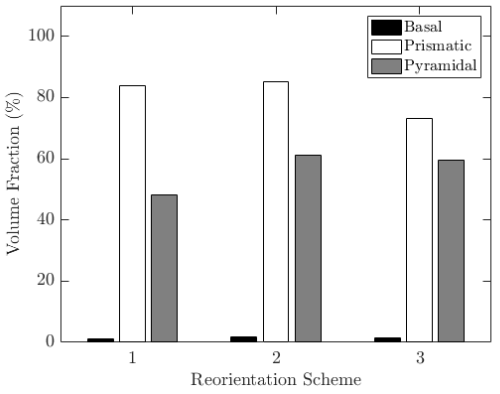

(c)

Figure 5.6: Slip system activity within the twin region at 2.0% macroscopic strain for simulations with (a) $w = 0.0025$mm, (b) $w = 0.005$mm, and (c) $w = 0.01$mm.

CHAPTER 6

SUMMARY

6.1 Conclusions

Experimental studies have observed deformation twins forming in many crystals exhibiting hexagonal symmetry. Modeling the plastic deformation response of materials, however, has largely focused on crystallographic slip. This dissertation provides a map to include deformation twinning in a crystal plasticity finite element framework. The existing framework - which largely considers only crystallographic slip - is extended to include deformation twinning in full field three dimensional simulations by means of pre-discretization of a representative sample into twin regions, and construction of an attendant finite element mesh. When deformation twinning is invoked, essential boundary conditions are placed on the nodes within a region such that the nodal points are mapped to their expected positions due to twinning, and the crystal lattice is reoriented. This deformation is forced to occur over a very brief duration such that the shear rate associated with a twinning event is greater than shear rates commonly witnessed due to crystallographic slip.

The framework distinguishes itself from previous attempts to model deformation twinning in that it upholds the basic characteristics of the deformation associated with twinning, rather than collapsing the physical differences between slip and twinning by modeling twinning as an auxiliary slip system. Specifically, existing twin modeling efforts largely ignore the discrete nature of twinning by homogenizing deformation responses due to both slip and twinning at discrete material points. Due to this homogenization, the relative rate differences between slip and twinning are largely obscured. Additionally, without considering discrete twin regions, existing frameworks fail to

introduce new grain boundaries that alter the spatial arrangement of grains, which is known to have large effects on the development of plasticity in aggregates. The proposed framework - by considering discrete twin regions and maintaining the relative difference in shear rates between slip and twinning - rectifies some of the assumptions made in previous modeling efforts. This allows for the study of the aggregates response to the deformation due to twinning, and for the precise study of local - and global - metrics due to a twinning event in a way that previous modeling efforts do not afford.

A simulation is performed on a single crystal sample, and results highlighted the proposed framework's ability to correctly map the motion due to twinning. Lattice reorientation is achieved through the use of three different orientation schemes, each of which prove effective in reorienting the lattice to its expected orientation. With confidence in the ability of the framework to correctly map the motion of the twin and reorient the crystal lattice, simulations are performed on polycrystalline aggregates. A twin is inserted into a crystal at the center of the aggregate at an arbitrary point in deformation. Three different twin widths are considered. Stress fields are inspected after the insertion of the twin. Results indicate that large stress concentrations form at the twin tips in neighboring grains and the volume of the regions effected by the twin motion in neighboring grains increases as the twin size increases, echoing some experimental results. The reorientation schemes considered have an effect on the stress states post-twinning. Reorienting the lattice entirely at the beginning or end of twinning generally leads to lower stresses in the twin region than if the lattice is incrementally reoriented. Additionally, the resolved shear stress drops within a twin region, and increases at the twin tips during a twin event, the degree to which is dependent on both the size of the twin region and the reorientation scheme employed. This overall result, however, confirms results from similar two dimensional studies.

The work necessary to insert a twin is calculated to understand the energy associated with a twinning event. As twin size increases, the work necessary to insert a twin increases. Both the total work and plastic work follow this trend. Additionally, how the crystal lattice is reoriented effects both measures of work. Specifically, inserting a twin while incrementally reorienting the crystal lattice requires less work than when the lattice is reoriented entirely at the beginning or end of a twin event. As twin size increases, the calculated plastic work increases such that it is greater than the total work, implying a negative elastic contribution. This indicates that some portion of the volume is elastically unloading, indicating that twinning causes some elastic relaxation within the polycrystal. This may be seen by comparing the von Mises stress fields before and after twinning, where a stress drop is witnessed in some portions of the polycrystal - specifically in portions of the grain which experiences twinning.

Additional simulations are performed without a twinning event to understand the work required to deform the material without a twin event. For this specific case, the insertion of a twin invariably led to higher values of work than when the polycrystal was allowed to deform without a twin event. This is to be expected, as little attention is paid to modeling a real twin event - all variables associated with this study were chosen arbitrarily. However, a possible path to understanding twin nucleation and growth is presented. This showcases the ability to run two concurrent simulations over each deformation step - one in which twinning is considered, and one in which twinning is ignored. Deformation may proceed choosing whichever deformation mode is energetically favorable, and different measures may be considered, such as the total work or the elastic relaxation.

The change in temperature associated with the event is calculated, assuming all of the work associated with the twin event is converted to heat. Global results indicate that

the average temperature change in the polycrystal is negligible. However, the maximum local temperature change reveals sharp increases in temperature in the vicinity of the twin tip. A temperature increase can lead to changes in the elastic response as well as the elastic response, necessitating changes in the elastic constants, the slip strengths, the rate dependence, and the hardening parameters. Results suggest that coupling material properties with temperature should be investigated, as it could alter the deformation field, at least locally.

Finally, the development of slip is monitored after the twin event. As the polycrystal continues to deform, slip is observed to occur in large portions of the twin region. There is no mechanism inherent in the model to suppress slip in twin regions, and mechanical constraints on the twin region due to local deformation fields does not naturally suppress slip. Additionally, slip is witnessed to occur primarily on the prismatic plane, indicating the development of slip across the width of the twin.

Robust experimental data is necessary to best inform the future development of this model. Specifically, understanding the deformation field prior to and after a twinning event is necessary to tune the presented framework, understand the work associated with a twin event, and to understand the development of plasticity due to crystallographic slip after a twin event. As described in Chapter 2.1.3, high energy X-ray diffraction methods hold the greatest promise for providing the necessary data sets. Recent experimental studies have demonstrated the ability to determine grain average stress states, as well as characterize the formation of deformation twins. Further studies have shown that simulations provide a way of understanding the complex heterogeneous deformation that develops at the sub-grain level. By instantiating crystals to contain observed twins, and inserting them at the proper spatial location and at the correct point in deformation, a statistical understanding of the stress states prior to and after twinning may be deduced.

Machine learning techniques may offer insight into these complex data sets.

6.2 Future Directions

Parametric Study

Experienced gained in the study outlined in Appendix C showed how a rigorous and methodical parametric study may be performed. Such a study should be performed on this deformation twinning framework to gauge the response of aggregates to various changes. Possible parameters to be studied could include:

- Twin width
- Twin location
- Orientation of crystal
- Point in deformation at which twin is inserted

Effects to be gauged should include:

- Effects on macroscopic total work and plastic work
- Effects on macroscopic yield strength and ductility
- Effects on local quantities, such as slip activity

Extension to Various Crystal Types

The framework may be generalized to include twinning for any crystal symmetry, primarily crystals exhibiting cubic symmetry. As it stands, the only change necessary to the

framework is generalizing the calculation of the reciprocal lattice vector for any crystal symmetry (Chapter 3.1). This would make the framework more versatile, and open it to a new class of materials that it can model.

Transformation Induced Plasticity

The presented framework is uniquely positioned to handle the problem of both deformation twinning and transformation induced plasticity. Deformation twinning could (in some ways) be considered a sub-problem of transformation induced plasticity. While deformation twinning is characterized by the uniform shear of a discrete region coupled with a reorientation of the crystal lattice within said region, transformation induced plasticity is different only in that it considers, additionally, a change in crystallographic phase. Practically, this would require few changes on top of what is already included in the framework, as elements could essentially be assigned a new phase designation upon transformation (with a few other minor steps). This is, perhaps, the most exciting change to be implemented into the code.

APPENDIX A

FINITE ELEMENT IMPLEMENTATION

Below is a detailed description of the finite element implementation of the crystal plasticity finite element framework utilized in this study.

For ease of implementation of in a finite element framework, quantities described in Chapter 2.2 must be cast as vectors and matrices. First, consider the following transformations, taking second order tensors to column vectors:

$$\begin{aligned} \boldsymbol{\tau} \rightarrow \{\tau\} &= \left\{\tau_{11} \quad \tau_{22} \quad \tau_{33} \quad \sqrt{2}\tau_{23} \quad \sqrt{2}\tau_{13} \quad \sqrt{2}\tau_{12}\right\}^T \\ \boldsymbol{\tau}' \rightarrow \{\tau'\} &= \left\{\tfrac{1}{\sqrt{2}}\left(\tau'_{11} - \tau'_{22}\right) \quad \sqrt{\tfrac{3}{2}}\tau'_{33} \quad \sqrt{2}\tau'_{23} \quad \sqrt{2}\tau'_{13} \quad \sqrt{2}\tau'_{12}\right\}^T \end{aligned} \tag{A.1}$$

The top applies to all full tensors, while the bottom transformation applies specifically to deviatoric tensors. In both cases, coefficients on individual terms arise to preserve the inner product (i.e., such that $\boldsymbol{\tau} \cdot \boldsymbol{\tau} = \{\tau\}^T \cdot \{\tau\}$).

Similarly, the fourth order stiffness tensor (Equation 2.10) is reduced to a volumetric component, κ, and a diagonalized deviatoric component $[C']$, such that (for hexagonal crystals) $\kappa = 3\left(C_{11} + C_{12} + C_{13}\right)$, and:

$$[C'] = \begin{bmatrix} C_{11} - C_{12} & & & & & \\ & 3\left(C_{33} - C_{13}\right) & & & & \\ & & C_{44} & & & \\ & & & C_{44} & & \\ & & & & C_{11} - C_{12} & \end{bmatrix} \tag{A.2}$$

Thus, the volumetric and deviatoric Kirchhoff stresses are calculated as:

$$\begin{aligned} \operatorname{tr}\left(\{\tau\}\right) &= \frac{\kappa}{3}\operatorname{tr}\left(\{E^e\}\right) \\ \{\tau'\} &= [C']\{E^{e\prime}\} \end{aligned} \tag{A.3}$$

Turning now to time discretization, the rate change of the elastic strain ($\{\dot{\mathbf{E}}^e\}$) may be approximated from the strains at the beginning ($\{e_0^e\}$) and end ($\{e^e\}$) of a time step:

$$\{\dot{E}^e\} = \frac{1}{\Delta t}\left(\{E^e\} - \{E_0^e\}\right) \tag{A.4}$$

Substituting Equation A.4 into the expression of the deviatoric deformation rate in Equation 2.8 gives:

$$\{D'\} = \frac{1}{\Delta t}\{E^{e\prime}\} + \{\hat{D}^{P\prime}\} + \left[\hat{W}^P\right]\{E^{e\prime}\} - \frac{1}{\Delta t}\{E_0^{e\prime}\} \tag{A.5}$$

where

$$\{\hat{D}^{P\prime}\} = [M]\{\tau'\} = \sum_k \left(\frac{\dot{\gamma^k}}{\tau^k}\right)\{P^k\}\{P^k\}^T\{\tau'\} \tag{A.6}$$

where $\dot{\gamma^k}$ is found through the power law expression of Equation 2.13, τ^k is the resolved shear stress, and $\{P^k\}$ the vector form of the symmetric portion of the Schmid tensor for the k^{th} slip system. This, together with the knowledge that $\{\tau'\} = [C']\{E^{e\prime}\}$,

$$\begin{gathered}\{\sigma'\} = [S]\left(\{D'\} - \{H'\}\right) \\ \text{where } [S]^{-1} = \frac{\beta}{\Delta t}[C']^{-1} - \beta[M] \\ \text{and } \{H'\} = \left[\hat{W}^P\right]\{E^{e\prime}\} - \frac{1}{\Delta t}\{E_0^{e\prime}\}\end{gathered} \tag{A.7}$$

Here, the deviatoric Cauchy stress is related to the total deformation rate, as well as the spin and elastic strain at the beginning of the time step, $\{H'\}$, through the tensor $[S]$, which relies on β - the determinant of the elastic stretch, $\mathbf{F}^e$.

Equilibrium is enforced by ensuring a weighted residual is iteratively driven to zero:

$$R = \int_{\mathcal{B}} \psi \cdot (\nabla \cdot \boldsymbol{\sigma} + \mathbf{b})\, \mathrm{d}\mathcal{B} = 0 \tag{A.8}$$

where $\nabla \cdot \boldsymbol{\sigma}$ is the divergence of the Cauchy stress, and $\mathbf{b}$ are the body forces. This allows for the formation of the standard weak form:

$$R = \int_{\mathcal{B}} \mathrm{tr}\left(\boldsymbol{\sigma}'\nabla\psi\right)\mathrm{d}\mathcal{B} + \int_{\mathcal{B}} \pi\nabla\cdot\psi\mathrm{d}\mathcal{B} + \int_{\partial\mathcal{B}} \mathbf{t}\cdot\psi\mathrm{d}\Gamma + \int_{\mathcal{B}} \mathbf{b}\cdot\psi\mathrm{d}\mathcal{B} \tag{A.9}$$

where π is the hydrostatic stress, $\mathbf{t}$ is the applied traction, and Γ the portion of the domain with applied traction.

Ignoring body forces and applied tractions (only velocity essential boundary conditions are considered currently), and casting in a matrix form, the residual for each element of a finite element mesh takes the form:

$$\{R^{el}\} = \left[\left[K^{el}_{dev}\right] + \left[K^{el}_{vol}\right]\right]\{V\} - \{f^{el}_{dev}\} - \{f^{el}_{vol}\} \tag{A.10}$$

where (each integral below is evaluated by means of Gauss quadrature):

$$\begin{aligned}
\left[K^{el}_{dev}\right] &= \int_{\mathcal{B}} [B]^T\,[X]^T\,[S\,]\,[X]\,[B]\,\mathrm{d}\mathcal{B} \\
\left[K^{el}_{vol}\right] &= \int_{\mathcal{B}} \frac{\beta}{\kappa\Delta t}\,[B]^T\,[X]^T\,\{\delta\}\{\delta\}^T\,[X]\,[B]\,\mathrm{d}\mathcal{B} \\
\{f^{el}_{dev}\} &= \int_{\mathcal{B}} [B]^T\,[X]^T\,[S\,]\,\{H\}\mathrm{d}\mathcal{B} \\
\{f^{el}_{vol}\} &= \int_{\mathcal{B}} [B]^T\,[X]^T\,\frac{\beta}{\kappa\Delta t}\{\delta\}^T\{E^e_0\}\mathrm{d}\mathcal{B}
\end{aligned} \tag{A.11}$$

where $[B]$ are the derivatives of the shape functions of the elements, $[X]$ is an array of coefficients to ensure proper inner products, $\{\delta\}$ is a matrix trace operator, $\left[K^{el}_{dev}\right]$ is the deviatoric stiffness matrix, $\left[K^{el}_{vol}\right]$ is the volumetric stiffness matrix, and $\{f^{el}_{dev}\}/\{f^{el}_{vol}\}$ are the matrices accounting for the initial elastic strain at the beginning of a step, and the spin at the beginning of a step, respectively.

Assembling for the entire mesh and enforcing that the residual must vanish for every element yields a global residual gives:

$$\{R\} = [[K_{dev}] + [K_{vol}]]\,\{V\} - \{F_{dev}\} - \{F_{vol}\} \tag{A.12}$$

As both the deviatoric and volumetric stiffnesses, K, are dependent on the velocity field - and thus Equation A.12 is non-linear - the goal is to iteratively solve for the

velocity field at step $n + 1$ by correcting the velocity field from step n:

$$\begin{gathered} \{V\}^{n+1} = \{V\}^{n} + \{\Delta V\}^{n+1} \\ \text{where } \left[[K_{dev}] + [K_{vol}]\right] \{\Delta V\}^{n+1} = -\{R\}^{n} \end{gathered} \tag{A.13}$$

Here, $[K_{dev}]$ is either the secant stiffness matrix or tangent stiffness matrix, depending on whether the solver is currently using Picard's method or the Newton-Raphson method, respectively. For a given time step, the solver generally uses Picard's method for the first few iterations, followed by Newton-Raphson to solve for final convergence. Note, the essential velocity boundary conditions are held fixed for a given time step in the above equation. That is, ΔV is 0 for nodes which have essential velocity boundary conditions.

APPENDIX B

ON SLIP INITIATION IN EQUIAXED α/β TI-6AL-4V

The following appears in *Acta Materialia* [60].

Abstract

A computational study of 3D virtual instantiations of microtextured Ti-6Al-4V with varying initial slip system strengths is presented. Electron backscatter diffraction (EBSD) scans of a rolled and heat-treated mill annealed plate were used in order to determine the approximate geometric morphology of both the grain structure and the microtextured regions. Data from the EBSD experiments were used to calculate representative orientation distribution functions (ODFs) and grain size distributions for the α (HCP) crystallographic phase. Laguerre tessellations were employed to create idealized geometric representations of the microstructure and microtextured regions, while orientations were sampled from the experimentally derived ODFs. A highly parallelized crystal plasticity finite element framework was used to model the deformation response of single phase polycrystals under uniaxial tension, with attention paid to the intragrain slip system activity. Simulations were conducted with changes in the orientations within microtextured regions, as well as with various sets of initial slip system strengths to reflect differences in reported values in literature. Results were compared to a strength-to-stiffness parameter designed to predict succession of yield as a function of orientation. Presented are slip activity trends as a function of microstructure and initial slip system strengths, as well as results concerning the development of long-range localization of plasticity as a function of the microstructure. Predictions are compared to slip system activity measured by digital image correlation.

B.1 Introduction

Ti-6Al-4V is the most widely produced titanium alloy, used in a wide array of industries and applications due to good resistance to corrosion, high strength, and low density [75]. Lending complexity to understanding the deformation response is the presence of a hexagonal crystallographic phase which exhibits elastic anisotropy and strong plastic anisotropy [63, 118]. Furthermore, due to the thermomechanical processes used during manufacture, a wide variety of microstructures are attainable, and thus a wide range of deformation responses are available from this single alloy. Determining how the microstructure influences the deformation response is crucial in understanding such a ubiquitous alloy.

Of the most common microstructures, those produced by the mill annealed processing path exhibit near equiaxed grains of hexagonal crystallographic phase - in contrast to the complex geometric structures that may form in other variations (e.g. the β annealed and bi-modal microstructures) [35, 107]. Additionally, the microstructure contains spatial regions comprised of contiguous grains with crystallographic orientations of a single crystallographic fiber - microtextured regions - that arise from the unique processing route of the mill annealed microstructure. The texture of these regions may contribute to only a portion of the overall texture of the material, and have been experimentally observed in a number of studies [89, 44, 114, 39]. Due to the microstructural morphology and crystallographic texture, the equiaxed mill annealed microstructure exhibits a different deformation response than other microstructural variations, namely exhibiting both a higher yield strength and ductility, as well as less variation in both measures.

The plastic behavior of many hexagonal crystals is debated in literature. In order to accommodate generalized plastic deformation [51], multiple families of slip systems

- namely the basal, prismatic, and pyramidal families - are required. While the plastic behavior of hexagonal crystals is widely accepted to be anisotropic, the degree of anisotropy is contested [56, 111, 18, 49, 128, 136]. Specifically, debate centers on the relative strength of the pyramidal family, as well as whether the basal or prismatic family is the weakest slip family. The mechanical response and development of plasticity within an aggregate comprised of hexagonal crystals will be sensitive to the relative initial slip system strengths.

Considering the mechanical constraints that exist due to compatibility and equilibrium between grains - as well as between microtextured regions - is crucial in determining the influence of microtextured regions and initial slip system strengths on the deformation response of the material. Computational simulations provide a window into the development of plasticity at the crystal scale [8, 78, 77], which can lend insight into grain-to-grain and region-to-region interactions. This includes other recent work concerning slip initiation in microtextured materials through the lens of simulated deformation data [50]. Developments in parallel computing as well as the creation of large scale representative geometries and attendant finite element meshes [93] allow for the simulation of large, highly refined polycrystals, and thus the interrogation of both the behavior of the aggregate and behavior within grains.

Prediction and explanation of the succession of crystal yield, as evidenced by the initiation of slip, is achieved through the use of a directional strength-to-stiffness metric [129]. Considering not only the slip system strengths of an oriented crystal, but also its directional stiffness, a directional strength-to-stiffness metric has been used to predict the succession of yield by comparing the relative strains at which different crystals may reach a critical resolved shear stress in order for slip to activate. Previous work [129] has focused on understanding the influence of elastic anisotropy on the strength-to-stiffness

ratio in FCC crystals. For the case of HCP crystals, the directional strength-to-stiffness metric becomes more complicated with the presence of plastic anisotropy. First order assumptions regarding the crystal stress state allow for computationally inexpensive baseline predictions of the succession of yield for individual crystals during the onset of plasticity. When used in highly textured materials that exhibit plastic anisotropy, a directional strength-to-stiffness metric can also explain the succession of separate families of slip systems with disparate initial strengths.

In this study, electron backscatter diffraction data in large 2D scans and in 3D datasets are used to inform the geometric representation of polycrystals through the use of Laguerre tessellations [61, 94]. These data are also used to functionally represent orientation distributions. Tessellations and orientation distributions are used together to create instantiations for use in deformation simulations. A suite of simulations is conducted to probe both the influence of microtextured regions on the development of plasticity in the polycrystal, as well as the sensitivity of slip activation to initial slip system strengths. Results are compared to previous experimental observations through the lens of a strength-to-stiffness metric.

B.2 Background

B.2.1 Material Background

Ti-6Al-4V alloys subject to deformation processing and subsequent annealing in the α/β phase field develop a spectrum of relatively fine-scale α/β microstructures. The material used in this study (Figure B.1) was homogenized in the β phase field, cooled, and then rolled into plate at a temperature just below the α/β transus. Subsequently, the plate

was heat treated at 926°C for 4 hours and cooled to room temperate at 0.3°C/minute to homogenize residual strain present from the hot working steps. Analysis of the top of the rolled plate details a composition of 6.28 wt% aluminum, 4.09 wt% vanadium, 0.18 wt% oxygen, 0.19 wt% combination iron, carbon, nitrogen, and yttrium, and balance titanium.

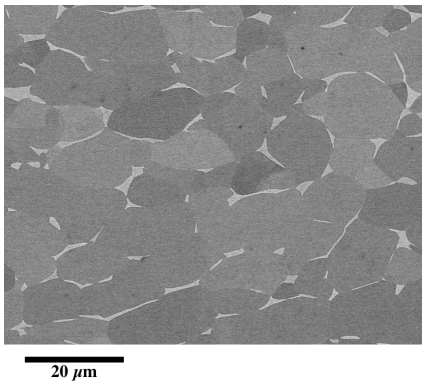

Figure B.1: Backscattered electron (BSE) image of the investigated Ti-6Al-4V alloy showing the α grains (dark grey) and the β grains (light contrast). The material is primarily composed of equiaxed α grains surrounded or partially surrounded by β phase.

Dominant in terms of volume fraction, the α phase - which exhibits HCP crystal symmetry - represents approximately 92% of the material volume. The geometry of the microstructure of Ti-6Al-4V is very sensitive to the thermomechanical processes used during production. Microstructures (e.g. β annealed or bimodal) comprised of primary grains with complex sub-grain structures are attainable through the use of hot rolling or long recrystallization steps, and present many challenges with respect to understanding their deformation responses. The equiaxed mill annealed microstructure represents a geometrically simple microstructural variation available for Ti-6Al-4V. Electron backscatter diffraction (EBSD) scans elucidate the geometric morphology of the α grains in the microstructure (Figure B.2(a)), which shows that the mill annealed microstructure is comprised of α phase grains of both similar size and shape.

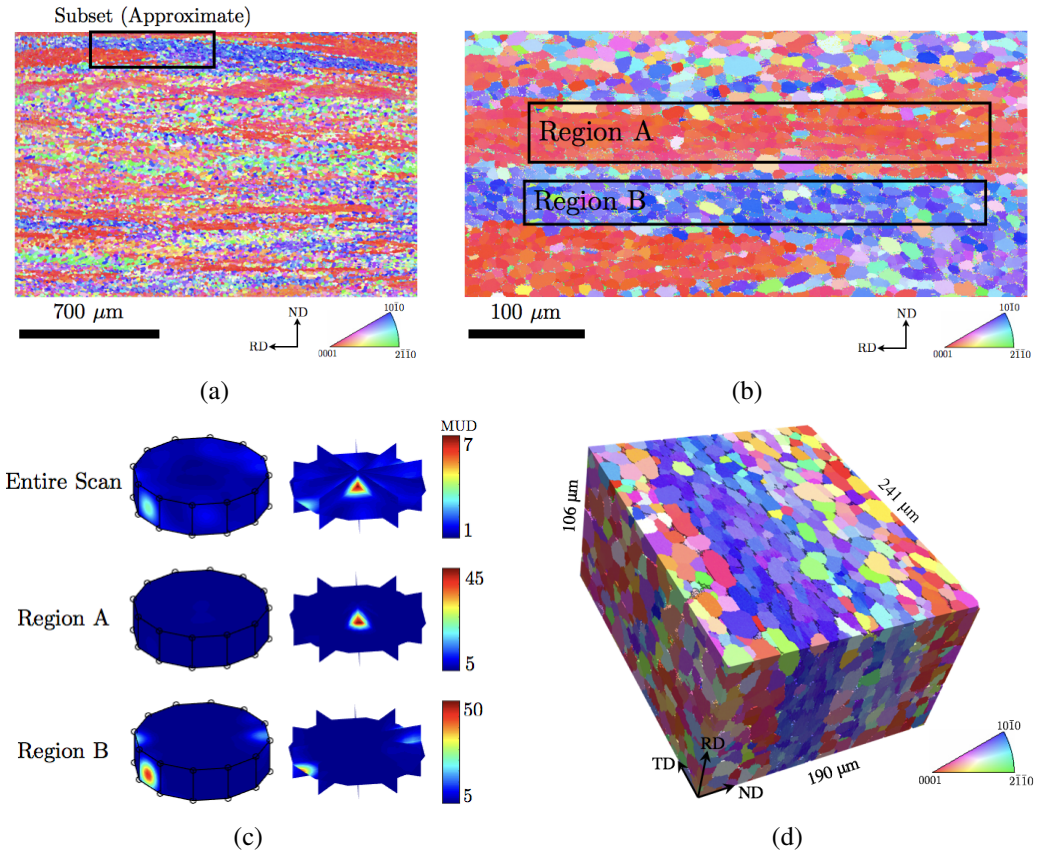

Figure B.2: (a) EBSD scan of an equiaxed mill annealed Ti-6Al-4V plate. (b) Subset of EBSD scan with microtextured regions of interest outlined. (c) Orientation distribution functions calculated from entire EBSD scan as well as selected regions, and plotted in the hexagonal symmetry fundamental region of Rodrigues' space. (d) Three dimensional morphology of the equiaxed mill annealed microstructure elucidated by TriBeam tomography and 3D EBSD reconstruction. All EBSD images depict only the α crystallographic phase.

Additionally, crystallographic orientations of the grains are gathered from EBSD scans. Figure B.2(b) details a subset of the EBSD scan in Figure B.2(a), and exhibits areas of contiguous grains with similar crystallographic orientations (labeled "Region A" and "Region B") - or microtextured regions. The two outlined regions show two different microtextured regions. Similarly oriented microtextured regions appear multiple times through EBSD surface scans covering larger areas B.2(a). The microtextured regions outlined in Figure B.2(b) were identified visually. Microtextured regions result

due to the persistence of α phase transformation structures (that arise from high temperature β phase structures) through thermomechanical processing [9, 75].

By considering the orientations measured in the entire scan, as well as only those within the selected regions, functional representations of the microtextured regions may be constructed [70]. Figure B.2(c) shows the deduced orientation distribution functions (ODFs) for the entire scan, as well as each of the identified microtextured regions plotted in the hexagonal symmetry fundamental region of Rodrigues' space [43, 70]. Note that both of the ODFs for the selected regions possess only a single peak - or a distribution centered on only a single crystallographic orientation. The ODFs for the selected regions represent only portions of the entire sample's texture - functionally illustrating the microtextured regions present in the sample. All calculations and plotting in Rodrigues' orientation space were performed using the ODFPF software package developed by the Deformation Processes Lab at Cornell University [31].

Three-dimensional characterization was performed by TriBeam, an in-situ FIB-SEM microscope femtosecond laser based mesoscale tomography technique [40]. The TriBeam tomography experiment performed on the Ti-6Al-4V alloy in this article involved femtosecond laser sectioning, a fast glancing angle 30kV, 20nA FIB cleaning step, and collection of both secondary electron images and electron backscatter diffraction (EBSD) maps. Tomographic sectioning was performed with an in-plane EBSD imaging resolution of 0.6 μm and a sectioning resolution of 1 μm. Imaging was performed using a 30kV electron beam and a 4x4 binning mode on the EBSD detector. The 3D reconstruction was performed using DREAM.3D [46]. Briefly, the reconstruction process required a registration (slice alignment step) and a 5° segmentation tolerance to define the grains boundaries.

The 3D characterization (Figure B.2(d)) shows that the microtextured regions run

lengthwise not only in the rolling direction (as shown in Figure B.2(b)) but also in the transverse direction. In other words, the microtextured regions are planar regions with normals in the same direction as the sample ND.

Surface strain measurements were made using a SEM based digital image correlation (SEM DIC) technique in a previous study [39] to determine the relative slip system activity and the extent and location of strain localization before the onset of plasticity. The SEM DIC technique was developed [115] to measure elastic strains as small as 0.15% at the sub-micron scale, in other words, at resolutions that can resolve the location of strain localization inside of grains. In a previous article [39], the sequence of slip activation was shown in an identical microtextured Ti-6Al-4V alloy as used in the present study. Loading was performed on a sample at strain rates of 10^{-3} s^{-1} to 10^{-4} s^{-1} while DIC measurements were taken at discrete macroscopic strain states before the onset of macroscopic plasticity. Experimentally, strain localization was observed substantially earlier than macroscopic yielding (in the macroscopic elastic loading regime) in preferentially orientation grain and microtextured regions. Furthermore, the localization of plastic straining was observed to occur across entire microtextured regions - notably with bands of plastic deformation traversing grains and phases (Figure B.3). Slip activity characterized as a function of the applied macroscopic strain was detected by SEM DIC, and has been directly compared to the simulations performed in this article.

B.2.2 Simulation Methods

The model employed in this study is an elastic-viscoplastic model embedded in a highly parallelized finite element framework. This method is capable of modeling large inelastic, quasi-static deformations of a polycrystal discretized into a finite element mesh.

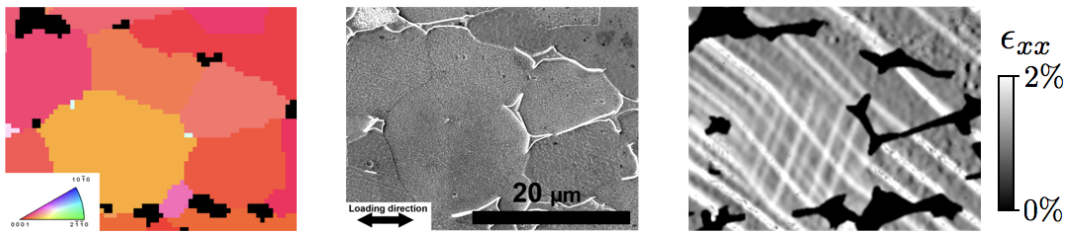

(a) (b) (c)

Figure B.3: Results from (a) EBSD, and (b) SEM DIC experiments detailing grain and phase structure. (c) Strain distribution at 1.00% macroscopic strain, which details the localization of plastic strain (white bands) traversing α phase grains - including those separated by small regions of β phase (black regions).

The deformation of the material is described using a set of constitutive equations, and we consider both an elastic response and inelastic response of a single crystal. Anisotropy is included in the elastic response, as well as the inelastic response, which considers only rate-dependent crystallographic slip restricted to dominant slip systems. Although deformation twinning is commonly seen in commercially pure titanium and other titanium alloys, it is not observed in Ti-6Al-4V due to its high aluminum content [75] and consequently was not modeled. Deformation is considered to be ductile and isothermal - no heat transfer or fracture models are included. Simulations are performed using the FEpX software package [32]. Here, a simplified summary of the model is described. A more complete description of the kinematics and configuration may be found in the FEpX theory and methods manual [32].

The equations for the elastic and plastic responses are written in a configuration reached by elastically unloading, without rotation, from the current, or spatial, configuration by the inverse of the elastic stretch, $\mathbf{v}^e$. The elastic portion of deformation is governed by Hooke's law,

$$\boldsymbol{\tau} = \mathbf{C}(\mathbf{r})\mathbf{e}^e \tag{B.1}$$

where the Kirchhoff stress, $\boldsymbol{\tau}$, is related to the elastic strain, $\mathbf{e}^e$. The Kirchhoff stress is

related to the Cauchy stress, $\boldsymbol{\sigma}$, by $\boldsymbol{\tau} = \det(\mathbf{v}^e)\boldsymbol{\sigma}$; the elastic strain is computed from the elastic stretch as $\mathbf{e}^e = \mathbf{v}^e - \mathbf{I}$, assuming small elastic strains [17, 86]. The stiffness tensor, $\mathbf{C}$, is dependent on the symmetry of the crystal, and is reduced to reflect said symmetry [84]. Additionally, the stiffness tensor is a function of the orientation of the crystal, represented here using the Rodrigues' vector, $\mathbf{r}$ [43].

The plastic portion of deformation is governed by a rate-dependent restricted slip model. The plastic deformation rate, $\mathbf{D}^P$ (defined again in unloaded configuration), is a linear combination of the simple shearing modes defined by the symmetric portion of the Schmid tensors,

$$\mathbf{D}^P = \sum_k \dot{\gamma}^k \mathbf{P}^k \tag{B.2}$$

$$\mathbf{P}^k = \mathrm{sym}\left(\mathbf{s}^k \otimes \mathbf{m}^k\right) \tag{B.3}$$

where $\dot{\gamma}$ is the shearing rate. For each slip system, k, the Schmid tensor is defined as the dyadic product between a slip plane normal vector, $\mathbf{m}^k$, and a slip direction vector, $\mathbf{s}^k$.

Slip systems considered in this study are shown in Table B.1. The α phase utilizes three slip families to represent those which have been experimentally observed to be active during the onset of plasticity [39].

Slip System Name	Number of Systems	m	s
Basal (b)	3	$\{0\,0\,0\,1\}$	$\langle 1\,1\,\bar{2}\,0\rangle$
Prismatic (p)	3	$\{0\,0\,\bar{1}\,0\}$	$\langle 1\,1\,\bar{2}\,0\rangle$
Pyramidal (π)	12	$\{0\,0\,\bar{1}\,1\}$	$\langle 1\,1\,\bar{2}\,3\rangle$

Table B.1: Slip systems used for the α phase of Ti-6Al-4V.

The kinetics of slip are defined using a power law relationship between the shearing rate of a given slip system and the resolved shear stress, τ^k, on that system:

$$\begin{aligned} \dot{\gamma}^k &= \dot{\gamma}_0 \left(\frac{|\tau^k|}{g^k}\right)^{\frac{1}{m}} \mathrm{sgn}(\tau^k) \\ \text{where } \tau^k &= \mathrm{tr}(\mathbf{P}^k \boldsymbol{\tau}') \end{aligned} \tag{B.4}$$

where $\boldsymbol{\tau}'$ is the deviatoric portion of $\boldsymbol{\tau}$. The resolved shear stress on a slip system is scaled by the slip system strength, g^k. The fixed-state strain rate sensitivity is controlled by m, and $\dot{\gamma}_0^k$ is the fixed-state strain rate scaling coefficient. For a given element, g^k evolves at the same rate for all slip systems within a family.

Similarly, for a given element, each slip system within a family will evolve at the same rate. Evolution of a slip system's strength is modeled using a linear Voce hardening assumption [65], while the saturation strength is a function of the sum of the slip system shear rates for a given element:

$$\begin{aligned} \dot{g}^k &= \dot{\gamma} h_0 \left(\frac{g_s^k(\dot{\gamma}) - g^k}{g_s^k(\dot{\gamma}) - g_0^k} \right) \\ \text{where } g_s^k(\dot{\gamma}) &= g_{s0}^k \left(\frac{\dot{\gamma}}{\dot{\gamma}_{s0}} \right)^{m'} \\ \text{and } \dot{\gamma} &= \sum_k |\dot{\gamma}^k| \end{aligned} \tag{B.5}$$

The initial slip system strength and saturation strength are defined by g_0^k and g_s^k, respectively, and h_0 is the strength hardening rate coefficient. The saturation strength is a function of the sum of the slip system shear rates for a given element, and is controlled by the initial saturation strength, g_{s0}^k, the saturation strength strain rate scaling coefficient, $\dot{\gamma}_{s0}$, and the saturation strength rate scaling exponent, m'. For a given element, the saturation strengths of all slip systems within a family will evolve at the same rate.

Model parameters were gathered from the analysis of tensile tests on equiaxed Ti-6Al-4V and from literature on Ti-Al alloys [126, 33, 56, 111, 18, 49, 128, 136]. Single crystal elastic constants are outlined in Table B.2, and were optimized in an associated optimization study on the same material studied here [126]. Values used for the variations on the initial slip system strengths for this study are outlined in Table B.3. The primary set of initial slip system strengths (Strength Set 1) were also determined in a related study on the same material [33]. The methodology employed in these studies

consisted of a combination of high-energy x-ray diffraction experiments with *in situ* loading of equiaxed Ti-6Al-4V and coordinated finite element simulations of virtual polycrystals. Elastic moduli and slip system strengths were determined by matching the evolution of the dominant modes of harmonic expansions of lattice strain distributions within the elastic domain for the elastic moduli and through the elastic-plastic transition for the slip system strengths. As indicated in Table B.3, Strength Set 1 prismatic strength is slightly higher than the basal strength and the pyramidal strength is moderately higher than the basal strength.

C_{11} **(GPa)**	C_{12} **(GPa)**	C_{13} **(GPa)**	C_{44} **(GPa)**
169.7	88.7	61.7	42.5

Table B.2: Single crystal elastic constants for the α phase of Ti-6Al-4V.

Strength Set	$g_{0,b}$ **(MPa)**	$g_{0,p}$ **(MPa)**	$g_{0,\pi}$ **(MPa)**	$\frac{g_{0,p}}{g_{0,b}} : \frac{g_{0,\pi}}{g_{0,b}}$
1	390	468	663	1.2 : 1.7
2	390	390	1170	1.0 : 3.0
3	390	351	663	0.9 : 1.7

Table B.3: Variations of initial slip system strengths used for simulating the α phase of Ti-6Al-4V, including relative ratios normalized by each set's basal strength.

The relative values of slip system strengths reported in the literature for the hexagonal phase of Ti-Al alloys spans a considerable range, as summarized in Table B.4 [56, 111, 18, 49, 128, 136]. Most often the pyramidal systems are moderately to greatly higher in strength than the basal systems. In contrast, the prismatic systems range from slightly weaker to slighter stronger than the basal systems. To explore these trends in the simulations performed here, Strength Sets 2 and 3 were chosen to complement the ratios existing in Strength Set 1. Strength Set 2 has equal basal and prismatic strengths, and a substantially higher pyramidal strength. Strength Set 3 has a relatively weak prismatic strength in comparison to the basal strength and a moderately higher pyramidal strength. With these definitions for the three strength sets we are able to explore three markedly

different distributions of strength-to-stiffness ratios, as discussed in the following section.

$g_{0,b}$ **(MPa)**	$g_{0,p}$ **(MPa)**	$g_{0,\pi}$ **(MPa)**	$\frac{g_{0,p}}{g_{0,b}} : \frac{g_{0,\pi}}{g_{0,b}}$	**Alloy and Reference**
444	392	631	0.9 : 1.4	Ti-6Al-4V [56]
353	397	503	1.1 : 1.4	Ti-6Al-4V [111]
420	370	590	0.9 : 1.4	Ti-6Al-4V [18]
320	322	846	1.0 : 2.6	Ti-6Al Alloys [49]
200	181	758	0.9 : 3.8	Ti-Al Alloys [128]
349	150	1107	0.4 : 3.2	CP Ti [136]

Table B.4: Reported values for the initial slip system strengths for the hexagonal phase of various Titanium alloys, including relative ratios normalized by each set's basal strength.

Other model parameters (Table B.5) were chosen to limit the magnitude of hardening and effectively suppress evolution of the saturation strength. Recent studies suggest the possibility that the strain rate sensitivity may be variable across slip families [57]. Doubling the rate sensitivity for the prismatic or pyramidal slip systems leads to only a 7% change in the slip strength to maintain a constant shear rate at a fixed resolved shear stress. For experiments and simulations conducted at low fixed strain rates, the assumption of a single strain rate sensitivity is not expected to have a large impact on results.

h_0 **(MPa)**	g_{s0} **(MPa)**	m	m'	$\dot{\gamma}_0$ **(s^{-1})**	$\dot{\gamma}_{s0}$ **(s^{-1})**
190	530	0.01	0.01	1.0	5×10^{10}

Table B.5: Plasticity parameters used for the α phase of Ti-6Al-4V.

B.2.3 Strength-to-Stiffness Formulation

To better predict the succession of grains which have yielded as a function of orientation, a strength-to-stiffness metric is employed. A strength-to-stiffness metric is critical in predicting the behavior of crystals in low-strain regimes, and is useful in determining

the initial development of plasticity throughout a polycrystal. While the strength to stiffness ratio may not be of critical importance in predicting high strain behavior such as that experienced during processing, it is absolutely critical to predicting yielding, fatigue, and ductility. A structural analog is useful in illustrating the importance of a strength-to-stiffness metric in polycrystalline materials [129]. Consider two masses loaded in parallel (isostrain) with different directional yield strengths and directional moduli (Figure B.4(a)). The two masses may not yield in succession as expected when considering only their directional yield strengths. In this case, the mass with a larger yield stress also has a larger directional modulus, such that it reaches its yield stress at a lower strain than the mass with a lower yield stress and lower directional modulus (Figure B.4(b)). The succession of yield in the two masses is better described by a strength-to-stiffness metric, which predicts the mass to yield first would be that with the lower ratio of directional strength to directional stiffness.

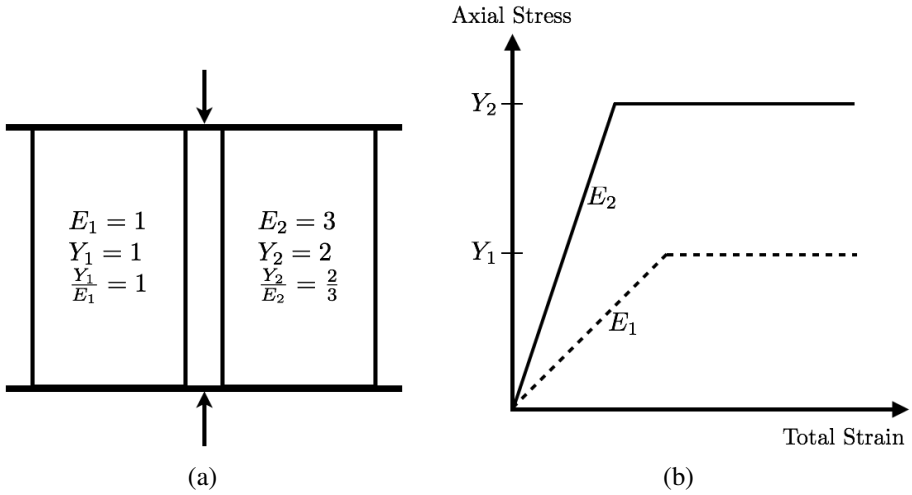

Figure B.4: Illustrations depicting the (a) masses and loading considered in the structural analog and (b) perfectly elastic-plastic behavior of each mass loaded separately, showing that the mass with a higher yield strength would be the first to yield under parallel loading.

The appropriate extension from this illustrative system is to consider many masses under similar loads, such as a polycrystalline material subjected to uniaxial tension.

Each grain in the aggregate may have a complex stress state due to the effects of elastic anisotropy, plastic anisotropy, and the loading of its neighbors. A first-order directional strength-to-stiffness metric may be calculated, however, assuming a uniaxial stress state in the same direction as the applied load. Previous study on FCC crystals reveals that for high degrees of single crystal anisotropy, the isostress assumption leads to the over-prediction of strength-to-stiffness values for certain crystallographic fibers compared to those predicted using more specific fiber averaged stress values [129]. For Ti-6Al-4V, the isostress assumption provides a reasonable estimate for strength-to-stiffness because the level of elastic anisotropy exhibited by the α phase is relatively low.

To obtain the directional modulus in general, the elastic compliance tensor, **S** (the inverse of the stiffness tensor, **C**, in Equation B.1), is considered in the crystal reference frame. Crystals exhibiting hexagonal symmetry are elastically transversely isotropic, meaning the directional stiffness for a uniaxial stress state, E_{dir}, is dependent only on the angle, $\theta(\mathbf{r})$, between the crystal's c-axis and the loading direction [51]:

$$\begin{aligned}\frac{1}{E_{dir}(\mathbf{r})} = &\left(1-\cos^2(\theta(\mathbf{r}))\right)^2 s_{11} + \cos^4(\theta(\mathbf{r}))\, s_{33} \\ &+ \cos^2(\theta(\mathbf{r}))\left(1-\cos^2(\theta(\mathbf{r}))\right)(2s_{13}+s_{44})\end{aligned} \tag{B.6}$$

where s_{ij} are components of the symmetry reduced compliance tensor in the crystal reference frame. Figure B.5 details the directional stiffness as a function of θ.

To obtain the strength for a given orientation, the uniaxial stress state is transformed from the sample reference frame to the crystal reference frame, and the normalized resolved shear stresses, $\frac{\tau^k(\mathbf{r})}{g^k}$, for each slip system are each computed for an applied uniaxial stress. From this, the directional strength for a given orientation is defined as the inverse of the Schmid factor [106]:

$$S_{dir}(\mathbf{r}) = \frac{1}{m(\mathbf{r})} = \frac{1}{\max\left(\frac{|\tau^k(\mathbf{r})|}{g^k}\right)} \tag{B.7}$$

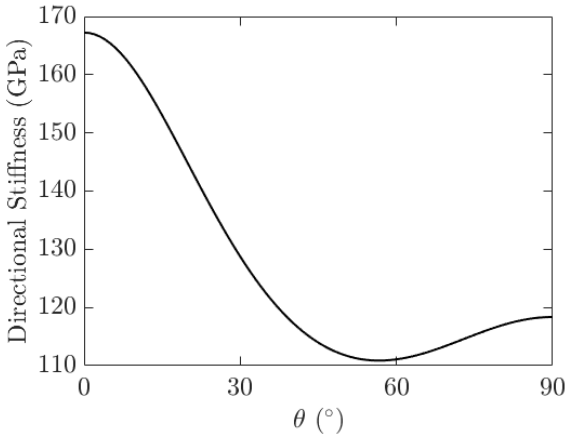

Figure B.5: Directional stiffness of the α phase in Ti-6Al-4V as calculated from elastic constants in Table B.2. θ is symmetrically bound between 0° (loading along the c-axis) and 90° (fully transverse).

where $m(\mathbf{r})$ is the orientation dependent Schmid factor. From the separate evaluations of stiffness and strength, the directional strength-to-stiffness parameter is constructed as,

$$r_{dir}(\mathbf{r}) = \frac{S_{dir}(\mathbf{r})}{E_{dir}(\mathbf{r})} \tag{B.8}$$

Since the single crystal elastic constants are held fixed in this study, the contribution of the directional stiffness to the strength-to-stiffness parameter remains constant across the simulations. However, the relative slip system strengths are variable (Table B.3) and each strength set will have a unique influence on the strength-to-stiffness values.

Pole distributions are useful in displaying the results graphically. Each point on the unit sphere corresponds to a crystallographic orientation, in which the c-axis, **c**, will form some angle between the loading direction, **d** - which is in this case parallel to the RD direction. The computation consists of evaluating the strength-to-stiffness ratio for each crystallographic orientation defined by the points on the unit sphere, thus defining a pole distribution. For display, the distribution is presented as a stereographic projection onto a plane perpendicular to the loading axis. Figure B.6 details the directional strength-to-stiffness ratios for the various sets of initial slip system strength.

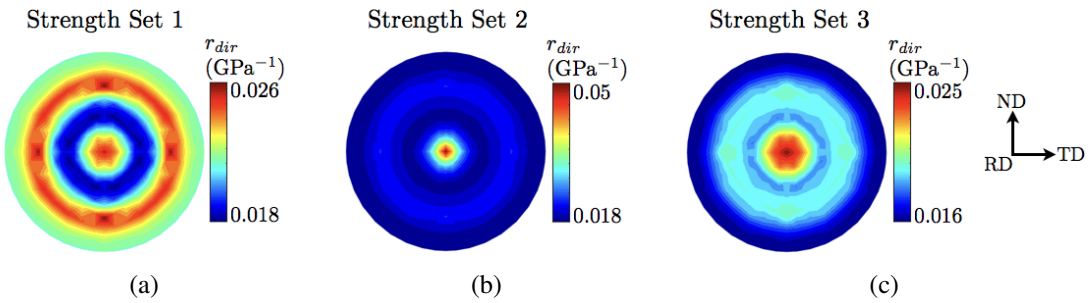

Figure B.6: Directional strength-to-stiffness parameters plotted on the (0 0 0 1) pole figures looking down the RD axis (center of plots represent the alignment of the (0 0 0 1) crystallographic direction with the sample's rolling direction). Plots show strength-to-stiffness parameters calculated using (a) Strength Set 1, (b) Strength Set 2, and (c) Strength Set 3.

Note that the pole figures are nearly axisymmetric about their RD axes, with only minor azimuthal fluctuations in magnitude. To this point, Figure B.7 details the directional strength-to-stiffness assuming both elastic and plastic transverse isotropy to more compactly illustrate the metric. Practically, this is achieved by calculating averages of the strength-to-stiffness values azimuthally about the RD axes of the pole figures found in Figure B.6. Note the general differences - in both character and magnitude - between the curves of the strength-to-stiffness parameters calculated using different strength sets. Specifically, note the values when the loading is parallel to the c-axis ($\theta = 0°$, or the center of the pole figures), and when the loading is fully transverse ($\theta = 90°$, or the periphery of the pole figures).

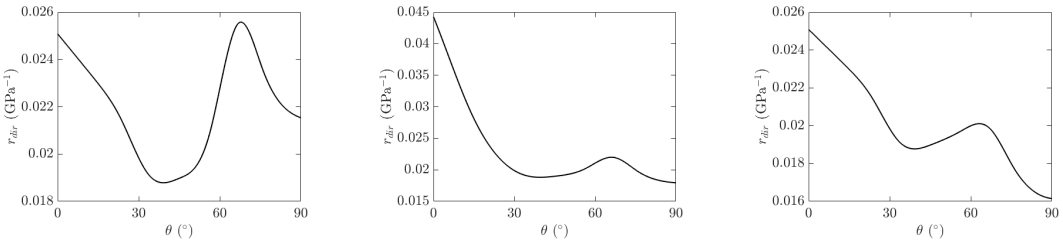

(a) (b) (c)

Figure B.7: Average directional strength-to-stiffness parameters plotted against θ - the angle between the loading direction and a crystal's c-axis. Plots show strength-to-stiffness parameters calculated using (a) Strength Set 1, (b) Strength Set 2, and (c) Strength Set 3.

B.3 Simulations and Results

B.3.1 Instantiation

Geometric representation of the microstructure is achieved through the use of Laguerre tessellations. Control over grain size (relative equivalent diameter) was achieved through the use of a normal distribution with mean 1 and standard deviation 0.045, while control over grain shape (sphericity) was achieved through the use of a lognormal distribution with mean -0.145 and standard deviation of 0.03 [61, 94]. These parameters facilitate a grain morphology comprised of near-equiaxed grains (Figure B.9), similar to those experimentally observed in Figures B.1 and B.2(a) and representative of the measured grain size distribution in Figure B.8, which exhibits a roughly normal distribution of grain sizes for the α phase.

In previous studies [39], the β phase was shown to allow the formation of bands of localized plastic strain over α grains on either side of a β phase lath (Figure B.3), contributing to long-ranging strain localization. However, the extent of resistance to transmission that the β phase presents between neighboring α phases is a complicated

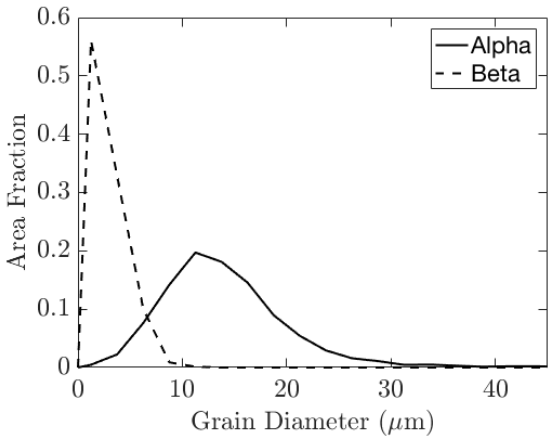

Figure B.8: Grain size distribution of the α and β phases of equiaxed mill annealed Ti-6Al-4V, as measured from the 2x1.5 mm EBSD scan in Figure B.2(a).

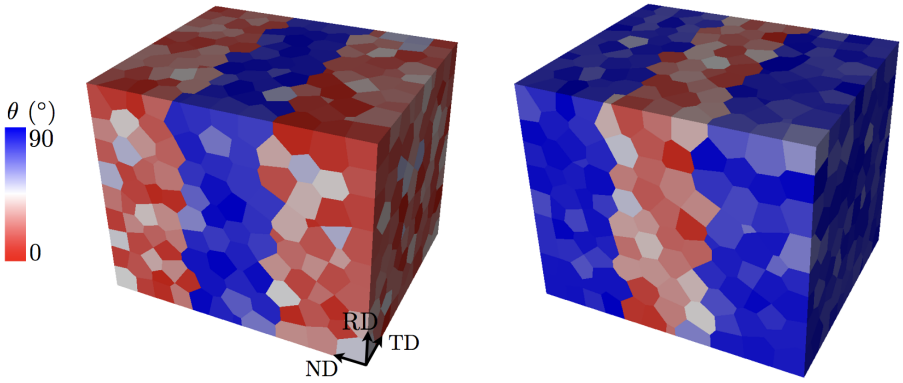

(a) (b)

Figure B.9: Polycrystal visualizations of the angular deviation of the (0 0 0 1) crystal direction from the sample's rolling/tensile direction (RD). (a) Instantiation 1, containing an embedded microtextured region sampled from the region B ODF, and (b) Instantiation 2, containing an embedded microtextured region sampled from the region A ODF. In both instantiations, regions outside of the embedded microtextured region were sampled from the other microtextured region's ODF.

research topic [19, 105, 117] that can be simplified by investigating single α phase alloys. Furthermore, the β phase laths do not fully encapsulate α phase grains, leading to primarily α-α contact. To alter observed trends, the β phase would have to substantially alter the stress states in the α phase grains, which is not expected due to the primary grain contact. Additionally, both the elastic and plastic behaviors of the β phase are poorly understood or quantified, and inclusion of the β phase would not reduce uncertainty in the present study. As such, simulations focus on only the α phase - β phase laths between α phase grains are not included in the instantiations. Each instantiation is comprised of 1200 α phase grains. The mesh contains approximately 1000 elements per grain, to facilitate the inspection of deformation at the intragrain level.

Grains are assigned to spatial regions based on the spatial location of their centroid. The microtextured regions at the center of these instantiations are designed to have approximately four grains across their width to mimic the microtextured regions observed in EBSD scans. Generally, orientations are assigned to grains by randomly sampling from the ODFs informed by the EBSD surface scans. Microtextured regions are modeled in the instantiations by assigning grains to spatial regions based on the location of their centroids. Orientations are then assigned to grains within each spatial region by sampling from only one microtextured region ODF per region - ensuring localized microtexturing. Each microtextured region contains approximately 400 grains, or a third of the total volume.

To account for potential bias introduced by sampling only a single microtextured region per instantiation, two instantiations are created - one with an embedded microtextured region sampled from the region B ODF (Figure B.9(a)), and one with an embedded microtextured region sampled from the region A ODF (Figure B.9(b)).

Symmetry boundary conditions are employed [34], where loading is applied in the

direction of the material's rolling direction. Three faces are symmetry planes, while one ND-RD face and one RD-TD face are traction free, and one ND-TD face is the loading control surface. Velocities are applied for an effective engineering strain rate of 10^{-3} s^{-1} to mimic the strain rate of the experiment.

B.3.2 Results

Figures B.10 and B.11 detail (0 0 0 1) pole figures with the discrete orientations of grains considered to have active slip systems. Two thresholds must be met for a grain to be considered active for a given family of slip systems. First, a slip system from any family at each element of the mesh is considered active based on a threshold relating its shear rate to the applied strain rate ($\dot{\epsilon}_{app}$):

$$\dot{\gamma} \begin{cases} < \frac{1}{10}|\dot{\epsilon}_{app}| & \text{inactive} \\ \geq \frac{1}{10}|\dot{\epsilon}_{app}| & \text{active} \end{cases} \tag{B.9}$$

Note that elemental results presented consider the model's results calculated at an element's centroid. Next, a grain is considered active based on a volumetric threshold, calculated by considering the sum of the volumes of all the elements in a given grain (V_{grain}) and the sum of the volumes of the elements with active slip systems (V_{active}):

$$V_{active} \begin{cases} < \frac{1}{10}V_{grain} & \text{inactive} \\ \geq \frac{1}{10}V_{grain} & \text{active} \end{cases} \tag{B.10}$$

Results were insensitive to either threshold through the range of [0.01 : 0.25], and as such 0.10 was chosen arbitrarily within this range.

Each plot details the full spherical pole figure from a viewpoint looking down the rolling direction axis, similar to Figure B.6. Table B.6 details the approximate engineer-

ing strains at which each slip family first activates for each instantiation and strength set.

Instantiation, Strength Set	% Strain (basal : prismatic : pyramidal)	% Strain at Yield
1,1	0.53 : 0.66 : 0.70	0.91
1,2	0.53 : 0.55 : 1.00	0.86
1,3	0.53 : 0.49 : 0.70	0.82
2,1	0.54 : 0.66 : 0.72	0.92
2,2	0.54 : 0.54 : 1.00	0.82
2,3	0.54 : 0.49 : 0.71	0.76

Table B.6: Engineering strains at which slip system families first activate, and engineering strains at macroscopic yield (0.1% offset method).

B.4 Discussion

In this study the rolling direction is coincident with the loading direction, and henceforth "rolling direction" will refer to both the rolling direction of the material and the sample's loading direction. Additionally, the region between the periphery (outer circumference) of the pole figure plots and the center of the pole figure plots - that is, the region where the c-axis is neither aligned nor orthogonal to the rolling direction - will be referred to as the "intermediary region of the pole figure".

B.4.1 Pole Figures

Little difference is observed between simulations conducted with Instantiation 1 and simulations conducted with Instantiation 2, and as such the results are discussed simultaneously. Inspection of the pole figures shown in Figures B.10 and B.11 reveals immediate trends concerning grain activation. Broadly speaking, orientations with the lowest strength-to-stiffness values are the first to register slip activity, and orientations

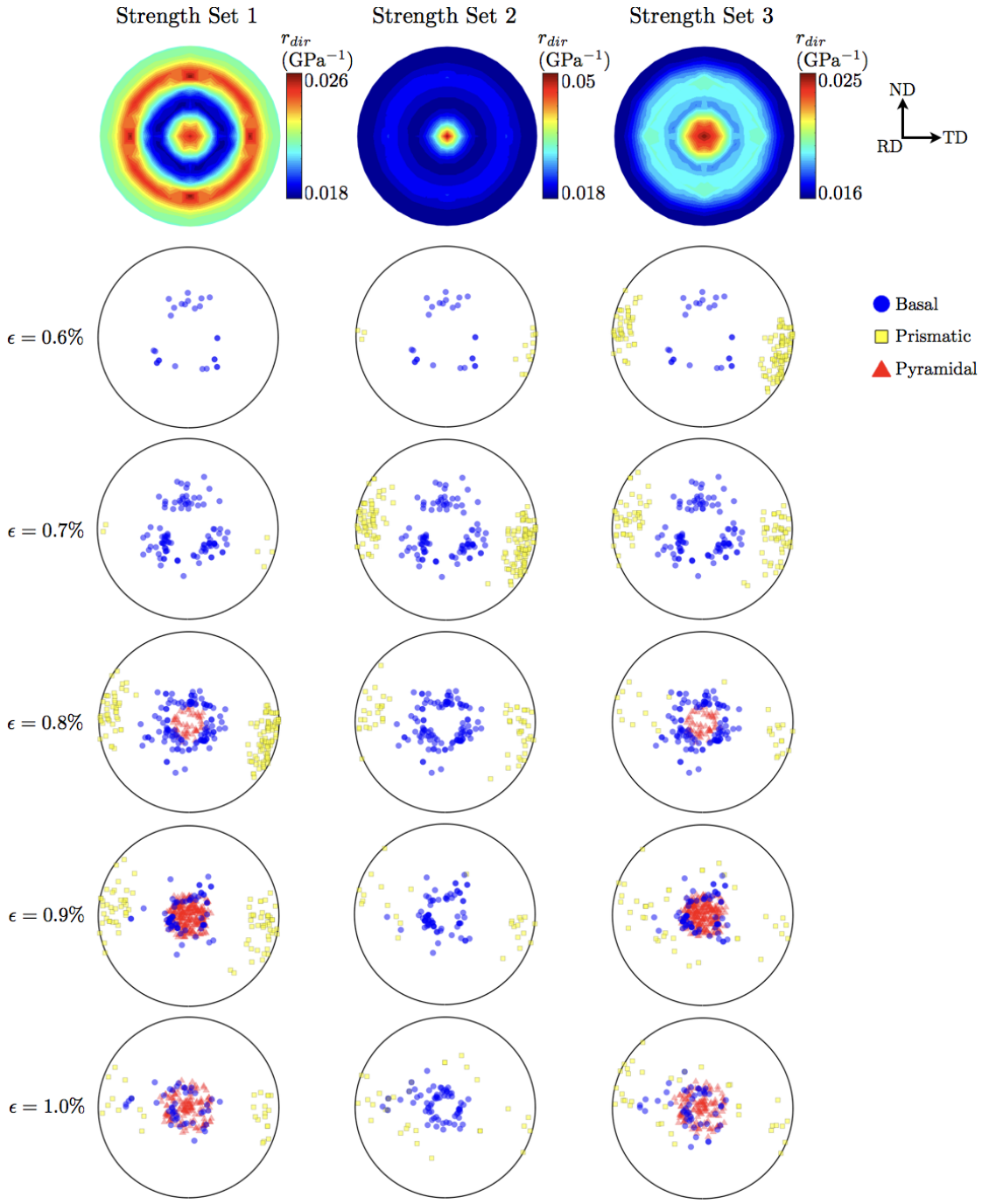

Figure B.10: (0 0 0 1) pole figures depicting grains with active slip systems at various macroscopic engineering strains for the simulation conducted using Instantiation 1 and various slip system strength sets (Table B.3). At each strain, pole figures depict newly active grains - that is, grains which were not active at a previous strain state.

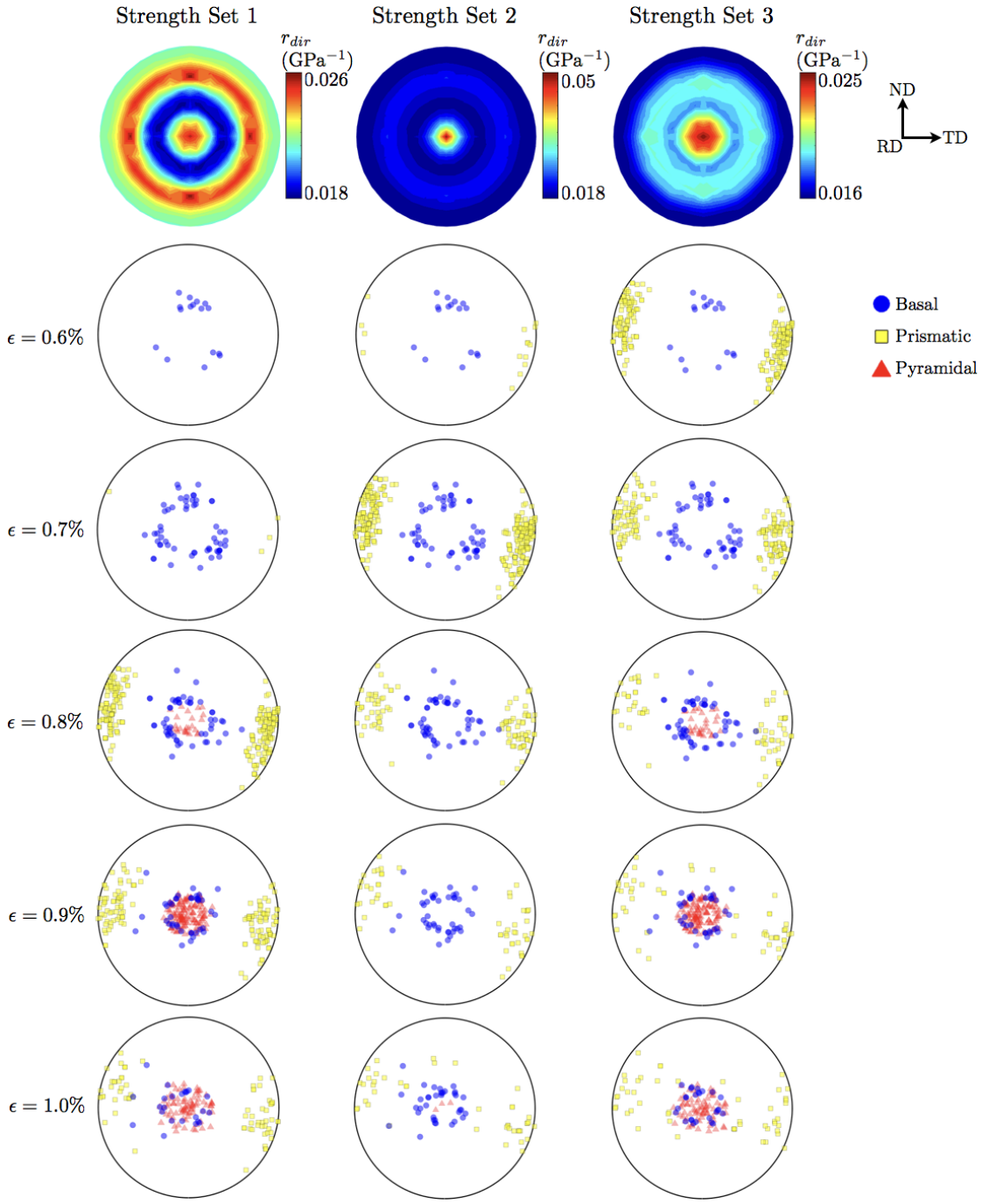

Figure B.11: (0 0 0 1) pole figures depicting grains with active slip systems at various macroscopic engineering strains for the simulation conducted using Instantiation 2 and various slip system strength sets (Table B.3). At each strain, pole figures depict newly active grains - that is, grains which were not active at a previous strain state.

with higher strength-to-stiffness values activate at higher strains. Key differences, however, are apparent between each simulated strength set.

Inspecting the pole figures in the first columns of Figures B.10 and B.11 - those corresponding to the simulations conducted with Strength Set 1 - reveals that crystals in the intermediary region of the pole figure are the first to activate. This is consistent with the strength-to-stiffness plot for Strength Set 1 presented at the tops of the first columns, as the intermediary region of the pole figure has the lowest strength-to-stiffness values. Orientations with their c-axis orthogonal to the rolling direction are the second to activate, and orientations with their c-axis aligned with the rolling direction activate last - again, both consistent with the strength-to-stiffness values.

The pole figures in the second columns of Figures B.10 and B.11 - those corresponding to the simulations conducted with Strength Set 2 - reveal a different trend. Grains in the intermediary region of the pole figure activate at roughly the same strain as those with their c-axis orthogonal to the loading direction, while grains with their c-axis aligned with the rolling direction are again the last to activate - notably at a much higher strain than in simulations conducted with other strength sets. The strength-to-stiffness plot for Strength Set 2 presented at the tops of the second columns shows that the strength-to-stiffness values for the intermediary region of the pole figure are comparable to the values for the periphery of the pole figure, while the center of the pole figure has the highest strength-to-stiffness values. Again, the order in which orientations activate are supported by the relative values for the strength-to-stiffness parameter.

Finally, the pole figures in the third columns of Figures B.10 and B.11 - those corresponding to the simulations conducted with Strength Set 3 - reveal that grains in the intermediary region of the pole figure again activate at roughly the same strain as those with their c-axis orthogonal to the loading direction, followed by grains with their c-axis

aligned with the rolling direction, though at a lower strain than in the pole figures in the second columns of Figures B.10 and B.11. This again obeys the strength-to-stiffness plot for Strength Set 3 presented at the tops of the third columns.

B.4.2 Slip System Families

The order in which slip system families activate with relation to the strength-to-stiffness parameter may also be explored. Table B.6 details the engineering strains at which the each slip family first registers activity in the polycrystal for each simulated instantiation and strength set. Again, little difference is noted between simulations conducted with Instantiation 1 or Instantiation 2. However, differences are evident between simulations conducted with different strength sets. The strains at which activation is first registered for each slip family correlates well with the initial slip system strengths used for each simulation - relative strains at activation match the ordering of relative slip system strengths.

The pole figures also reveal phenomena pertaining to the clustering of orientations with the same slip family active. Grains in the center and periphery of the (0 0 0 1) pole figures are from the microtextured regions sampled from the region A and B ODFs, respectively, while grains in the intermediary region of the pole figure may come from either microtextured region. The clustering of like orientations in the center and along the periphery of the pole figures reveals microtextured regions activating with a certain slip family. The pole figures in the first column of Figure B.10, for example, reveal that the grains at the periphery of the pole figure initially activate with only prismatic slip systems, while grains at the center of the pole figure initially activate with only pyramidal slip systems. This indicates that grains that exhibit pyramidal activity reside

in microtextured regions corresponding to the region A ODF, while grains that exhibit prismatic activity reside in microtextured regions corresponding to the region B ODF. Grains in the intermediary region of the pole figure initially activate with only basal slip systems. These trends hold true for the other simulated instantiations and strength sets.

In previous work, high resolution scanning electron microscope images were collected to measure the onset of plastic strain localization, using the digital image correlation technique (SEM DIC) [39, 115]. SEM DIC strain field measurements were performed on the same Ti-6Al-4V material investigated in this study, in region from the field of view in Figure B.2(a). Bands of localized plastic deformation and their relative slip systems were identified from the strain field measurements at 0.65% and 0.71% engineering strain. Comparison to the experimentally measured slip activity, shown in Figure B.12(a) [39] reveals good correlation with the simulated results obtained using Strength Set 1. Experiments were conducted at a limited number of strain steps, and thus precise strains at which each slip family activates were not obtained. At 0.65% engineering strain, a relatively large number of grains register basal activity (in the intermediary region of the pole figure only), whereas only a few grains register prismatic activity (on the periphery of the pole figure only), and no grains register pyramidal activity. At 0.71% engineering strain, both the intermediary region and periphery of the pole figure continue to register new basal and prismatic activity, respectively, while the center of the pole figure registers a small number of grains with pyramidal activity.

Simulations conducted with Strength Set 1 have average activation engineering strains of 0.54%, 0.66%, and 0.71% for the basal, prismatic, and pyramidal families, respectively. Figure B.12(b) shows pole figures for the simulation conducted with Instantiation 1 and Strength Set 1 at 0.65% and 0.71% engineering strains. At 0.65% engineering strain, a relatively large number of grains register basal activity in the in-

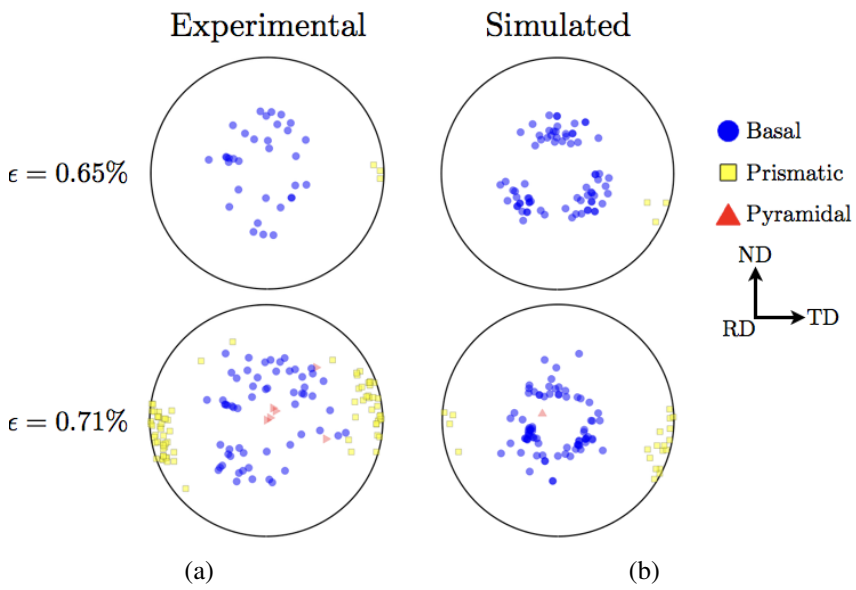

Figure B.12: (a) Experimental and (b) simulated (0 0 0 1) pole figures depicting grains with newly active slip systems at fine strain increments of 0.65% engineering strain and 0.71% engineering strain.

termediary region of the pole figure, while a small number of grains register prismatic activity around the periphery of the pole figure. A single grain at the center of the pole figure registers pyramidal activity at 0.71% engineering strain, with continued basal and prismatic activity in the intermediary region and periphery of the pole figure, respectively.

Other simulated strength sets produce results that do not match experimental observations. Simulations conducted with Strength Set 2 have an average engineering strain of 1.00% at which pyramidal activity is first witnessed - much higher than the average engineering strains at which the other two families first activate (0.54% and 0.55% for basal and prismatic, respectively). Additionally, Strength Set 2 produces a comparable amount of grains with basal and prismatic activity at 0.65% engineering strain, and no pyramidal activity at 0.71% engineering strain. Simulations conducted with Strength Set 3 have an average engineering strain at which prismatic activity is first witnessed

of 0.40%, below the average engineering strain at which grains with basal activity first appear (0.54%). Additionally, Strength Set 3 produces more grains with prismatic activity at 0.65% engineering strain. In other words, the strength set with a weak basal system, and a moderately high pyramidal strength (Strength Set 1) best captures the observed trends in slip system family activation, while the strength set with a high pyramidal strength (Strength Set 2) registers pyramidal activation at an engineering strain far above what was observed experimentally, and the strength set with a weak pyramidal system (Strength Set 3) registers pyramidal activation before basal activation, which produces relative numbers of active grains for each family that differ from experimental observations.

B.4.3 Behavior in Aggregate Subsets

Results considering different subsets of grains were compiled to account for any potential bias introduced by considering interior and surface grains separately or together. Table B.7 details the strains at which each slip family first registers activity for each instantiation and strength set when considering only the grains on traction free surfaces (to mimic experimental EBSD scans), as well as when considering all interior grains. Little difference is witnessed when considering subsets of the aggregate or the entire aggregate, though the calculated strains at which slip families activate when considering only the traction free surface tend to be marginally higher than those calculated when considering the interior grains, which in turn tend to match (with few deviations) the calculated strains when considering the entire aggregate.

Instantiation, Strength Set	% Strain - Surface (basal : prismatic : pyramidal)	% Strain - Interior (basal : prismatic : pyramidal)
1,1	0.55 : 0.68 : 0.74	0.53 : 0.66 : 0.70
1,2	0.55 : 0.57 : 1.05	0.53 : 0.55 : 1.00
1,3	0.55 : 0.51 : 0.74	0.53 : 0.49 : 0.70
2,1	0.54 : 0.68 : 0.72	0.54 : 0.66 : 0.71
2,2	0.54 : 0.57 : 1.05	0.54 : 0.54 : 1.00
2,3	0.54 : 0.51 : 0.71	0.54 : 0.49 : 0.73

Table B.7: Engineering strains at which slip systems first activate when considering only traction free surfaces or all interior grains.

B.4.4 Effects of Microtextured Regions

To probe the influence of microtextured regions, two additional instantiations were produced in which the same orientation sets for Instantiations 1 and 2 were randomly assigned to grains - that is, with no microtextured regions. Figure B.13 shows visualizations of these new instantiations containing the same orientation sets, but no microtextured regions. Table B.8 details the engineering strains at which each slip family activates for simulations conducted with these two new instantiations and each strength set. Activation strains deviate somewhat from those in Tables B.6 and B.7, but the observed trends concerning the order of slip family activation are consistent with the trends observed in simulations performed with microtextured regions, implying that microtextured regions have little influence on this metric.

Instantiation, Strength Set	% Strain (basal : prismatic : pyramidal)	% Strain at Yield
3,1	0.54 : 0.61 : 0.72	0.90
3,2	0.54 : 0.50 : 1.00	0.84
3,3	0.54 : 0.38 : 0.69	0.80
4,1	0.55 : 0.65 : 0.77	0.91
4,2	0.54 : 0.54 : 1.00	0.81
4,3	0.55 : 0.55 : 0.72	0.75

Table B.8: Engineering strains at which slip systems first activate for simulations conducted without the presence of microtextured regions, and engineering strains at macroscopic yield (0.1% offset method).

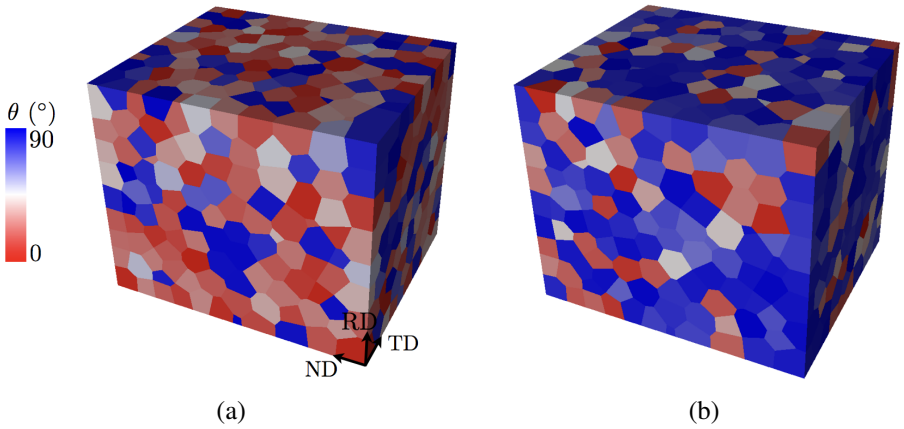

Figure B.13: Polycrystal visualizations of the angular deviation of the (0 0 0 1) crystal direction from the sample's rolling/tensile direction (RD). (a) Instantiation 3 contains the same orientation set as Instantiation 1, but with a random spatial assignment of orientations, and (b) Instantiation 4 contains the same orientation set as Instantiation 2, but with a random spatial assignment of orientations.

Microtextured regions, however, have an effect on the localization of plasticity within the aggregate. Figure B.14 details the grains within polycrystals of two representative simulations (one conducted with the presence of microtextured regions, and one without), colored if they are considered active for a certain slip family (Equations B.9 and B.10). Note that for the simulation conducted with the presence of microtextured regions, active grains within each microtextured regions are active in the same slip family - that is, the regions in which the c-axis is perpendicular to the loading direction have grains which exhibit prismatic slip, while the region in which the c-axis is aligned with the loading direction exhibits primarily basal slip. The microtextured regions also facilitate the development of long-range regions of localized plastic strain spanning multiple contiguous grains. Most evident is the strain caused by shear on basal slip planes that is shown to have developed in the center microtextured region, which spans across neighboring grains, but terminates at the boundaries of the microtextured region. This strain localization occurs while the aggregate is still in the elastic regime (Table B.6).

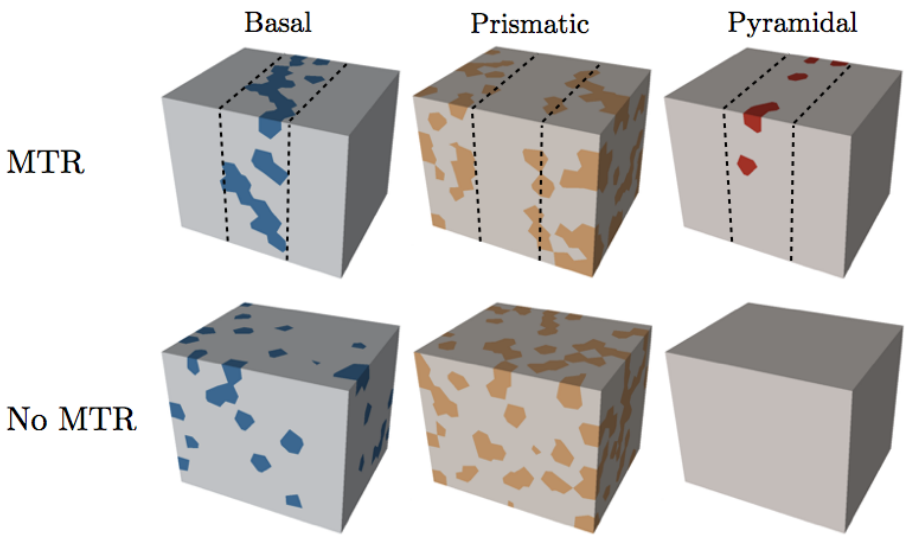

Figure B.14: Visualizations detailing the spatial distribution of grains with active slip families at 0.77% engineering strain for simulations conducted with Strength Set 1/Instantiation 2 (with the presence of microtextured regions, whose approximate boundaries are demarcated by dashed lines), and Strength Set 1/Instantiation 4 (without the presence of microtextured regions).

Conversely, the simulations conducted without the presence of microtextured regions exhibit a more disperse distribution of plasticity. Whereas the microtextured regions facilitate the localization of plasticity by means of specific slip family activity, their absence allows for plasticity to develop anywhere in the polycrystal. Additionally, the dispersion of slip activity across the polycrystal suppresses the formation of long-range plasticity localization before the onset of macroscopic yielding (Table B.8). The shift from plasticity within single grains to coordinated long-ranging plasticity localization across grains with similar grain orientations in microtextured regions is likely to be detrimental to ductility.

These results align well with experimental results (Figure B.15 [39]) in which long-range bands of plastic deformation form that traverse grain boundaries, but terminate along the boundaries of microtextured regions. This localization is observed to occur

before the onset of macroscopic yield. This is most evident in "MTR 1", which shows a long band of plastic deformation achieved by slip on the prismatic plane traversing multiple grains across the microtextured region, but terminates at the borders. Furthermore, plasticity within microtextured regions is witnessed to be generally restricted to a single slip family. This supports both the simulated results described in Section B.4.2, in which the pole figures display the clustering of orientations with the same slip family activated, as well as the results plotted in Figure B.14.

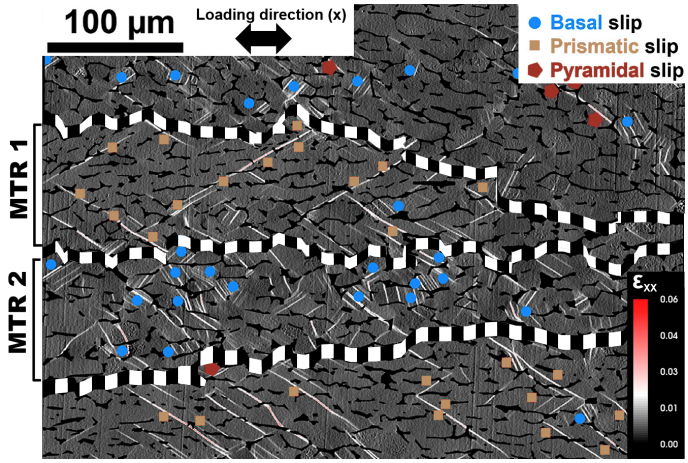

Figure B.15: Experimental strain map measured using SEM DIC during monotonic loading at 0.71% engineering strain (below macroscopic yielding). The type of slip system activity is indicated for basal (blue), prismatic (orange), and pyramidal (red) in the strain map. The slip type was determined by comparing the calculated plastic strain on the surface from the EBSD orientation data to the observed localization in the DIC measurements. The MTRs were determined from the EBSD orientation data and are demarcated by the dashed black and white lines in the strain map for better visualization.

B.4.5 Influence of the Slip System Hardening Assumption

Recent studies of hexagonal materials have proposed and utilized more complex hardening assumptions than the Voce form utilized in this study [91, 87]. In the plastic

region of deformation, these hardening models have a large impact on the deformation response of the sample. At the low strain values interrogated in this study, and for a material that exhibits little hardening, the hardening model is not expected to impact the findings regarding the initiation of slip. To determine the sensitivity of the results of this study to the comparatively simple isotropic hardening assumption, additional simulations were conducted using Instantiations 1 and 2, and Strength Sets 1, 2, and 3. Two different hardening assumptions were explored - the case of no hardening ($g_0^k = g_{s0}^k$ for all slip systems k, Equation B.5), and the case of self hardening, where each slip system hardens independently [23]. Table B.9 details the results of these simulations in terms of the strains at which each slip family activates.

Hardening Assumption	**Instantiation, Strength Set**	**% Strain (basal : prismatic : pyramidal)**
No Hardening	1,1	0.55 : 0.68 : 0.72
	1,2	0.55 : 0.57 : 1.05
	1,3	0.55 : 0.51 : 0.72
	2,1	0.56 : 0.68 : 0.74
	2,2	0.56 : 0.56 : 1.05
	2,3	0.56 : 0.51 : 0.73
Self Hardening	1,1	0.55 : 0.68 : 0.72
	1,2	0.55 : 0.57 : 1.05
	1,3	0.55 : 0.51 : 0.72
	2,1	0.56 : 0.68 : 0.74
	2,2	0.56 : 0.56 : 1.05
	2,3	0.56 : 0.51 : 0.73

Table B.9: Engineering strains at which slip system families first activate when considering different hardening assumptions.

Both the case of no hardening and the case of self hardening result in slightly higher strains at activation that the results presented in Table B.6 - though not significantly. More importantly, however, the relative strains at activation are consistent with the results found with the case of isotropic hardening. In all cases, the trends observed in the results from the simulations conducted with isotropic hardening are the same with the two other hardening assumptions. When viewing the results at coarser strain states (Fig-

ure B.16), the results are nearly indistinguishable from those found with the isotropic hardening assumption (first column of Figure B.10).

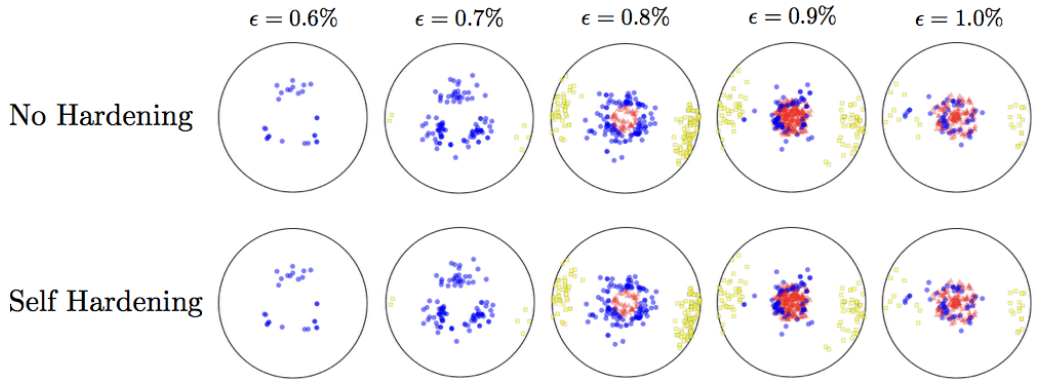

Figure B.16: Comparisons of results assuming no hardening and full self hardening for simulations conducted using Instantiation 1 and Strength Set 1. Compare to the first column of Figure B.10.

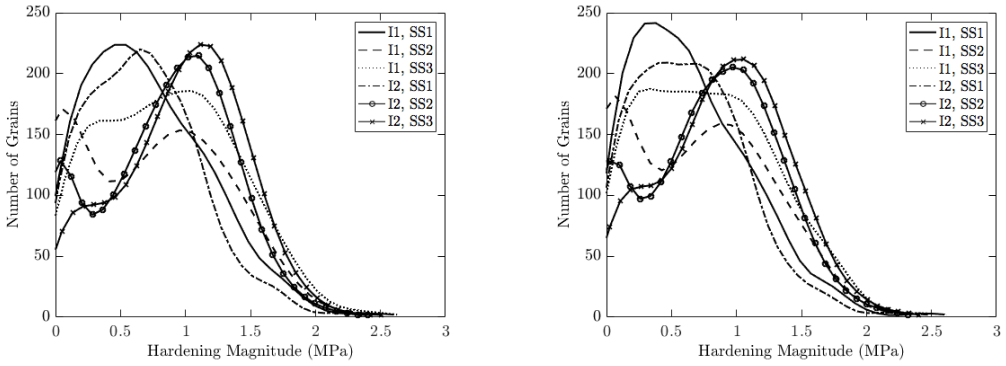

(a) (b)

Figure B.17: Grain averaged hardening magnitude distribution at 1.00% strain for simulations conducted with (a) an isotropic hardening assumption, and (b) a self hardening assumption. Legends refer to the instantiation and strength set used in each simulation, e.g. "I1, SS3" for Instantiation 1, Strength Set 3.

Additionally, the grain averaged magnitude of hardening is calculated for the simulations with isotropic hardening or self hardening. In the case of isotropic hardening, the hardening magnitude is simply averaged across the grain (weighted by the element volume). In the case of self hardening, the hardening magnitude considers the largest

slip system hardening magnitude per element, which is in turn averaged across the grain (again, weighted by the element volume). Figure B.17 shows the grain averaged hardening for all simulations performed with hardening at 1.00% strain - the maximum strain investigated in this study.

Hardening is seen to contribute minimally to the results of this study due in large part to the deformation regime in which this study focuses (elastic and elastic/plastic transition), in which the results are shown to be insensitive to the hardening assumption, and the magnitude of hardening is low compared to the slip system strengths.

B.5 Conclusion

A study of the effect of microtextured regions and relative initial slip system strengths for equiaxed mill annealed Ti-6Al-4V is presented. Single phase instantiations - namely the generation of the microstructural morphology and the formation of representative orientation distribution functions - were informed by experimental data gathered through 2D and 3D EBSD data. Simulations were conducted multiple times on each instantiation with different sets of initial slip system strengths. Results from the simulations were used to determine slip activity in grains at various strains, and the strains at which each slip system family activates were deduced. These results proved to be sensitive to the relative initial slip system strengths for the basal, prismatic, and pyramidal slip families. A strength-to-stiffness parameter - previously demonstrated to be successful for use with FCC materials and extended here for use with HCP materials - correctly predicted the succession of yield in all cases. Compared to experimental results, the order of grain activation and the relative number of grains which exhibited slip activity in each family were best modeled using a weak basal family strength, a slightly higher prismatic family

strength (1.2x basal), and moderately high pyramidal family strength (1.7x basal). Other sets of slip system strengths - including one with a high pyramidal family strength (3x basal), and another with a weak prismatic family strength (0.9x basal) - differed from experimental results in the relative magnitude of strain at activation, as well as the relative number of active grains for a given family at a given strain. Considering subsets of the aggregate - specifically grains which appear on traction free surfaces and interior grains - had little effect on these observed trends. Furthermore, the presence of microtextured regions had little effect on the initiation of slip, but proved to facilitate the formation of long-range plasticity localization within microtextured regions before the onset of macroscopic yield, compared to the disperse distribution of plasticity in simulations conducted without the presence of microtextured regions, which compares well with experimental observations.

Acknowledgements

Funding for this study was provided by the Office of Naval Research under grants N00014-12-1-0399 and N00014-16-1-2982, as well as the Cornell High Energy Synchrotron Source (CHESS) under NSF award DMR-1332208. Members of the Deformation Processes Lab at Cornell University are thanked for their helpful suggestions.

APPENDIX C

THE INFLUENCE OF MECHANICAL CONSTRAINTS INTRODUCED BY β ANNEALED MICROSTRUCTURES ON THE YIELD STRENGTH AND DUCTILITY OF TI-6AL-4V

The following appears in the *Journal of the Mechanics and Physics of Solids* [61].

Abstract

Discussed is a computational study of the influence of the microstructure's geometric morphology on the yield strength and ductility of Ti-6Al-4V. Uniaxial tension tests were conducted on physical specimens to determine the macroscopic yield strength and ductility of two microstructural variations (mill annealed and β annealed) to establish comparisons of macroscopic properties. A multi-experimental approach was utilized to gather two dimensional and three dimensional data, which were used to inform the construction of representative β annealed polycrystals. A highly parallelized crystal plasticity finite element framework was employed to model the deformation response of the generated polycrystals subjected to uniaxial tension. To gauge the macroscopic response's sensitivity to the morphology of the geometry, the key geometrical features - namely the number of high temperature β phase grains, α phase colonies, and size of remnant secondary β phase lamellae - were altered systematically in a suite of simulations. Both single phase and dual phase aggregates were studied. Presented are the calculated yield strengths and ductilities, and the resulting trends as functions of geometric parameters are examined in light of the heterogeneity in deformation at the crystal scale.

C.1 Introduction

Ti-6Al-4V is the most widely used titanium alloy, and is commonly used for critical components in many different engineering applications - desirable because of the concurrence of high strength, corrosion resistance, and low weight [75]. The thermomechanical processes the raw material is subjected to during manufacture have the potential to introduce a wide variety of microstructures, in turn altering the deformation response of the material. Representing two extremes of attainable microstructures are the mill annealed microstructure and the β annealed microstructure. Experimental observation has shown that the two microstructures are markedly different in terms of their geometric features and deformation response [35, 107]. The presence of two crystallographic phases, including a hexagonal crystallographic phase that exhibits strong elastic and plastic anisotropy [63, 118] adds complexity to the material's deformation response. How the microstructure effects the deformation response can be understood by considering the mechanical constraints that exist between the two crystallographic phases when equilibrium and compatibility are enforced. Understanding the microstructure-property relationship - specifically in regards to the estimation of the yield strength and ductility - is crucial in an alloy with such ubiquity, wide microstructural variability, and complex crystal scale behavior.

Simulating the deformation of these microstructures provides insight into the development of plasticity at the crystal scale, and the influence that the microstructure has on the resulting macroscopic behavior. Mathematical frameworks exist that describe the behavior of plastically deforming materials at the crystal scale [8, 78]. These crystal plasticity equations are often implemented in a finite element computational framework [77]. Due to constraints on computational capabilities, studies have historically been limited to simplified representations of microstructures [104, 95, 137], idealized mod-

els for the study of texture evolution [88], or detailed microstructural representations of limited scale [12]. Indeed, while other modeling techniques (e.g. mean field approaches such as the Taylor model or Sachs model) are able to estimate an aggregate's macroscopic response, high fidelity finite element modeling allows for a better understanding of the microstructure's influence on such a response by considering the spatial arrangement of grains and phases. The development of more efficient computational architectures, coupled with the use of highly parallelized code has allowed for the use of larger meshes, and thus the inclusion of fine geometric detail. Recent experimental and computational studies suggest that deformation occurs heterogeneously across individual grains, necessitating the use of high fidelity representations of microstructures in order to accurately predict the deformation response [85, 131].

Representation of a microstructure for use in such simulations is dependent on the experimental identification of key geometric features. Two dimensional methods, such as optical microscopy and EBSD provide detailed depictions of surface features of microstructures, yet are lacking due to their failure to elucidate three dimensional features. Recent developments in both destructive [38] and non-destructive [73] orientation mapping techniques allow for the construction of three dimensional maps - providing not only detailed information about the geometric features of a microstructure, but also the spatial distribution of crystallographic orientations. A multi-experimental approach allows for a better understanding of a microstructure's geometric morphology. These data, in turn, may be used to inform the generation of a potentially infinite number of randomly generated microstructure representations that contain features similar to those observed. Voronoi tessellations have proven to be an effective way to represent generic polycrystals [125, 10], and techniques and implementation have recently evolved to efficiently facilitate the creation of large polycrystals and attendant robust finite element meshes [93]. While sufficient in representing main features of the mill annealed mi-

crostructure, Voronoi tessellations alone are insufficient in accurately representing the fine details of the β annealed microstructure.

In this paper, we focus specifically on how attributes of the β annealed microstructure introduce mechanical constraints that affect the material's macroscopic properties. A method is described that creates an idealized version of the β annealed microstructure that includes the experimentally observed fine geometric features. A highly parallelized crystal plasticity finite element framework is used to simulate the deformation response. Details of the geometry are altered to gauge their influence on macroscopic behavior, and lower bound estimates on the yield strength and ductility are found. Following presentation of the macroscopic properties, concurrent responses at the crystal scale are examined. The influence of structure-imposed constraints within the microstructure on the intensity of deformation heterogeneity is demonstrated with contrasting images of evolving deformation rate banding for defining features of the microstructure. Further, the propensity for microstructure features to constrain slip activity to one or two systems is investigated in detail. The differences in responses at the crystal scale provide a better understanding of the particular features that most influence the trends observed at the macroscopic scale.

C.2 Background

C.2.1 Experimental Observations

The two crystallographic phases present in Ti-6Al-4V are the α phase, which exhibits hexagonal close packed crystal symmetry, and a secondary β phase, which exhibits body centered cubic crystal symmetry. These two phases represent approximately 92% and

8% of the volume, respectively, in both the mill annealed and the β annealed microstructures. The mill annealed microstructure is characterized by relatively small (O(10 μm)) equiaxed α phase grains with laths of β phase between grains. The β annealed microstructure is a complex network of thin β phase lamellae embedded in α phase transformation structures - or colonies - that form within large (O(500 μm)) equiaxed β phase grains present above the transus temperature. Figure C.1 displays optical micrographs of both microstructures.

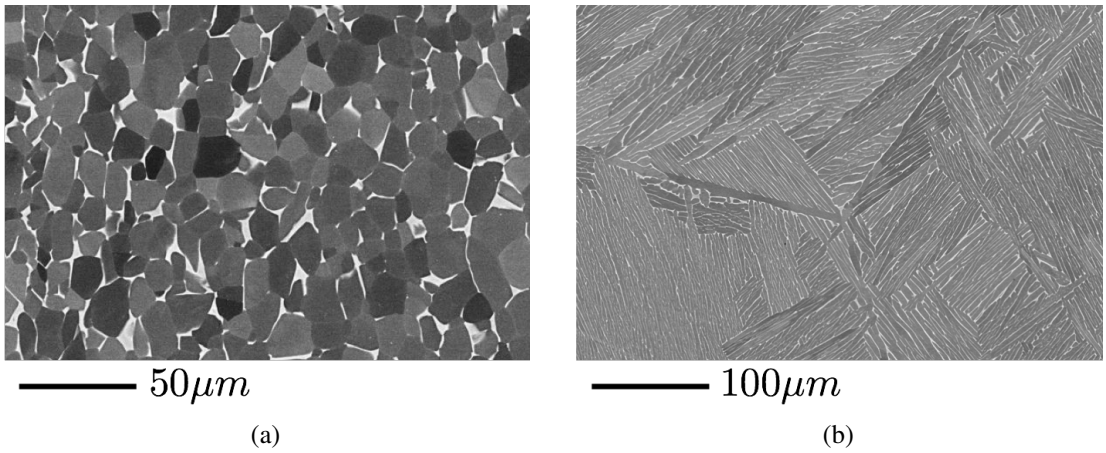

Figure C.1: Optical micrographs of the (a) mill annealed microstructure, and (b) β annealed microstructure. Darker regions of the micrographs are regions of α phase, and lighter regions represent β phase. (Reproduced from [75].)

Macroscopic Tensile Tests

Tensile tests were performed on samples with a 6.35 mm diameter circular cross section and gage length of 31.75 mm in order to characterize the differences in the yield strength and ductility between the two microstructures. Eight mill annealed samples were fabricated from a rolled sheet, each with its tensile direction aligned with the rolling direction, and eight β annealed samples were fabricated from a separate rolled sheet, each with its tensile direction aligned with the rolling direction. Tensile tests were conducted

monotonically at an engineering strain rate of 0.001 s^{-1}. Yield strength was calculated from the engineering stress-strain curve using a 0.1% offset.

A practical measure of ductility was chosen as the engineering strain at which the sample incurred the maximum engineering stress, or maximum load, which forms the basis for the Considère condition for stable deformation. Additionally, the amount of hardening - quantified as the difference between the ultimate tensile strength (the stress at ductility) and the yield strength - is included. Spreads in the offset yield strength, ductility, and hardening are calculated as each set's standard deviation. Table C.1 details the aggregate results of these tensile tests, while Figure C.2 shows example stress-strain curves for both microstructures. The β annealed microstructure exhibits a lower yield strength, a significantly lower ductility, and a larger amount of hardening than the mill annealed microstructure, as well as a larger degree of variability in all measures. Qualitatively, the mill annealed samples were smooth at the onset of necking, while the β annealed samples exhibited pronounced surface roughness (i.e., "orange-peel") - indicating the presence of large grains.

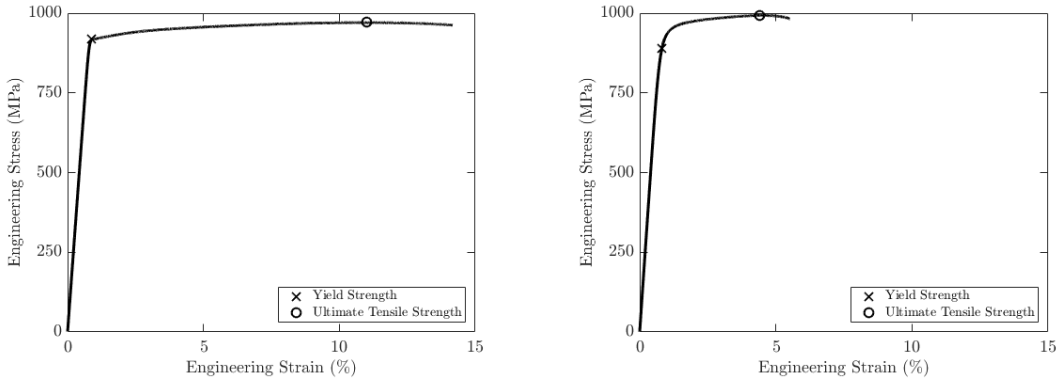

Figure C.2: Example experimental stress-strain curves for the (a) mill annealed microstructure and the (b) β annealed microstructure.

Microstructure	Yield Strength (MPa)	Ductility (%)	Hardening (MPa)
Mill Annealed	909.0 ± 4.8	11.6 ± 0.7	64.0 ± 18.3
β Annealed	898.6 ± 30.5	4.3 ± 1.1	96.6 ± 22.9

Table C.1: Yield strength, ductility, and hardening calculated from macroscopic tensile tests.

High Energy Diffraction Microscopy

To gain insight on the three dimensional geometric morphology of the β annealed microstructure, a high energy X-ray diffraction experiment was performed by other investigators working on this same material [127]. A sample with a 1 mm square cross section was interrogated. This sample was cut from the same rolled sheet as the macroscopic tensile test samples. Diffraction peaks were recorded in the near field regime - that is, with the detector sufficiently close to the sample such that both crystallographic orientation and spatial location associated with a Bragg peak may be deduced [73]. An X-ray beam of width 1.2 mm and height 2 μm was used to illuminate a planar slice of the sample, and a spatial map of orientations for the plane was deduced. The sample was successively translated through the beam such that a total of 30 planar orientation maps were available. When stacked, these planar maps form a three dimensional spatial map of orientations (with a total height of 0.75 mm). Detector resolution was such that only α phase structures were characterized experimentally (Figure C.3(a)).

Because the α phase colonies are transformation structures within grains comprised solely of β phase crystals present when the material was rolled above the transus temperature, the morphology of the prior β phase (Figure C.3(b)) could be determined based on established methods [45]. Qualitatively, the pre-transformation β phase structure was shown to have relatively large equiaxed grains with angles of $\sim$120° at triple junctions. This suggests an equilibrium state, and thus a grain-growth microstructure [101].

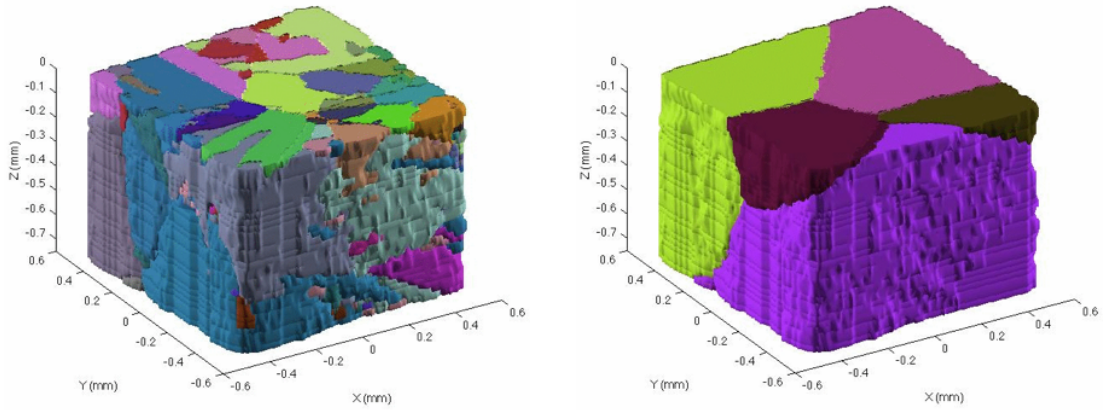

(a) (b)

Figure C.3: Near field high energy X-ray diffraction reconstructions. (a) Measured α-phase orientation map, (b) calculated prior β-phase orientation map. (Reproduced from [127].)

C.2.2 Simulation Methods

The model employed in this study is an elastic-viscoplastic model embedded in a highly parallelized finite element framework. This method is capable of modeling large inelastic, quasi-static deformations of a polycrystal discretized into a finite element mesh. The deformation of the material is described using a set of constitutive equations, and we consider both an elastic response and inelastic response of a single crystal. Anisotropy is included in the elastic response, as well as the inelastic response, which considers only rate-dependent crystallographic slip restricted to dominant slip systems. Deformation twinning is not observed in Ti-6Al-4V due to its high aluminum content [75] and consequently was not modeled. Deformation is considered to be ductile and isothermal - no heat transfer or fracture models are included. Simulations are performed using the FEpX software package [32]. Here, a simplified summary of the model is described. A more complete description of the kinematics and configuration may be found in the FEpX theory and methods manual [32].

The equations for the elastic and plastic responses are written in a configuration reached by elastically unloading, without rotation, from the current, or spatial, configuration by the inverse of the elastic stretch, $\mathbf{v}^e$. The elastic portion of deformation is governed by Hooke's law,

$$\boldsymbol{\tau} = \mathbf{C}(\mathbf{r})\mathbf{e}^e \tag{C.1}$$

where the Kirchhoff stress, $\boldsymbol{\tau}$, is related to the elastic strain, $\mathbf{e}^e$. The Kirchhoff stress is related to the Cauchy stress, $\boldsymbol{\sigma}$, by $\boldsymbol{\tau} = \det(\mathbf{v}^e)\boldsymbol{\sigma}$; the elastic strain is computed from the elastic stretch as $\mathbf{e}^e = \mathbf{v}^e - \mathbf{I}$, assuming small elastic strains [17, 86]. The stiffness tensor, $\mathbf{C}$, is dependent on the symmetry of the crystal, and is reduced to reflect said symmetry [84]. Additionally, the stiffness tensor is a function of the orientation of the crystal, represented here using the Rodrigues' vector, $\mathbf{r}$ [43].

The plastic portion of deformation is governed by a rate-dependent restricted slip model. The plastic deformation rate, $\mathbf{D}^P$ (defined again in unloaded configuration), is a linear combination of the simple shearing modes defined by the symmetric portion of the Schmid tensors,

$$\mathbf{D}^P = \sum_k \dot{\gamma}^k \mathbf{P}^k \tag{C.2}$$

$$\mathbf{P}^k = \mathrm{sym}\left(\mathbf{s}^k \otimes \mathbf{m}^k\right) \tag{C.3}$$

where $\dot{\gamma}$ is the shearing rate. For each slip system, k, the Schmid tensor is defined as the dyadic product between a slip plane normal vector, $\mathbf{m}^k$, and a slip direction vector, $\mathbf{s}^k$. Additionally, the plastic deformation rate tensor may be reduced to a scalar value, or the effective plastic deformation rate:

$$D^P_{eff} = \sqrt{\frac{2}{3}\mathbf{D}^P : \mathbf{D}^P} \tag{C.4}$$

Slip systems used in this study are shown in Table C.2. The α phase utilizes three

slip families in order to produce a sufficient number of independent slip systems to accommodate generalized plasticity.

Phase	Crystal Type	Slip System Name	Number of Systems	m	s
α	HCP	Basal (b)	3	$\{0\,0\,0\,1\}$	$\langle 1\,1\,\bar{2}\,0\rangle$
α	HCP	Prismatic (p)	3	$\{0\,0\,\bar{1}\,0\}$	$\langle 1\,1\,\bar{2}\,0\rangle$
α	HCP	Pyramidal (π)	12	$\{0\,0\,\bar{1}\,1\}$	$\langle 1\,1\,\bar{2}\,3\rangle$
β	BCC	-	12	$\{1\,1\,0\}$	$\langle 1\,1\,1\rangle$

Table C.2: Slip systems used for α and β crystallographic phases.

The kinetics of slip are defined using a power law relationship between the shearing rate of a given slip system and the resolved shear stress, τ^k, on that system:

$$\begin{aligned} \dot{\gamma}^k &= \dot{\gamma}_0 \left(\frac{|\tau^k|}{g^k} \right)^{\frac{1}{m}} \operatorname{sgn}(\tau^k) \\ \text{where } \tau^k &= \operatorname{tr}(\mathbf{P}^k \boldsymbol{\tau}') \end{aligned} \tag{C.5}$$

where $\boldsymbol{\tau}'$ is the deviatoric portion of $\boldsymbol{\tau}$. The resolved shear stress on a slip system is scaled by the slip system strength, g^k. The fixed-state strain rate sensitivity is controlled by m, and $\dot{\gamma}_0^k$ is the fixed-state strain rate scaling coefficient. For a given element, g^k is the same for all slip systems within a family.

Similarly, for a given element, each slip system within a family will evolve at the same rate. Evolution of a slip system's strength is modeled using a linear Voce type expression [65], while the saturation strength is a function of the sum of the slip system shear rates for a given element:

$$\begin{aligned} \dot{g}^k &= \dot{\gamma} h_0 \left(\frac{g_s^k(\dot{\gamma}) - g^k}{g_s^k(\dot{\gamma}) - g_0^k} \right) \\ \text{where } g_s^k(\dot{\gamma}) &= g_{s0}^k \left(\frac{\dot{\gamma}}{\dot{\gamma}_{s0}} \right)^{m'} \text{ and } \dot{\gamma} = \sum_k |\dot{\gamma}^k| \end{aligned} \tag{C.6}$$

The initial slip system strength and saturation strength are defined by g_0^k and g_s^k, respectively, and h_0 is the strength hardening rate coefficient. The saturation strength is a

function of the sum of the slip system shear rates for a given element, and is controlled by the initial saturation strength, g^k_{s0}, the saturation strength strain rate scaling coefficient, $\dot{\gamma}_{s0}$, and the saturation strength rate scaling exponent, m'. For a given element, the saturation strengths of all slip systems within a family will evolve at the same rate.

Model parameters were gathered from associated studies and literature. Single crystal elastic constants are outlined in Table C.3. Single crystal elastic constants for the α phase were optimized in an associated study, utilizing a method based on minimizing the differences in discrete spherical harmonic modes of the lattice strain pole figures calculated from high energy X-ray diffraction experiments and from simulations [126]. Single crystal elastic constants for the β phase were taken from literature [11, 63].

Values used for initial slip system strengths are outlined in Table C.4. Relative initial slip system strengths for the α phase were also identified for our Ti-6Al-4V material using X-ray diffraction data in an associated study [33] and informed the parameters used in this study. The relative values of the strengths of the basal, prismatic and pyramidal slip systems are similar to values reported by others in the literature [56, 18] for Ti-6Al-4V. The basal and prismatic systems are comparable in strength while the pyramidal system is considerably stronger. The β phase initial slip system strength was set equal to the initial slip system strengths of the basal and prismatic systems of the α phase, approximated to reflect current literature [80]. Other model parameters (Table C.5) were chosen to limit the magnitude of hardening and effectively suppress evolution of the saturation strength. Both crystallographic phases are assumed to have the same parameters for the plastic flow kinetics and strain hardening, which were chosen to provide good agreement with the measured tensile behavior.

Phase	C_{11} **(GPa)**	C_{12} **(GPa)**	C_{13} **(GPa)**	C_{44} **(GPa)**
α	169.66	88.66	61.66	42.50
β	133.10	95.10	-	42.70

Table C.3: Single crystal elastic constants for the α phase and β phase.

$g_{0,\beta}$ **(MPa)**	$g_{0,b}$ **(MPa)**	$g_{0,p}$ **(MPa)**	$g_{0,\pi}$ **(MPa)**
390	390	390	663

Table C.4: Initial slip system strengths for the α phase and β phase.

h_0 **(MPa)**	g_s **(MPa)**	m	m'	$\dot{\gamma}_0$ **(s^{-1})**	$\dot{\gamma}_s$ **(s^{-1})**
190	530	0.01	0.01	1.0	5×10^{10}

Table C.5: Plasticity parameters used for both the α phase and β phase.

C.3 Microstructure Instantiation

C.3.1 Geometric Instantiation

The characterization of the β annealed microstructure discussed in Section C.2.1 provides a map of the prior β phase grain structure from which the α phase colonies emerge upon cooling of the material. Instantiation of polycrystals for use in simulations will build on that knowledge, starting from prior β phase grains, forming α phase colonies within grains, and finally β phase lamella within α phase colonies.

Multilevel Tessellation Method

Following this approach, a microstructure was generated by applying several levels of tessellations (i.e., a multilevel tessellation method). Tessellations were generated in a similar way at all levels by partitioning a domain of space, D, into cells. At the first level, D corresponds to the body of the full polycrystal, while at subsequent levels, D corresponds to each of the cells of the tessellations of the previous level. Tessellations

described henceforth are either Laguerre tessellations or lamellar tessellations.

A Laguerre tessellation of a domain of space is constructed from a spatial distribution of seed points, S_i ($i \in [1, N]$), of non-negative weights, w_i. A cell, C_i, is associated with each seed point in the following manner:

$$C_i = \left\{ P(\mathbf{x}) \in D \mid \|P - S_i\|^2 - w_i < \|P - S_j\|^2 - w_j \ \forall j \neq i \right\} \tag{C.7}$$

The resulting cells are convex polyhedra intersecting along planar faces, straight edges and vertices. The larger the weight of a seed (relative to the weights of other seeds), the bigger its associated cell. The actual size and shape of a cell, however, depend on the full set of seed positions and weights. A common way to define the positions and weights of the seeds is by sphere packing [42]. In this case, Laguerre tessellations are generated by evolving the seed positions and weights until desired (target) cell properties are obtained. In other words, Laguerre tessellations are obtained through the minimization of an objective function that quantifies the difference between the current cell properties and the target cell properties, and whose variables are the seed attributes.

It is possible to parametrize the cell size as the diameter of the sphere of equivalent volume, d, and the cell shape as the sphericity, s, which is equal to the ratio of the surface area of the sphere of equivalent volume to the surface area of the cell. The normalized diameter of a cell, d_n, is defined as $d/\langle d \rangle$, where '$\langle\ \rangle$' denotes the average over all cells. Let the target cumulative distribution functions of the normalized diameters and sphericities be written as F_{d_n} and F_s, and their current counterparts be written as $F^*_{d_n}$ and F^*_s, respectively. The differences between the target and current distributions can be calculated in the same way for both variables and contribute equally to the objective function:

$$O = \int_{-\infty}^{+\infty} \frac{\left(F^*_{d_n}(x) \circ S - F_{d_n}(x) \circ S\right)^2}{F_{d_n}(x) \circ S \ \left(1 - F_{d_n}(x) \circ S\right)} \mathrm{d}x + \int_{-\infty}^{+\infty} \frac{\left(F^*_s(x) \circ S - F_s(x) \circ S\right)^2}{F_s(x) \circ S \ \left(1 - F_s(x) \circ S\right)} \mathrm{d}x \tag{C.8}$$

where $\circ$ is the convolution product, and S is a normal distribution of relatively small standard deviation (0.05) - introduced to facilitate optimization convergence. O takes a minimum value of zero when the current and target distributions are equal. This problem is solved using a gradient-free, non-linear optimization algorithm [55], by considering random seed positions and equal seed weights as as initial solution (which corresponds to a Voronoi tessellation).

A lamellar tessellation is generated by periodically slicing a domain with parallel planes. The width of the resulting lamellae is controlled by the plane positions and can be constant or not throughout the domain.

Both Laguerre tessellations and lamellar tessellations can be used to generate multi-level tessellations. At the first level, a tessellation is generated to produce primary cells. At the second level, each primary cell is divided into a new tessellation to produce secondary cells. This process can be repeated an arbitrary number of times until the desired microstructural representation is reached. The construction of a multilevel tessellation results in a collection of adjacent tessellations at the last level, which intersect along planar faces, straight edges and vertices of upper-level tessellations (this can be seen on Figure C.5 which details a multilevel tessellation for the case of the β annealed alloy). All the tessellation faces, edges and vertices that overlap at these intersections are eventually merged, and the resulting geometry is then subjected to regularization and meshing [93]. These methods are implemented in the Neper software package [92].

Application to β Annealed Microstructure

Data collected from the near field diffraction experiments (Figure C.3) were used as a starting point for informing the geometry of virtual microstructures. Distributions of

grain size and sphericity are well established for grain-growth microstructures [101, 112]. A Laguerre tessellation was used to represent the large, equiaxed prior β phase grains. To facilitate the parametric study, the size distribution was altered from the grain-growth size distribution, such that it resulted in more uniform grain sizes. Figure C.4 details the distributions describing the tessellation. The domain shape (rectangular prism) and aspect ratio (4:1) were chosen in order to mimic the gauge section of a physical specimen (Figure C.5(a)).

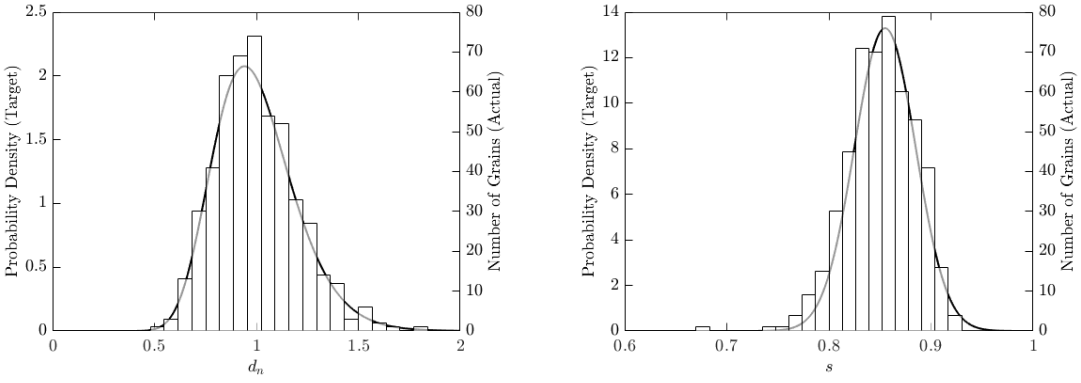

(a) (b)

Figure C.4: Target distributions (solid lines) and actual distributions (histograms) for (a) normalized equivalent diameter (d_n) of the grains, and (b) sphericity (s) of the grains. The distribution of the equivalent diameter of the grains is represented by a log-normal distribution with a mean of 1 and a standard deviation of 0.2, while the distribution of sphericity of the grains is represented by a normal distribution with a mean of 0.855 and a standard deviation of 0.03. An example tessellation with 500 grains was used for the actual distributions.

To represent the α phase colonies that transform within each prior β phase grain, a second level tessellation was invoked. Using each prior β phase grain as a domain, a Laguerre tessellation was performed where each new cell represents a colony (Figure C.5(b)). Similar sphericity and size parameters as the first level tessellation were used for each second level tessellation. By using the prior β phase grains as domains in which the α phase colonies form, α phase structures form the shape of a prior β phase grain,

and localized microtexturing is ensured when orientations are assigned.

Finally, remnant β phase lamellae were represented using a third level of tessellation (Figure C.5(c)). As lamellar width was able to be altered, volume fractions of crystallographic phases were controlled by fixing the width of the β lamellae and altering the width of the α phase in between lamellae. It has been observed that the flat portions of the lamellar planes are parallel to the $(\bar{1}\,1\,0\,0)$ plane of the α phase, or equivalently to the $(\bar{1}\,1\,2)$ plane of the β phase [75], in agreement with the Burgers orientation relationship between the α and β phases (see Section C.3.2). As such the lamellae were defined accordingly by relating the lamellar plane normals to either the grain or colony crystallographic orientation. Successive tessellation levels are concatenated to form the full geometric instantiation (Figure C.5(d)).

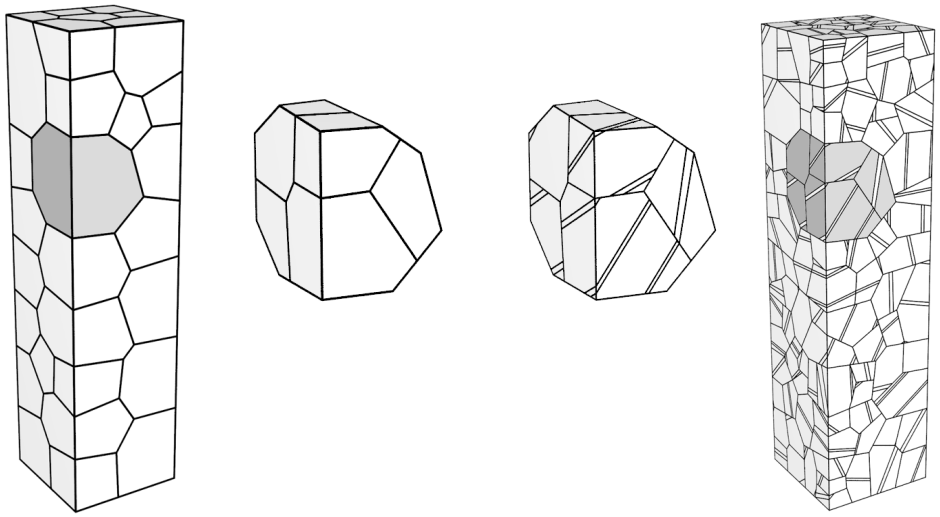

Figure C.5: Example trilevel tessellation. (a) First level Laguerre tessellation in primary domain with example cell highlighted, (b) second level Laguerre tessellation using example first level Laguerre cell as domain (enlarged), (c) second level Laguerre cells discretized into lamellar planes (enlarged), (d) primary domain including all tessellation levels with example cell highlighted.

C.3.2 Orientation Selection

Orientations were selected with strict attention paid to localized microtexturing. While an experimental orientation distribution function could potentially be built from measured α phase orientations, such as those in Figure C.3(a), random sampling from such a function would effectively eliminate localized microtexturing. As such, it is necessary to start from the pre-transformation structure and select orientations that would preserve this phenomenon. Ideally, an orientation distribution function for the reconstructed prior β phase grains would be gathered experimentally. Presently, near field high energy X-ray diffraction experiments necessitate the use of small samples due to limitations in both time and current technological capabilities. As Figure C.3(b) illustrates, the diffraction volume used captured only a small number of prior β phase grains, far fewer than would be necessary to create a statistically significant orientation distribution function. Since the β annealed microstructure was rolled and recrystallized above the transus temperature when it was composed entirely of cubic crystals, a Cube texture was assumed [62, 133]. As such, an idealized orientation distribution function was generated using a spherical Gaussian-type distribution centered around the origin of Rodrigues' orientation space [43, 70], and is normalized over the cubic fundamental region, Ω,

$$\begin{aligned} A(\mathbf{r}) &= \frac{1}{(2\pi\eta^2)^{\frac{3}{2}}}\, e^{-\frac{|\mathbf{r}|^2}{\eta^2}} \\ \int_{\Omega} A(\mathbf{r})\mathrm{d}v &= 1 \end{aligned} \tag{C.9}$$

where η controls the strength of texture. To provide a distribution with a reasonably strong texture, a value of $\eta = 0.255$ was chosen, which creates an orientation distribution function with a maximal intensity of ~13 at the Cube orientation. Orientations for the prior β phase grains are generated by randomly sampling from this idealized orientation distribution function, plotted in Figure C.6(a).

The α phase colonies within prior β phase grains have orientations that are strictly coupled to the orientation of the prior β phase grains in which they form, obeying the Burgers orientation relationship:

$$\begin{aligned} \{1\,1\,0\}_\beta &\parallel (0\,0\,0\,1)_\alpha \\ [1\,1\,1]_\beta &\parallel [1\,1\,\bar{2}\,0]_\alpha \end{aligned} \tag{C.10}$$

For a given β phase orientation, there are twelve possible α phase orientations that may arise as governed by Equation C.10. To assign orientations for the α phase colonies that form within a prior β grain, orientations were chosen at random from the twelve possibilities. In other words, it was assumed that no preference is given to variant selection. Figure C.6(b) illustrates the idealized α phase texture that would arise from 10,000 prior β phase grains transforming into 10,000 random α phase variants. Note the decrease in the strength of texture between the prior β phase and the transformed α phase due to the single β phase texture component being distributed among all the α variants. All calculations and plotting in Rodrigues' orientation space were performed using the ODFPF software package developed by the Deformation Processes Lab at Cornell University [31].

C.4 Simulations and Results

C.4.1 Simulation Suite

A set of simulations was devised to study the effects the geometric features of the microstructure have on the mechanical behavior of the material. Both single phase (α only) and dual phase simulations were conducted, and a full list is detailed in Table C.6. The main geometric features studied were the number of prior β phase grains in a domain,

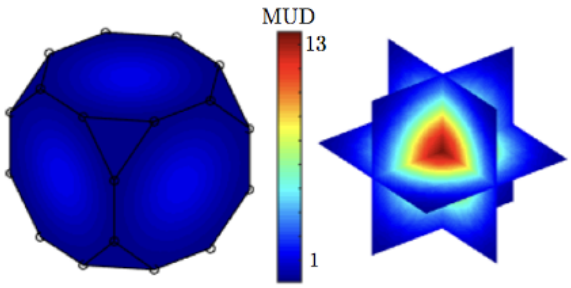

(a)

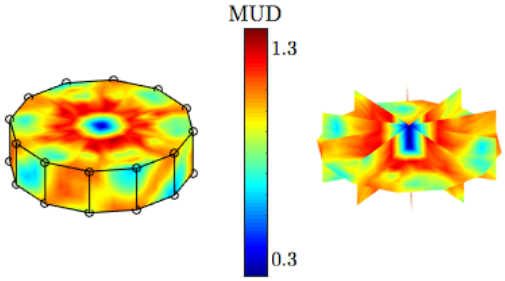

(b)

Figure C.6: (a) Cube texture of prior β phase grains plotted in the cubic symmetry fundamental region of Rodrigues' space, and (b) the resulting α phase texture assuming random variant selection plotted in the hexagonal symmetry fundamental region of Rodrigues' space. Scales presented as multiples of a uniform distribution (MUD).

the number of α phase colonies per grain, and the inclusion and width of remnant β phase lamellae.

Single phase simulations were conducted to probe the effect of the number of grains in a domain, as well as the number of colonies per grain. Ignoring the remnant β phase facilitated the study of the dominant α phase only. Five microstructure geometries with 40, 120, 200, 280, and 360 grains per domain and a single colony per grain were constructed. To provide details on variability for each of these five geometries, five simulations were conducted for each geometry, each time using a distinct orientation set. Similarly, five microstructure geometries with 40 grains and 5, 10, 15, 20, and 25 colonies

per grain were produced. Again, five simulations were conducted for each geometry using distinct orientation sets for each simulation. Example geometries for single phase instantiations can be seen in Figures C.7 and C.8.

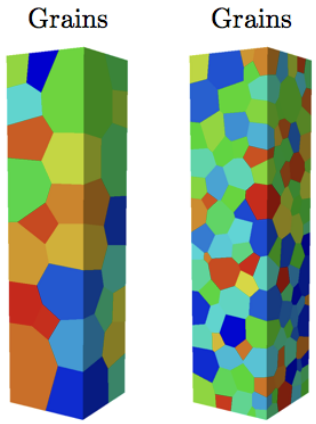

Figure C.7: Examples of single phase geometries containing (a) 40 grains, and (b) 360 grains. Grains are colored arbitrarily.

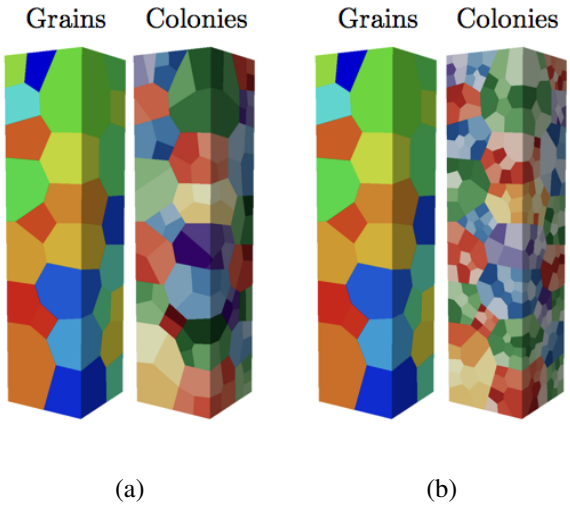

Figure C.8: Examples of single phase geometries containing 40 grains with (a) 5 colonies per grain and (b) 25 colonies per grain. Grains are colored arbitrarily, while colonies are colored on monochromatic scales dependent on the grain in which they reside.

Investigating the inclusion of the β phase in the simulations consisted mainly of

studying the effects of the lamellae - in terms of their inclusion, size, and crystallographic orientation. While the simulation method described in Section C.2.2 does not include an inherent length scale, the local stress field calculated using this method is influenced by the morphology of the microstructure and distribution of phases. As such, it is important to probe the effects of lamellar width on the local stress field, and in turn the macroscopic response. For each dual phase instantiation, volume fraction of the β phase was fixed at 8% ± 1%. In investigating the effect of the size of the remnant β phase lamellae, five base microstructure geometries were produced with 40 grains and a single colony per grain, and five base geometries were produced with 40 grains and five colonies per grain. Since the planar direction of the remnant β phase lamella is dependent on the orientation set, each time a new orientation set was applied to a base geometry, the lamella would change. Each base geometry was used with five different orientation sets, and five lamellar widths (0.10, 0.08, 0.06, 0.04, and 0.02) resulting in 50 geometric instantiations. In these simulations, a decrease in lamellar width leads to an increasing number of lamellae per grain in order to enforce phase volume fraction - which could also produce changes to the local stress field. Example geometries for dual phase instantiations containing lamella can be seen in Figure C.9.

Five geometries were produced with 40 grains, 5, 10, 15, 20, and 25 colonies per grain, and a constant lamellar width of 0.10. This set of geometries was simulated twice to gauge the effects of localized microtexturing on dual phase simulations. Each geometry was simulated once with orientations assigned such that the Burgers orientation relationship was properly enforced and once with the same orientation set assigned randomly to the geometry. Four Voronoi microstructures were produced with 500, 1000, 1500, and 3000 grains, where random grains were assigned as β phase to probe the effect of both the remnant β phase's morphology (morphology consisted of no inter-grain colonies, nor association between plane normals and crystallographic direction), and

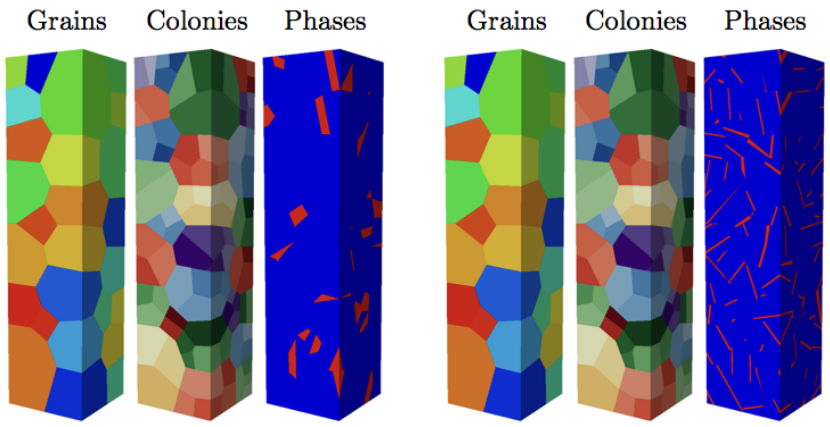

(a) (b)

Figure C.9: Examples of dual phase geometries containing 40 grains, 5 colonies per grain, and (a) lamella of width 0.10 and (b) lamella of width 0.02. Grains are colored arbitrarily, while colonies are colored on monochromatic scales dependent on the grain in which they reside. Phase is colored using a binary color scale, where blue represents regions of α phase, and red represents regions of β phase.

thus localized microtexturing. Example geometries for dual phase Voronoi instantiations can be seen in Figure C.10.

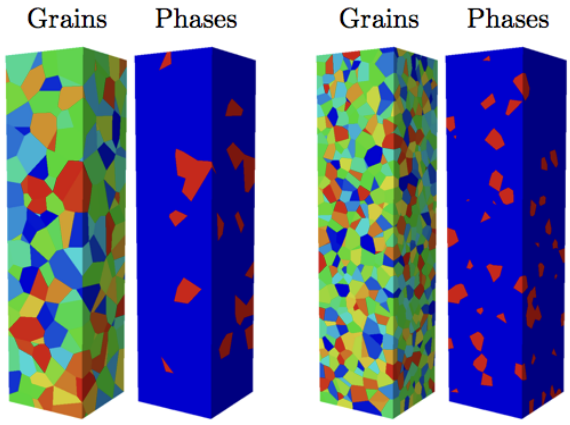

(a) (b)

Figure C.10: Examples of dual phase Voronoi geometries with (a) 500 total grains and (b) 3000 total grains. Phase is colored using a binary color scale, where blue represents regions of α phase, and red represents regions of β phase.

Grains	Colonies/Grain	Lamellar Width	Phases
40, 120, 200, 280, 360	1	-	α
40	5, 10, 15, 20, 25	-	α
40	1	0.10, 0.08, 0.06, 0.04, 0.02	$\alpha + \beta$
40	5	0.10, 0.08, 0.06, 0.04, 0.02	$\alpha + \beta$
40	5, 10, 15, 20, 25	0.10	$\alpha + \beta$
500, 1000, 1500, 3000	1	-	$\alpha + \beta$

Table C.6: List of simulations conducted for the β annealed microstructure. Each geometry is simulated with 5 separate orientation sets. For the dual phase ($\alpha + \beta$) cases with a variable number of colonies per grain, instantiations were simulated twice - once enforcing the Burgers orientation relationship and once not.

To describe the number of grains in a cross section of a sample, a metric λ is introduced, which is a ratio of the specimen's thickness to the average equivalent diameter (Section C.3.1) of the specimen's grains [53]. Table C.7 lists the calculated λ values for the base geometries. As the total number of cells of distinct orientation are increased, the value of λ increases (since the equivalent diameter of the grains must necessarily decrease). Previous studies suggest that an increase in the yield strength of a material is associated with an increase in λ - specifically when $1 < \lambda < 3$ [53].

Grains	Colonies/Grain	λ
40, 120, 200, 280, 360	1	1.81, 2.67, 3.13, 3.62, 3.96
40	5, 10, 15, 20, 25	3.14, 3.92, 4.43, 5.12, 6.27
500, 1000, 1500, 3000	1	3.99, 5.18, 6.33, 8.86

Table C.7: Average equivalent area ratio for different morphologies. Dual phase instantiations utilize the single phase geometries as base geometries, and as such have the same average equivalent area ratios.

C.4.2 Instantiation and Data Reduction

To showcase the steps from the formation of a virtual microstructure to the reduction of simulated data, a generic sample is shown. A geometric morphology is created for a sample (Section C.3.1), during which orientations and phases are necessarily assigned -

lamellae normals are needed for instantiation, and are known from the crystallographic orientations. Figure C.11 shows an example orientation map and phase map for a dual phase complex morphology.

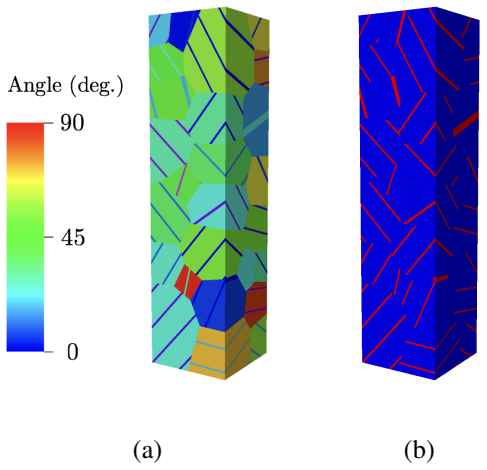

Figure C.11: Example sample with 40 grains, 1 colony per grain, and a lamellar width of 0.02, colored by (a) crystallographic orientation - specifically the deviation of the crystal {0 0 1} direction from the sample's loading direction, and (b) crystallographic phase (binary color scale where blue represents regions of α phase, and red represents regions of β phase).

Data output from the deformation simulation is used to construct a sample stress strain curve - an example is shown in Figure C.12. From this curve, the yield stress and ductility is calculated. Furthermore, data output from the simulations may be plotted against on the deformed geometry (Figure C.13) to gain information about the progression of plasticity spatially. Information about the average mesh and simulation statistics can be viewed in Table C.8. Below, aggregate and representative results deduced in this manner from each simulation are presented.

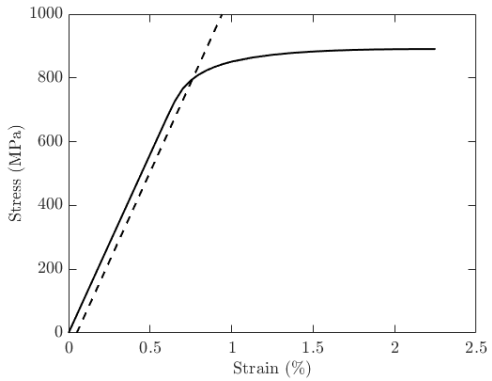

Figure C.12: Example stress strain curve plotted to the ductility limit, with offset yield line (dashed).

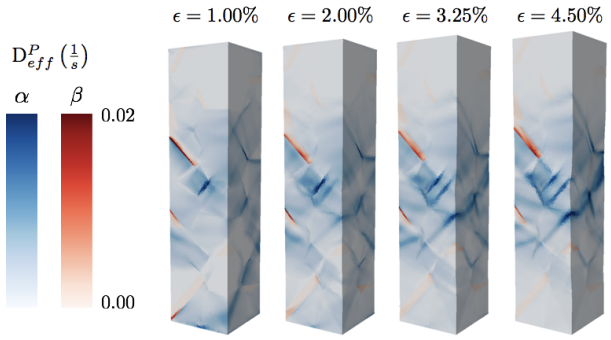

Figure C.13: Example variable (effective plastic deformation rate) plotted spatially on a deformed mesh at various strains.

Phases	**NxPPN**	**Nodal Points**	**Duration**
α	8x8	160,000	4
$\alpha + \beta$ (thick lamella)	16x8	1,250,000	28
$\alpha + \beta$ (thin lamella)	32x8	2,800,000	42

Table C.8: Selected statistics for main simulation sets. Computer architecture is described by the number of computational nodes (N) and the number of processors per node (PPN). Mesh size is described by the average number of nodal points, rounded to the nearest 10,000. Duration describes the average completion time, rounded to the nearest hour. Thick lamella refers to simulations with lamellar widths of 0.10, 0.08, 0.06, or 0.04, whereas thin lamella refers to simulations with lamellar width of 0.02.

C.4.3 Simulation Result Trends

For each simulation, the engineering strain was calculated from the initial sample length, total time at each load step, and velocity applied to the control surface. The engineering stress was calculated from the integrated load on the extended surface at each time step and the initial cross sectional area. A stress-strain history was calculated for each sample. Yield strength was calculated using a 0.1% offset method, and ductility was defined as the strain correlating to the maximum engineering stress - both matching the same methods used in the tensile experiments (Section C.2.1).

Yield Strength Trends

Evolution of the yield strength as a function of geometric properties of the β annealed microstructure are plotted here. Figure C.14 shows yield strength trends for simulations conducted only with the α phase. Error bars represent variability in the data, calculated as the standard deviation for each data set. Figures C.15 and C.16 show the yield strength trends for the sets of dual phase simulations. Since multiple sets of simulations were not performed for the dual phase instantiations, no measure of variability is included.

Ductility and Hardening Trends

Figures C.17 through C.19 detail ductility and hardening trends in a similar fashion to the yield strength trends presented in Section C.4.3.

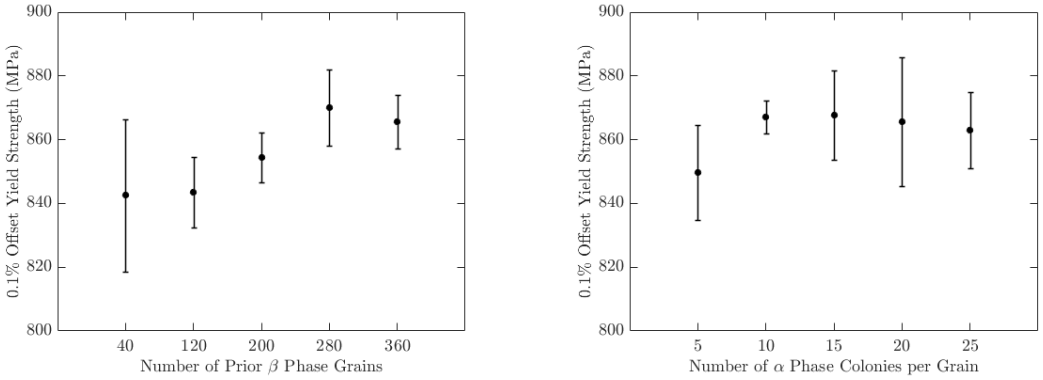

(a) (b)

Figure C.14: Yield strength trends of single phase simulations for changes in the (a) number of prior β phase grains, and the (b) number of α phase colonies per grain (40 grains).

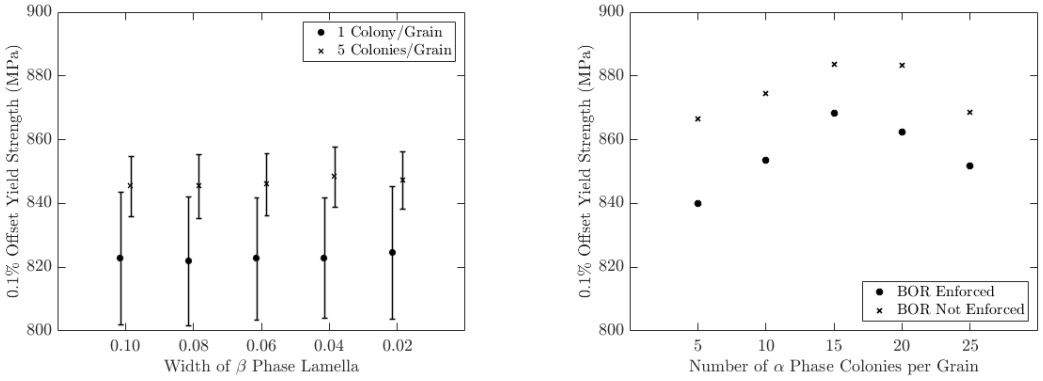

(a) (b)

Figure C.15: Yield strength trends for changes in the (a) width of remnant β phase lamellae, and the (b) number of α phase colonies per grain with a constant lamellar thickness of w = 0.10. In (b), results are provided where the Burgers orientation relationship (BOR) was enforced or not.

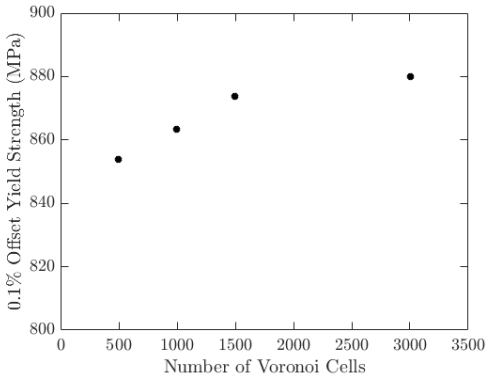

Figure C.16: Yield strength trends for changes in the number of Voronoi cells in dual phase single level Voronoi tessellations. The number of Voronoi cells refers to the sum of both prior β phase grains that have fully transformed to a single α variant, as well as grains composed solely of β phase.

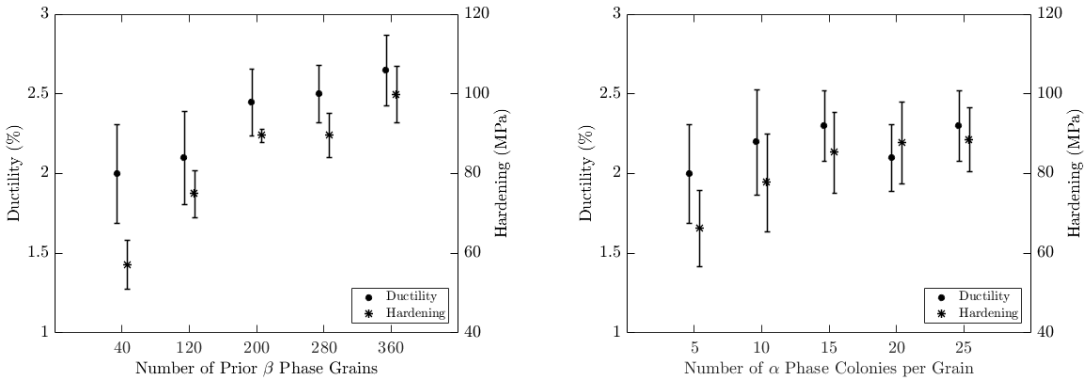

(a) (b)

Figure C.17: Ductility and hardening trends of single phase simulations for changes in the (a) number of prior β phase grains, and the (b) number of α phase colonies per grain (40 grains).

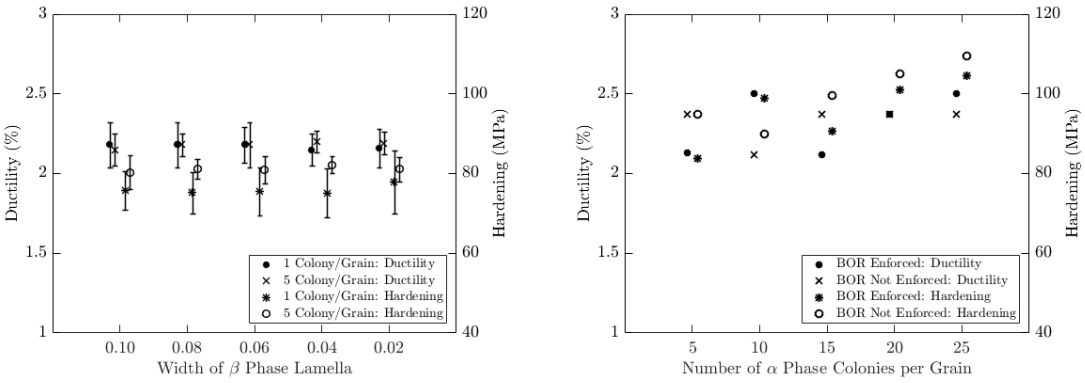

(a) (b)

Figure C.18: Ductility and hardening trends for changes in the (a) width of remnant β phase lamellae, and the (b) number of α phase colonies per grain with a constant lamellar thickness of w = 0.10. In (b), results are provided where the Burgers orientation relationship (BOR) was enforced or not.

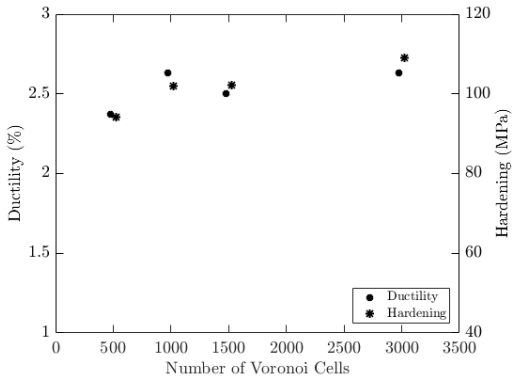

Figure C.19: Ductility and hardening trends for changes in the number of grains in dual phase single level Voronoi tessellations. The number of Voronoi cells refers to the sum of both prior β phase grains that have fully transformed to a single α variant, as well as grains composed solely of β phase.

C.5 Discussion

C.5.1 Yield Strength Trends

For the single phase simulations, a strong positive correlation is seen between the number of prior β phase grains and the offset yield strength (Figure C.14(a)). Yield strength trends for increases in the number of grains correlate well with an increase in the specimen's λ value found in Table C.7. Moreover, the yield strength is most variable when the number of grains is at its least. Looking at the yield strength as a function of the number of α phase colonies per grain reveals that the yield strength increases but saturates as the number of colonies per grain increases (though λ increases as the number of colonies per grain increases). This is most likely attributed to the fact that there are only twelve α variants that can form for a given β phase orientation, and as the number of colonies per grain is increased, the likelihood of new orientations being introduced in that domain decreases. Put simply, the yield strength saturates around ten α phase colonies per prior β phase grain due to a saturation in localized texture.

For changes in the lamellar width, virtually no change in yield strength is observed (Figure C.15(a)). Both simulation sets agree in this regard, though the simulations with 5 colonies per grain exhibit higher yield strengths than those with one, echoing the results of the single phase simulations. Inclusion of the remnant β phase lowered the yield strength for both sets of simulations, though all values fell within the lower bound of the calculated variability for the single phase simulations. Figure C.15(b) details yield strength trends for dual phase simulations where the number of colonies is variable - both with and without enforcement of localized microtexturing. For each simulation, when the Burgers orientation relationship was not enforced, the yield strength was higher, and by similar margins for each instantiation. Until 15 colonies per grain,

an increase in the number of colonies per grain corresponds to an increase in the yield strength, after which a negative correlation is observed. Since only one simulation was run for each geometry, however, it is difficult to gauge overall trends.

For dual phase simulations conducted with Voronoi morphologies, the yield strength tends to be higher than dual phase simulations with a complex morphology (Figure C.16). Additionally, it is evident that saturation occurs both at a higher level (~880 MPa) and with more cells of distinct orientation (~1500 cells) than the other dual phase simulations where the Burgers orientation relationship was enforced. These simulations consistently saturate at lower levels (maximum ~860 MPa) and at a lower number of cells (~400 cells, ignoring β lamellae). These values are both driven by the low number of grains used in the sample. However, the simulation set conducted with complex morphologies, but without the enforcement of localized microtexturing, was able to attain yield strengths comparable to those from the Voronoi morphologies (maximum $\geq$880 MPa).

C.5.2 Ductility and Hardening Trends

The calculated ductility exhibits many of the same trends as those for the calculated yield strengths. Single phase simulations exhibit the same positive trends - that is, as the number of grains is increased, the ductility increases (Figure C.17(a)). Similarly, ductility increases as the number of colonies per grain is increased - though again, only marginally as the likelihood of distinct orientations decreases (Figure C.17(b)). Qualitatively, these trends may be understood by inspecting the spatial distribution plastic deformation rate. Figures C.20 and C.21 detail representative results from the extreme cases of the single phase simulations by plotting the effective plastic deformation rate

over the deformed virtual samples.

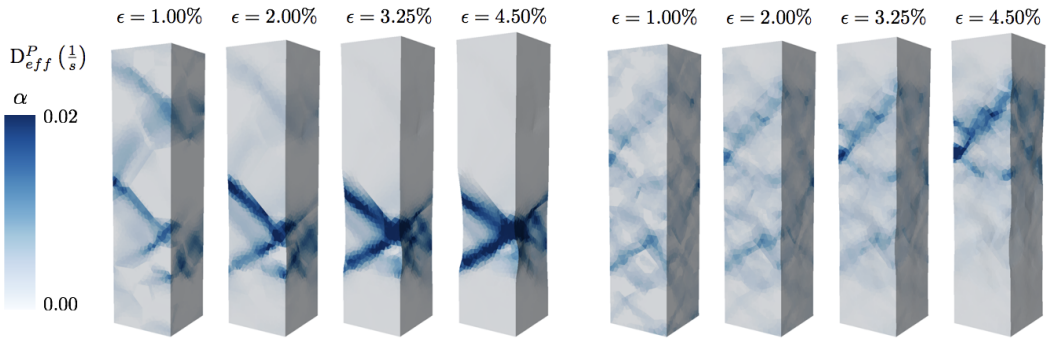

(a) (b)

Figure C.20: Representative results of the effective plastic deformation rate plotted at strains of $\epsilon = 1.00\%$, $\epsilon = 2.00\%$, $\epsilon = 3.25\%$, and $\epsilon = 4.50\%$ for (a) 40 grains and (b) 360 grains.

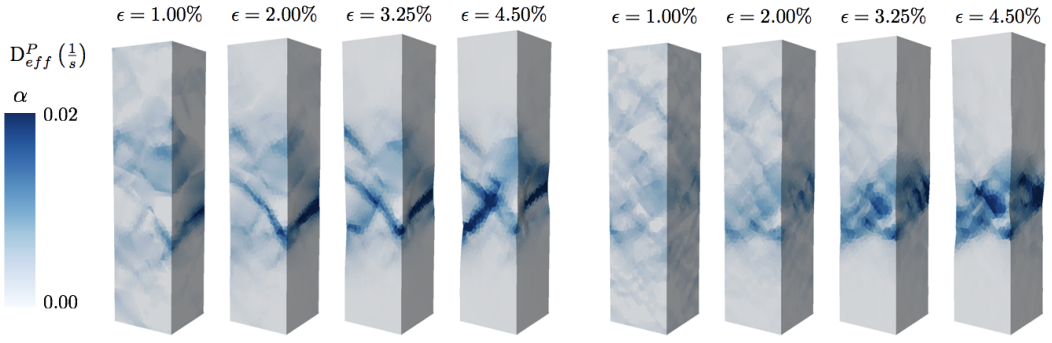

(a) (b)

Figure C.21: Representative results of the effective plastic deformation rate plotted at strains of $\epsilon = 1.00\%$, $\epsilon = 2.00\%$, $\epsilon = 3.25\%$, and $\epsilon = 4.50\%$ for 40 prior β phase grains with (a) 5 colonies and (b) 25 colonies per grain.

As a region of plastically coalesces at a defined region spanning the cross section, the sample is no longer able to carry additional load. The formation of this yield band - or a region of localized plastic deformation - coincides with the ductility of a sample. Figure C.20 showcases two deformation rate plots representing typical deformation characters for the limiting cases of grain variability. Deformation in the case with 40 grains localizes at a lower strain than in the case with 360 grains, reflecting the calculated ductility

values. Similarly, Figure C.21 shows similar plots for representative cases with 5 and 25 colonies per grain (40 grains). Deformation shows similar amounts of localization at the presented strains for both cases, again agreeing with the calculated ductility values. No strong trends in variability are apparent for either of the single phase simulation sets.

Adjusting the lamellar width for a sample has little to no effect on the ductility of the sample (Figure C.18(a)). For both the cases with a single colony per grain, and the cases with 5 colonies per grain, the ductility remains effectively constant as lamellar width is changed. Figures C.22 and C.23 detail the spatial distribution of plastic deformation for the limiting cases of both simulation sets. For the cases with a single colony per grain, the distributions of plastic deformation rate are extremely similar for both simulations. For the cases with 5 colonies per grain, the distribution and intensities are nearly identical. Both of these qualitatively agree with the numerical values of the calculated ductilities. Changing the thickness of the lamellae does not alter the ductility of the sample, as evident by the weak effect it has on plasticity localization.

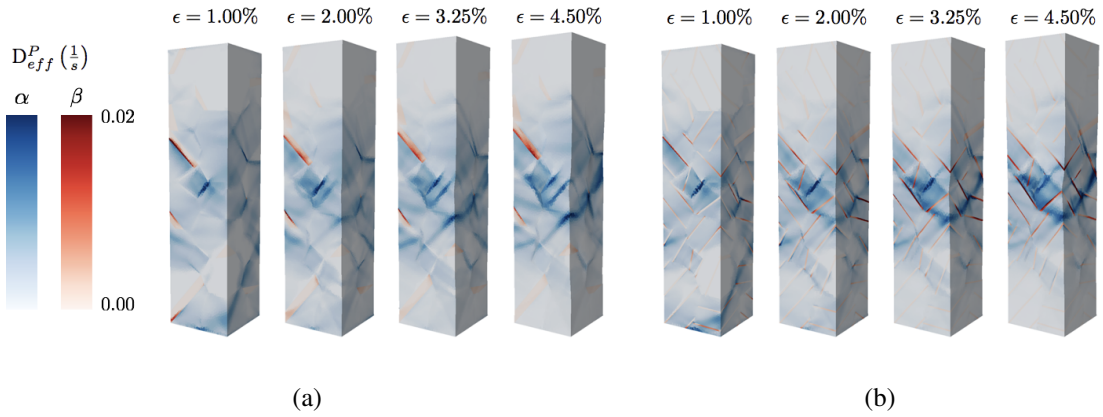

Figure C.22: Representative results of the effective plastic deformation rate plotted at strains of ϵ = 1.00%, ϵ = 2.00%, ϵ = 3.25%, and ϵ = 4.50% for 40 prior β phase grains, 1 α phase colony per grain, and lamellar widths of (a) w = 0.10, and (b) w = 0.02. Scales are identical for the two sets of plots.

For the rest of the dual phase simulations, ductility is relatively constant, or no

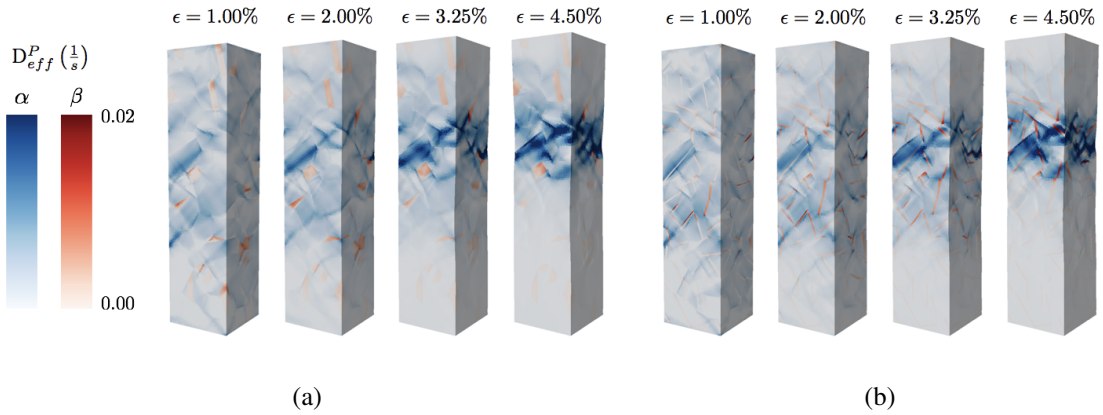

Figure C.23: Representative results of the effective plastic deformation rate plotted at strains of ϵ = 1.00%, ϵ = 2.00%, ϵ = 3.25%, and ϵ = 4.50% for 40 prior β phase grains, 5 α phase colonies per grain, and lamellar widths of (a) w = 0.10, and (b) w = 0.02. Scales are identical for the two sets of plots.

discernible trends are evident. For a complex morphology with a variable number of colonies per grain, a strong saturation is not immediately evident as was in the yield strength. Furthermore, loosening the restriction of the Burgers orientation relationship does not consistently increase or decrease the ductility. Dual phase simulations conducted with a Voronoi morphology, however, tend to have higher ductility values (~2.6%) than their counterparts conducted with complex morphologies and localized microtexturing (maximum ~2.4%) - similar to what is observed in the calculated yield strengths. This, too, may be attributed to the low number of grains present in these virtual samples, as evident by the values calculated from the single phase simulations.

Hardening trends tend to align well with ductility trends. Figures C.17(a) and C.17(b) detail hardening trends for single phase simulations. As the number of grains within a sample is increased, the amount of hardening also increases. Similar to yield and ductility trends, the amount of hardening saturates as the number of colonies per grain is increased past approximately 10 colonies per grain. Hardening in dual phase simulations also follows similar trends as ductility. Changes in lamellar width have lit-

tle effect on hardening (Figure C.18(a)), while enforcement of the Burgers orientation relationship tends to produce lower hardening than in simulations without enforcement (Figure C.18(b)). Dual phase simulations conducted with a Voronoi morphology tend to exhibit more hardening than simulations conducted with complex morphologies.

C.5.3 Effect of Morphology on Slip Activity

The single mode of plastic deformation modeled is crystallographic slip, and thus it is the primary factor controlling the macroscopic yield and ductility of the sample. Inspecting slip activity at different points in the samples' deformation histories lends some insight into the bulk trends described above. Slip activity was probed in each phase independently, and calculated at various points of deformation. Activity for each phase is presented as a volume fraction of that phase with a certain number of slip systems active, calculated element by element. A slip system is considered active if its shear rate is above a threshold value, which here is related to the magnitude of the applied strain rate:

$$\dot{\gamma} \begin{cases} < \frac{1}{10}|\dot{\epsilon}_{app}| & \text{inactive} \\ \geq \frac{1}{10}|\dot{\epsilon}_{app}| & \text{active} \end{cases} \tag{C.11}$$

In all cases presented, results are averaged over the given simulation replications or simulation set so as to provide a representative result. Figure C.24(a) details averaged results for all five simulations with 360 prior β grains. Similarly, Figure C.24(b) displays the average slip activity at various strains for the 25 α colony simulations. Figures C.25 through C.29 detail slip results for all dual phase simulation sets. Averages were calculated using all instantiations per set.

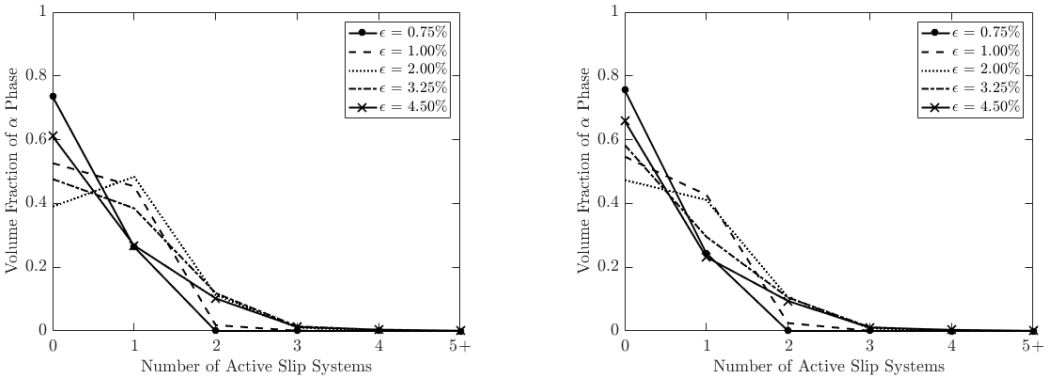

(a) (b)

Figure C.24: Average slip system activity for single phase simulations with (a) 360 prior β phase grains with a single colony per grain, and (b) 40 prior β phase grains with 25 α phase colonies per grain.

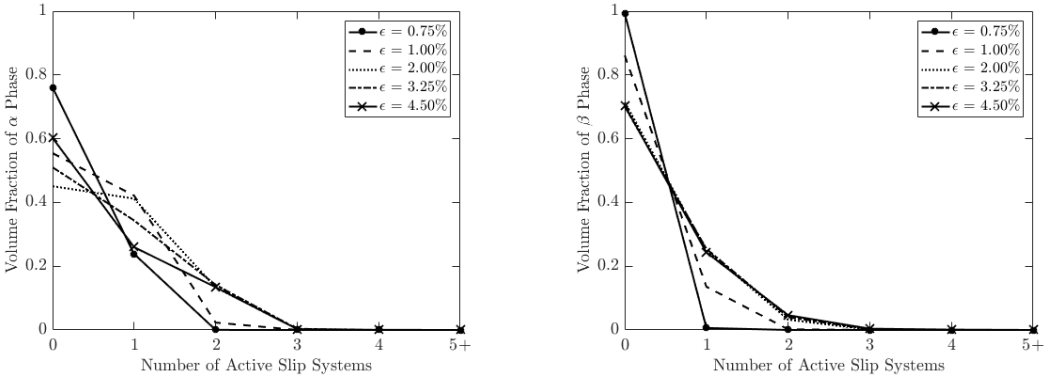

(a) (b)

Figure C.25: Average slip system activity in the (a) α phase and (b) β phase for simulations with 40 prior β phase grains, 1 α phase colony per grain, and variable lamellar thickness.

When comparing only the slip activity in the α phase for both single phase and dual phase simulations, the character of slip is relatively consistent, and some trends are evident. Firstly, polyslip (3 or more slip systems active) was effectively nonexistent, with regions exhibiting it representing at most less than 5% of the sample's α phase volume at any point in deformation. At most, about 60% of the α phase deformed plastically, before deactivating upon plasticity localization. Early in deformation, the overwhelm-

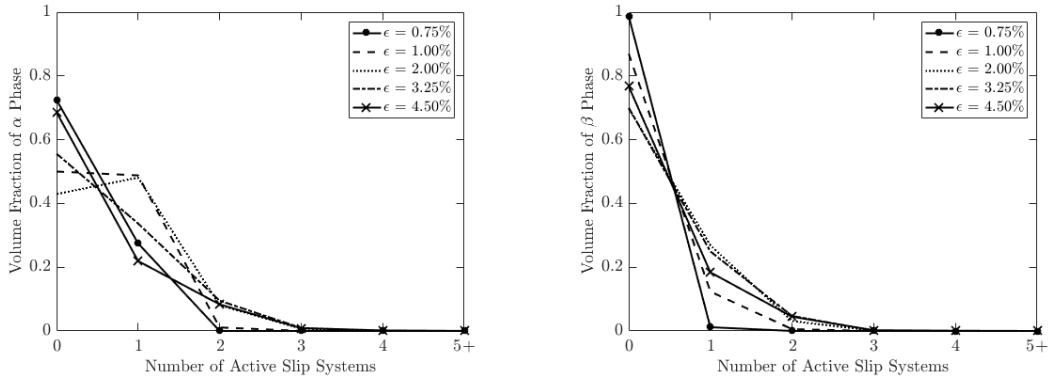

(a) (b)

Figure C.26: Average slip system activity in the (a) α phase and (b) β phase for simulations with 40 prior β phase grains, 5 α phase colonies per grain, and variable lamellar thickness.

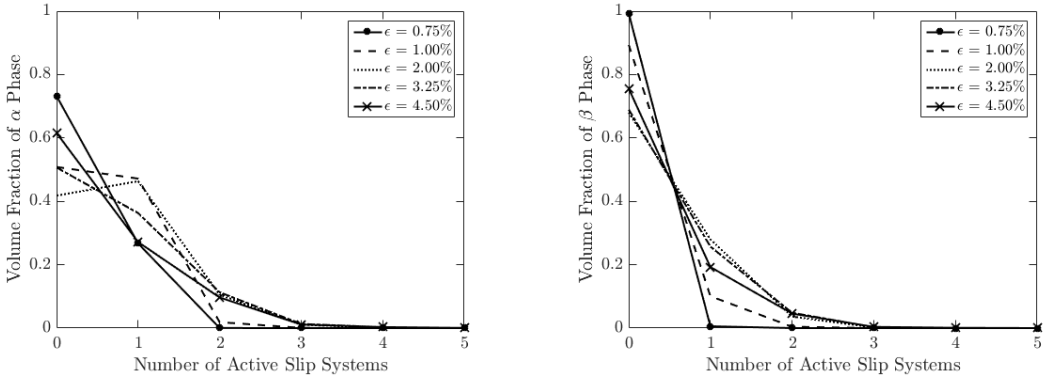

(a) (b)

Figure C.27: Average slip system activity in the (a) α phase and (b) β phase for simulations with 40 prior β phase grains, variable α phase colonies per grain, and lamellae thickness of w = 0.10.

ing majority of the active volume deformed through single slip. Late in deformation, the volume of the regions that deformed by dual slip increased, though even then only to about half of the volume of that exhibiting single slip.

For dual phase simulations with complex morphologies and localized microtexturing, slip in the β phase activated later in deformation than the α phase, and overall activity was lower than that of the α phase (Figures C.25 through C.27). While the α

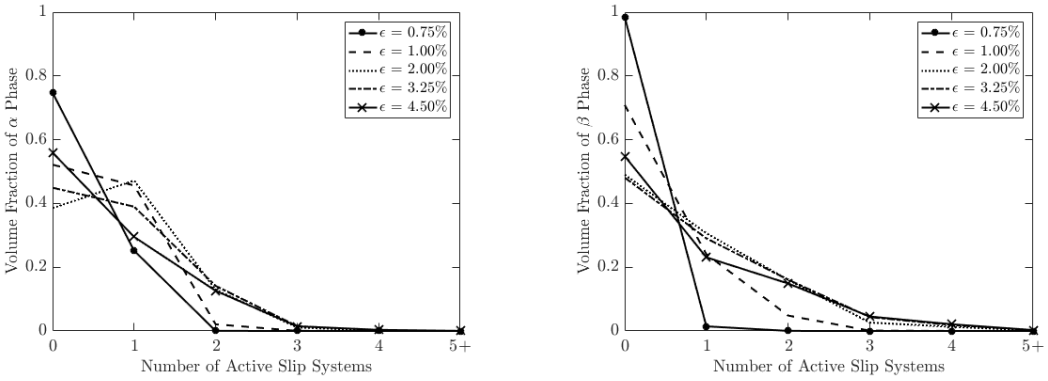

(a) (b)

Figure C.28: Average slip system activity in the (a) α phase and (b) β phase for dual phase Voronoi tessellations.

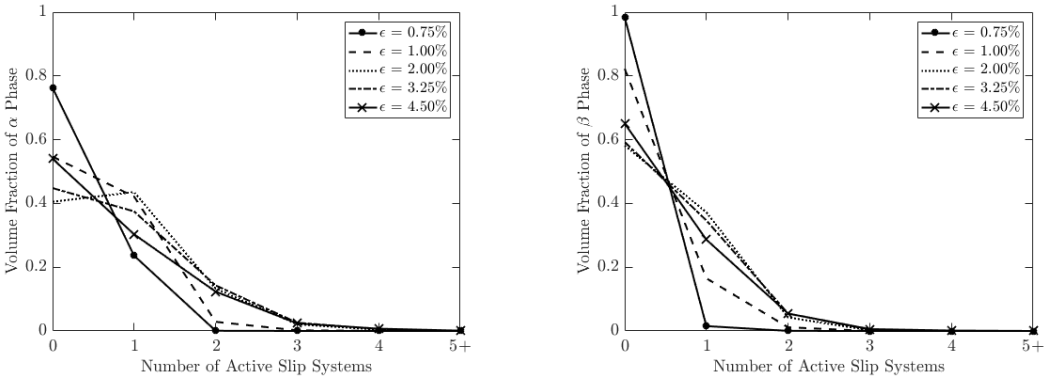

(a) (b)

Figure C.29: Average slip system activity in the (a) α phase and (b) β phase for simulations with 40 prior β phase grains, variable α phase colonies per grain, and a lamellae thickness of w = 0.10, without the enforcement of the Burgers orientation relationship (no localized microtexturing).

phase activated before macroscopic yield ($\epsilon = 0.5\%$), the β phase was found to be entirely elastic at that same point. At peak, only 30% of the β phase was inelastic - half that of the α phase. Further, those β phase regions that were plastically deforming exhibited almost entirely activity of only a single slip system. Again, polyslip was effectively nonexistent.

Dual phase simulations conducted with a Voronoi morphology, however, exhibited β phase slip activity markedly different than that of the previous simulations. While the β phase still activated later than the α phase, as it did in the instantiations with complex morphologies, much more of the β phase volume fraction became active - nearly to the same level as the α phase. At peak, more than 50% of the β phase became plastically active, nearly double what is seen in simulations constructed with complex morphologies. Furthermore, while single slip was the still dominant mode of plastic deformation in the β phase, double slip occurred in a significant volume at each point in deformation, even nearly equalling the volume deforming by single slip later in deformation. Though small, polyslip was non-negligible in the β phase ($\sim$ 15% at its peak), unlike any other simulated slip character for either phase.

Simulations conducted with a complex morphology without localized microtexturing exhibited a slight increase in β phase slip activity (Figure C.29). At peak, more than 40% of the β phase had activated - a 10% increase from the same morphologies with localized microtexturing. This increase in plasticity, however, was nearly entirely single slip - no large increase in double slip or polyslip was witness when localized microtexturing was relaxed. This implies that localized microtexturing and morphological constraints both contribute to restricted slip in the β phase when compared to simulations with a generic morphology.

C.6 Conclusion

A parameter study of the geometric features of β annealed Ti-6Al-4V is presented. Complex representations are instantiated by means of a multilevel tessellation method and include details of the high temperature morphology (prior β phase grains). This method allows for individual parameters controlling the geometry to be altered independently and also allows localized microtexturing to be enforced. The intent is to understand better the role of mechanical constraints introduced by the microstructural geometry on an aggregate's strength and ductility. The simulations demonstrated that:

- The calculated yield strength for a simulation is governed by the number of prior β phase grains in an instantiation, as well as the number of α phase colonies per grain - but with the latter only until the probability of new variants decreased and localized microtexturing became saturated. Inclusion of remnant β phase lamellae tended to decrease the yield strength, but lamellar width had little to no effect.
- The calculated ductility and hardening for a simulation are governed by the same geometric features as the yield strength. The point of ductility was seen to correspond with the formation of a localized band of plastic deformation, which generally formed more readily when there were less cells of distinct orientation through a cross section. Again, lamellar width had little to no effect on the macroscopic ductility or hardening.
- Slip activity in the β phase was restricted in simulations conducted with complex morphologies and localized microtexturing (enforcement of the Burgers orientation relationship), and both morphology and texture are shown to be influential in this phenomenon. Dual phase simulations conducted with generic Voronoi tessellations exhibited higher strength and ductility, and more hardening, than those

conducted with complex morphologies, as well as a high amount of β phase slip activity.

Acknowledgements

Funding for this study was provided by the Office of Naval Research under grant N00014-12-1-0399, as well as the Cornell High Energy Synchrotron Source (CHESS) under NSF award DMR-1332208. Professor Jim Williams is thanked for his expertise and acquisition of necessary materials from TIMET. Dr. Euan Wielewski is thanked for his advice, conducting the tensile experiments in this paper, and sharing data of the near field high energy X-ray diffraction experiment. Donald Boyce is thanked for his work in estimating constitutive model parameters.

BIBLIOGRAPHY

[1] H. Abdolvand, M.R. Daymond, and C. Mareau. Incorporation of twinning into a crystal plasticity finite element model: Evolution of lattice strains and texture in zircaloy-2. *International Journal of Plasticity*, 27(11):1721–1738, nov 2011.

[2] H. Abdolvand, M. Majkut, J. Oddershede, S. Schmidt, U. Lienert, B.J. Diak, P.J. Withers, and M.R. Daymond. On the deformation twinning of Mg AZ31B: A three-dimensional synchrotron X-ray diffraction experiment and crystal plasticity finite element model. *International Journal of Plasticity*, 70:77–97, 2015.

[3] H. Abdolvand, M. Majkut, J. Oddershede, J.P. Wright, and M.R. Daymond. Study of 3-d stress development in parent and twin pairs of a hexagonal close-packed polycrystal: Part II – crystal plasticity finite element modeling. *Acta Materialia*, 93:235–245, 2015.

[4] H. Abdolvand and A.J. Wilkinson. Assessment of residual stress fields at deformation twin tips and the surrounding environments. *Acta Materialia*, 105:219–231, 2016.

[5] A.Ghaderi and M.R. Barnett. Sensitivity of deformation twinning to grain size in titanium and magnesium. *Acta Materialia*, 59(20):7824–7839, 2011.

[6] A. Akhtar. Basal slip and twinning in α-titanium single crystals. *Metallurgical Transactions A*, 6(5):1105–1113, 1975.

[7] M. Ardeljan, I.J. Beyerlein, B.A. McWilliams, and M. Knezevic. Strain rate and temperature sensitive multi-level crystal plasticity model for large plastic deformation behavior: Application to AZ31 magnesium alloy. *International Journal of Plasticity*, 83:90–109, 2016.

[8] R.J. Asaro and A. Needleman. Texture development and strain hardening in rate dependent polycrystals. *Acta Metallurgica*, 33(6):923–953, 1985.

[9] D. Banerjee and J.C. Williams. Perspectives on titanium science and technology. *Acta Materialia*, 61(3):844–879, 2013.

[10] F. Barbe, L. Decker, D. Jeulin, and G. Cailletaud. Intergranular and intragranular behavior of polycrystalline aggregates. Part 1: F.E. model. *International Journal of Plasticity*, 17(4):513–536, 2001.

[11] N.R. Barton and P.R. Dawson. On the spatial arrangement of lattice orientations in hot-rolled multiphase titanium. *Modelling and Simulation in Materials Science and Engineering*, 9(5):433–463, 2001.

[12] N.R. Barton and P.R. Dawson. Lattice misorientations in titanium alloys: modeling the origins of defects. *International Journal of Forming Processes*, 5(2-3-4):189–201, 2002.

[13] Z.S. Basinski, M.S. Szczerba, M. Niewczas, J.D. Embury, and S.J. Basinski. The transformation of slip dislocations during twinning of copper-aluminum alloy crystals. *Revue de Métallurgie*, 94(9):1037–1044, 1997.

[14] I.J. Beyerlein, L. Capolungo, P.E. Marshall, R.J. McCabe, and C.N. Tomé. Statistical analyses of deformation twinning in magnesium. *Philosophical Magazine*, 90(16):2161–2190, may 2010.

[15] Thomas R. Bieler, Leyun Wang, Armand J. Beaudoin, Peter Kenesei, and Ulrich Lienert. In situ characterization of twin nucleation in pure ti using 3d-XRD. *Metallurgical and Materials Transactions A*, 45(1):109–122, 2013.

[16] G.F Bolling and R.H Richman. Continual mechanical twinning. *Acta Metallurgica*, 13(7):709–722, 1965.

[17] A.F. Bower. *Applied Mechanics of Solids*. CRC Press, 2010.

[18] F. Bridier, D.L. McDowell, P. Villechaise, and J. Mendez. Crystal plasticity modeling of slip activity in Ti-6Al-4V under high cycle fatigue loading. *International Journal of Plasticity*, 25(6):1457–1485, 2009.

[19] T.B. Britton, F.P.E Dunne, and A. J. Wilkinson. On the mechanistic basis of deformation at the microscale in hexagonal close-packed metals. *Proceedings of the Royal Society A: Mathematical, Physical and Engineering Science*, 471(2178):20140881, 2015.

[20] T.B. Britton, F.P.E. Dunne, and A.J. Wilkinson. On the mechanistic basis of deformation at the microscale in hexagonal close-packed metals. *Proceedings of the Royal Society A: Mathematical, Physical and Engineering Science*, 471(2178):20140881, 2015.

[21] D.W. Brown, S.R. Agnew, M.A.M. Bourke, T.M. Holden, S.C. Vogel, and C.N. Tomé. Internal strain and texture evolution during deformation twinning in magnesium. *Materials Science and Engineering: A*, 399(1-2):1–12, 2005.

[22] R.W Cahn. Plastic deformation of alpha-uranium: twinning and slip. *Acta Metallurgica*, 1(1):49–70, 1953.

[23] R. Carson, M. Obstalecki, M. Miller, and P. Dawson. Characterizing heterogeneous intragranular deformations in polycrystalline solids using diffraction-based and mechanics-based metrics. *Modelling and Simulation in Materials Science and Engineering*, 25(5):055008, 2017.

[24] G.Y. Chin, W.F. Hosford, and D.R. Mendorf. Accommodation of constrained deformation in f.c.c. metals by slip and twinning. *Proceedings of the Royal Society A: Mathematical, Physical and Engineering Sciences*, 309(1499):433–456, 1969.

[25] S.-H. Choi, D.H. Kim, S.S. Park, and B.S. You. Simulation of stress concentration in mg alloys using the crystal plasticity finite element method. *Acta Materialia*, 58(1):320–329, 2010.

[26] J.W. Christian and S. Mahajan. Deformation twinning. *Progress in Materials Science*, 39(1-2):1–157, 1995.

[27] J.D. Clayton. A continuum description of nonlinear elasticity, slip and twinning, with application to sapphire. *Proceedings of the Royal Society A: Mathematical, Physical and Engineering Sciences*, 465(2101):307–334, 2009.

[28] A.H. Cottrell. *Dislocations and Plastic Flow in Crystals*. Oxford University Press, 1953.

[29] S. Dancette, L. Delannay, K. Renard, M.A. Melchior, and P.J. Jacques. Crystal plasticity modeling of texture development and hardening in TWIP steels. *Acta Materialia*, 60(5):2135–2145, 2012.

[30] Chinmaya R. Dandekar, Yung C. Shin, and John Barnes. Machinability improvement of titanium alloy (ti–6al–4v) via LAM and hybrid machining. *International Journal of Machine Tools and Manufacture*, 50(2):174–182, feb 2010.

[31] P.R. Dawson and D.E. Boyce. OdfPf Library by The Deformation Processes Lab at Cornell University. `https://anisotropy.mae.cornell.edu/onr/Matlab/matlab.html`, 2004.

[32] P.R. Dawson and D.E. Boyce. FEpX – Finite Element Polycrystals: Theory, finite element formulation, numerical implementation and illustrative examples. `arXiv:1504.03296 [cond-mat.mtrl-sci]`, 2015.

[33] P.R. Dawson, D.E. Boyce, J.-S. Park, E. Wielewski, and M.P. Miller. Determining the strengths of HCP slip systems using harmonic analyses of lattice strain distributions. *Acta Materialia*, 144:92–106, 2018.

[34] L. Demkowicz. A Note on Symmetry Boundary Conditions in Finite Element Methods. *Applied Mathematics Letters*, 4(5):27–30, 1991.

[35] R. Ding, Z.X. Guo, and A. Wilson. Microstructural evolution of a Ti-6Al-4V alloy during thermomechanical processing. *Materials Science and Engineering: A*, 327(2):233–245, 2002.

[36] F.P.E. Dunne and D. Rugg. On the mechanisms of fatigue facet nucleation in titanium alloys. *Fatigue & Fracture of Engineering Materials & Structures*, 31(11):949–958, 2008.

[37] F.P.E. Dunne, D. Rugg, and A. Walker. Lengthscale-dependent, elastically anisotropic, physically-based hcp crystal plasticity: Application to cold-dwell fatigue in Ti alloys. *International Journal of Plasticity*, 23(6):1061–1083, 2007.

[38] M.P. Echlin, A. Mottura, C.J. Torbet, and T.M. Pollock. A new TriBeam system for three-dimensional multimodal materials analysis. *Review of Scientific Instruments*, 83(2):023701, 2012.

[39] M.P. Echlin, J.C. Stinville, V.M. Miller, W.C. Lenthe, and T.M. Pollock. Incipient slip and long range plastic strain localization in microtextured Ti-6Al-4V titanium. *Acta Materialia*, 114:164–175, 2016.

[40] M.P. Echlin, M. Straw, S. Randolph, J. Filevich, and T.M. Pollock. The tribeam system: Femtosecond laser ablation in situ sem. *Materials Characterization*, 100:1–12, 2015.

[41] C. Efstathiou, D.E. Boyce, J.-S. Park, U. Lienert, P.R. Dawson, and M.P. Miller. A method for measuring single-crystal elastic moduli using high-energy x-ray diffraction and a crystal-based finite element model. *Acta Materialia*, 58(17):5806–5819, 2010.

[42] Z. Fan, Y. Wu, X. Zhao, and Y. Lu. Simulation of polycrystalline structure with voronoi diagram in laguerre geometry based on random closed packing of spheres. *Computational Materials Science*, 29:301–308, 2004.

[43] F.C. Frank. Orientation Mapping. *MRS Bulletin*, 13(03):24–31, 1988.

[44] M. G. Glavicic and V. Venkatesh. Integrated Computational Materials Engineering of Titanium: Current Capabilities Being Developed Under the Metals Affordability Initiative. *JOM*, 66(7):1310–1320, 2014.

[45] M.G. Glavicic, P.A. Kobryn, T.R. Bieler, and S.L. Semiatin. A method to determine the orientation of the high-temperature beta phase from measured EBSD data for the low-temperature alpha phase in Ti-6Al-4V. *Materials Science and Engineering: A*, 346(1-2):50–59, 2003.

[46] Michael A. Groeber and Michael A. Jackson. Dream.3d: A digital representation environment for the analysis of microstructure in 3d. *Integrating Materials and Manufacturing Innovation*, 3(1):5, 2014.

[47] M. Grujicic and Y. Zhang. Crystal plasticity analysis of stress–assisted martensitic transformation in Ti–10V–2Fe–3Al (wt.%). *Journal of Materials Science*, 35(18):4635–4647, 2000.

[48] S. Hanada and O. Izumi. Transmission electron microscopic observations of mechanical twinning in metastable beta titanium alloys. *Metallurgical Transactions A*, 17A:1409–1420, 1986.

[49] V. Hasija, S. Ghosh, M.J. Mills, and D.S. Joseph. Deformation and creep modeling in polycrystalline Ti-6Al alloys. *Acta Materialia*, 51(15):4533–4549, 2003.

[50] S. Hémery, A. Nait-Ali, and P. Villechaise. Combination of in-situ SEM tensile test and FFT-based crystal elasticity simulations of ti-6al-4v for an improved description of the onset of plastic slip. *Mechanics of Materials*, 109:1–10, 2017.

[51] W.F. Hosford. *The Mechanics of Crystals and Textured Polycrystals*. Number 32 in The Oxford engineering science series. Oxford University Press, New York, 1993.

[52] P. Van Houtte. Simulation of the rolling and shear texture of brass by the taylor theory adapted for mechanical twinning. *Acta Metallurgica*, 26(4):591–604, 1978.

[53] P.J.M. Janssen, Th.H. de Keijser, and M.G.D. Geers. An experimental assessment of grain size effects in the uniaxial straining of thin Al sheet with a few grains across the thickness. *Materials Science and Engineering: A*, 419(1-2):238–248, 2006.

[54] N. Jia, F. Roters, P. Eisenlohr, C. Kords, and D. Raabe. Non-crystallographic

shear banding in crystal plasticity FEM simulations: Example of texture evolution in α-brass. *Acta Materialia*, 60(3):1099–1115, 2012.

[55] S.G. Johnson. The NLopt nonlinear-optimization package. `http://ab-initio.mit.edu/nlopt`.

[56] I.P. Jones and W.B. Hutchinson. Stress-state dependence of slip in Titanium-6Al-4V and other H.C.P. metals. *Acta Materialia*, 23(9):951–968, 1981.

[57] T.-S. Jun, Z. Zhang, G. Sernicola, F.P.E. Dunne, and T.B. Britton. Local strain rate sensitivity of single α phase within a dual-phase ti alloy. *Acta Materialia*, 107:298–309, 2016.

[58] S.R. Kalidindi. Incorporation of deformation twinning in crystal plasticity models. *Journal of the Mechanics and Physics of Solids*, 46(2):267–290, 1998.

[59] S.R. Kalidindi, A.A. Salem, and R.D. Doherty. Role of deformation twinning on strain hardening in cubic and hexagonal polycrystalline metals. *Advanced Engineering Materials*, 5(4):229–232, 2003.

[60] M Kasemer, M.P. Echlin, J.C. Stinville, T.M. Pollock, and P. Dawson. On slip initiation in equiaxed α/β Ti-6Al-4V. *Acta Materialia*, 136:288–302, 2017.

[61] M. Kasemer, R. Quey, and P. Dawson. The influence of mechanical constraints introduced by β annealed microstructures on the yield strength and ductility of Ti-6Al-4V. *Journal of the Mechanics and Physics of Solids*, 103C:179–198, 2017.

[62] J.H. Keeler and A.H. Geisler. Preferred Orientations in Rolled and Annealed Titanium. *Journal of Metals*, 8:80–90, 1956.

[63] A Kelly and G.W. Groves. *Crystallography and Crystal Defects*. Prentice Hall, Reading, 1970.

[64] P. Klimanek and A. Pötzsch. Microstructure evolution under compressive plastic deformation of magnesium at different temperatures and strain rates. *Materials Science and Engineering: A*, 324(1-2):145–150, 2002.

[65] U. F. Kocks, C. N. Tomé, and H.R. Wenk. *Texture and anisotropy: preferred orientations in polycrystals and their effect on materials properties*. Cambridge Univ. Press, Cambridge, 1st edition, 2000.

[66] B. Kouchmeshky and N. Zabaras. Modeling the response of HCP polycrystals deforming by slip and twinning using a finite element representation of the orientation space. *Computational Materials Science*, 45(4):1043–1051, 2009.

[67] K. Kowalczyk-Gajewska. Modelling of texture evolution in metals accounting for lattice reorientation due to twinning. *European Journal of Mechanics - A/Solids*, 29(1):28–41, 2010.

[68] A. Kumar and P.R. Dawson. The simulation of texture evolution with finite elements over orientation space i. development. *Computer Methods in Applied Mechanics and Engineering*, 130(3-4):227–246, 1996.

[69] A. Kumar and P.R. Dawson. The simulation of texture evolution with finite elements over orientation space II. application to planar crystals. *Computer Methods in Applied Mechanics and Engineering*, 130(3-4):247–261, 1996.

[70] A. Kumar and P.R. Dawson. Modeling crystallographic texture evolution with finite elements over neo-Eulerian orientation spaces. *Computer Methods in Applied Mechanics and Engineering*, 153(3–4):259–302, 1998.

[71] M. Arul Kumar, I.J. Beyerlein, R.A. Lebensohn, and C.N. Tomé. Role of alloying elements on twin growth and twin transmission in magnesium alloys. *Materials Science and Engineering: A*, 706:295–303, 2017.

[72] J. Lévesque, K. Inal, K.W. Neale, and R.K. Mishra. Numerical modeling of formability of extruded magnesium alloy tubes. *International Journal of Plasticity*, 26(1):65–83, jan 2010.

[73] U. Lienert, S. F. Li, C. M. Hefferan, J. Lind, R. M. Suter, J. V. Bernier, N. R. Barton, M. C. Brandes, M. J. Mills, M. P. Miller, B. Jakobsen, and W. Pantleon. High-energy diffraction microscopy at the advanced photon source. *JOM*, 63(7):70–77, 2011.

[74] M. Lindroos, G. Cailletaud, A. Laukkanen, and V.-T. Kuokkala. Crystal plasticity modeling and characterization of the deformation twinning and strain hardening in hadfield steels. *Materials Science and Engineering: A*, 720:145–159, 2018.

[75] G. Lütjering and J.C. Williams. *Titanium*. Engineering Materials and Processes. Springer, Berlin; New York, 2nd edition, 2007.

[76] S. Mahajan and D. F. Williams. Deformation twinning in metals and alloys. *International Metallurgical Reviews*, 18(2):43–61, jun 1973.

[77] E.B. Marin and P.R. Dawson. Elastoplastic finite element analyses of metal deformations using polycrystal constitutive models. *Computer Methods in Applied Mechanics and Engineering*, 165(1–4):23–41, 1998.

[78] E.B. Marin and P.R. Dawson. On modelling the elasto-viscoplastic response of metals using polycrystal plasticity. *Computer Methods in Applied Mechanics and Engineering*, 165(1–4):1–21, 1998.

[79] W.T. Marketz, F.D. Fischer, and H. Clemens. Deformation mechanisms in TiAl intermetallics - experiments and modeling. *International Journal of Plasticity*, 19(3):281–321, 2003.

[80] J.R. Mayeur and D.L. McDowell. A three-dimensional crystal plasticity model for duplex Ti-6Al-4V. *International Journal of Plasticity*, 23(9):1066–1082, 2007.

[81] D.P. Mika and P.R. Dawson. Polycrystal plasticity modeling of intracrystalline boundary textures. *Acta Materialia*, 47(4):1355–1369, 1999.

[82] S. Myagchilov and P.R. Dawson. Evolution of texture in aggregates of crystals exhibiting both slip and twinning. *Modelling and Simulation in Materials Science and Engineering*, 7(6):975–1004, 1999.

[83] C.J. Neil and S.R. Agnew. Crystal plasticity-based forming limit prediction for non-cubic metals: Application to mg alloy AZ31b. *International Journal of Plasticity*, 25(3):379–398, 2009.

[84] J.F. Nye. *Physical Properties of Crystals: Their Representation by Tensors and Matrices*. Clarendon Press ; Oxford University Press, 1984.

[85] M. Obstalecki, S.L Wong, P.R. Dawson, and M.P. Miller. Quantitative analysis of crystal scale deformation heterogeneity during cyclic plasticity using high-energy X-ray diffraction and finite-element simulation. *Acta Materialia*, 75:259–272, 2014.

[86] R.W. Ogden. *Non-linear Elastic Deformations*. Dover Publications, 1997.

[87] D.C. Pagan, P.A. Shade, N.R. Barton, J.-S. Park, P. Kenesei, D.B. Menasche, and J.V. Bernier. Modeling slip system strength evolution in ti-7al informed by in-situ grain stress measurements. *Acta Materialia*, 128:406–417, 2017.

[88] M.J. Philippe, M. Serghat, P. Van Houtte, and C. Esling. Modelling of texture

evolution for materials of hexagonal symmetry - II. application to zirconium and titanium α or near α alloys. *Acta Metallurgica et Materialia*, 43(4):1619–1630, 1995.

[89] A. L. Pilchak, C. J. Szczepanski, J. A. Shaffer, A. A. Salem, and S. L. Semiatin. Characterization of Microstructure, Texture, and Microtexture in Near-Alpha Titanium Mill Products. *Metallurgical and Materials Transactions A*, 44(11):4881–4890, 2013.

[90] William H. Press. *Numerical Recipes in C: The Art of Scientific Computing, Second Edition*. Cambridge University Press, 1992.

[91] G. Proust, C.N. Tomé, and G.C. Kaschner. Modeling texture, twinning and hardening evolution during deformation of hexagonal materials. *Acta Materialia*, 55(6):2137–2148, 2007.

[92] R. Quey. Neper: polycrystal generation and meshing (version 3.0). `http://neper.sourceforge.net`, 2016.

[93] R. Quey, P.R. Dawson, and F. Barbe. Large-scale 3D random polycrystals for the finite element method: Generation, meshing and remeshing. *Computer Methods in Applied Mechanics and Engineering*, 200(17–20):1729–1745, 2011.

[94] R. Quey, M. Kasemer, and P. Dawson. Multiscale polycrystals for the finite element method: generation and meshing. *In preparation*, 2018.

[95] D. Raabe, Z. Zhao, and W. Mao. On the dependence of in-grain subdivision and deformation texture of aluminum on grain interaction. *Acta Materialia*, 50(17):4379–4394, 2002.

[96] V. Ramachandran, D.E. Baldwin, and R.E Reed-Hill. Tensile behavior of polycrystalline zirconium at 4.2°k. *Metallurgical Transactions*, 1:3011–3018, 1970.

[97] R.E. Reed-Hill. *Physical Metallurgy Principles*. Van Nostrand Reinhold Inc., U.S., 1967.

[98] L. Rémy. The interaction between slip and twinning systems and the influence of twinning on the mechanical behavior of fcc metals and alloys. *Metallurgical Transactions A*, 12(3):387–408, 1981.

[99] F. Roters, P. Eisenlohr, L. Hantcherli, D.D. Tjahjanto, T.R. Bieler, and D. Raabe. Overview of constitutive laws, kinematics, homogenization and multiscale meth-

ods in crystal plasticity finite-element modeling: Theory, experiments, applications. *Acta Materialia*, 58(4):1152–1211, 2010.

[100] D Rowenhorst, A D Rollett, G S Rohrer, M Groeber, M Jackson, P J Konijnenberg, and M De Graef. Consistent representations of and conversions between 3d rotations. *Modelling and Simulation in Materials Science and Engineering*, 23(8):083501, oct 2015.

[101] D.J. Rowenhorst, A.C. Lewis, and G. Spanos. Three-dimensional analysis of grain topology and interface curvature in a β-titanium alloy. *Acta Materialia*, 58:5511–5519, 2010.

[102] A. A. Salem, S. R. Kalidindi, R. D. Doherty, and S. L. Semiatin. Strain hardening due to deformation twinning in α-titanium: Mechanisms. *Metallurgical and Materials Transactions A*, 37(1):259–268, 2006.

[103] A.A. Salem, S.R. Kalidindi, and S.L. Semiatin. Strain hardening due to deformation twinning in α-titanium: Constitutive relations and crystal-plasticity modeling. *Acta Materialia*, 53(12):3495–3502, 2005.

[104] G.B. Sarma and P.R. Dawson. Effects of interactions among crystals on the inhomogeneous deformations of polycrystals. *Acta Materialia*, 44(5):1937–1953, 1996.

[105] MF Savage, J Tatalovich, and MJ Mills. Anisotropy in the room-temperature deformation of α–β colonies in titanium alloys: role of the α–β interface. *Philosophical Magazine*, 84(11):1127–1154, 2004.

[106] E. Schmid and W. Boas. *Plasticity of Crystals with Special Reference to Metals*. Chapman & Hall, 1968.

[107] S. L. Semiatin, S. L. Knisley, P. N. Fagin, D. R. Barker, and F. Zhang. Microstructure evolution during alpha-beta heat treatment of Ti-6Al-4V. *Metallurgical and Materials Transactions A*, 34(10):2377–2386, 2003.

[108] Y.F. Shen, N. Jia, Y.D. Wang, X. Sun, L. Zuo, and D. Raabe. Suppression of twinning and phase transformation in an ultrafine grained 2gpa strong metastable austenitic steel: Experiment and simulation. *Acta Materialia*, 97:305–315, 2015.

[109] M. Shiekhelsouk, V. Favier, and M. Inal, K.and Cherkaoui. Modelling the behaviour of polycrystalline austenitic steel with twinning-induced plasticity effect. *International Journal of Plasticity*, 25(1):105–133, 2009.

[110] R.P. Singh and R.D. Doherty. Strengthening in MULTIPHASE (MP35n) alloy: Part i. ambient temperature deformation and recrystallization. *Metallurgical Transactions A*, 23(1):307–319, 1992.

[111] Xu Song, Shu Yan Zhang, Daniele Dini, and Alexander M. Korsunsky. Finite element modelling and diffraction measurement of elastic strains during tensile deformation of HCP polycrystals. *Computational Materials Science*, 44(1):131–137, 2008.

[112] A. Spettl, T. Werz, C.E. Krill, and V. Schmidt. Parametric representation of 3d grain ensembles in polycrystalline microstructures. *Journal of Statistical Physics*, 154:913–928, 2014.

[113] A. Staroselsky and L. Anand. Inelastic deformation of polycrystalline face centered cubic materials by slip and twinning. *Journal of the Mechanics and Physics of Solids*, 46(4):671–696, 1998.

[114] J.C. Stinville, F. Bridier, D. Ponsen, P. Wanjara, and P. Bocher. High and low cycle fatigue behavior of linear friction welded Ti-6Al-4V. *International Journal of Fatigue*, 70:278–288, 2015.

[115] J.C. Stinville, M.P. Echlin, D. Texier, F. Bridier, P. Bocher, and T.M. Pollock. Sub-grain scale digital image correlation by electron microscopy for polycrystalline materials during elastic and plastic deformation. *Experimental Mechanics*, 56(2):197–216, 2016.

[116] Gilbert Strang. *Computational Science and Engineering*. Wellesley-Cambridge Press, 2007.

[117] S Suri, GB Viswanathan, T Neeraj, D-H Hou, and MJ Mills. Room temperature deformation and mechanisms of slip transmission in oriented single-colony crystals of an α/β titanium alloy. *Acta Materialia*, 47(3):1019–1034, 1999.

[118] C. Tomé and U.F. Kocks. The yield surface of h.c.p. crystals. *Acta Metallurgica*, 33(4):603–621, 1985.

[119] C.N. Tomé, R.A. Lebensohn, and U.F. Kocks. A model for texture development dominated by deformation twinning: Application to zirconium alloys. *Acta Metallurgica et Materialia*, 39(11):2667–2680, 1991.

[120] T Ungár. Microstructural parameters from x-ray diffraction peak broadening. *Scripta Materialia*, 51(8):777–781, 2004.

[121] T. Ungár, M.G. Glavicic, L. Balogh, K. Nyilas, A.A. Salem, G. Ribárik, and S.L. Semiatin. The use of x-ray diffraction to determine slip and twinning activity in commercial-purity (CP) titanium. *Materials Science and Engineering: A*, 493(1-2):79–85, 2008.

[122] L. Wang, R. Barabash, T. Bieler, W. Liu, and P. Eisenlohr. Study of $\{1\,1\,\overline{2}\,1\}$ twinning in α-ti by EBSD and laue microdiffraction. *Metallurgical and Materials Transactions A*, 44(8):3664–3674, 2013.

[123] L. Wang, J. Lind, H. Phukan, P. Kenesei, J.-S. Park, R.M. Suter, A.J. Beaudoin, and T.R. Bieler. Mechanical twinning and detwinning in pure ti during loading and unloading - an in situ high-energy x-ray diffraction microscopy study. *Scripta Materialia*, 92:35–38, 2014.

[124] L. Wang, Y. Yang, P. Eisenlohr, T.R. Bieler, M.A. Crimp, and D.E. Mason. Twin nucleation by slip transfer across grain boundaries in commercial purity titanium. *Metallurgical and Materials Transactions A*, 41(2):421–430, 2009.

[125] O. Watanabe, H.M. Zbib, and E. Takenouchi. Crystal plasticity: micro-shear banding in polycrystals using voronoi tessellation. *International Journal of Plasticity*, 14(8):771–788, 1998.

[126] E. Wielewski, D.E. Boyce, J.-S. Park, M.P. Miller, and P.R. Dawson. A methodology to determine the elastic moduli of crystals by matching experimental and simulated lattice strain pole figures using discrete harmonics. *Acta Materialia*, 126:469–480, 2017.

[127] E. Wielewski, D.B. Menasche, P.G. Callahan, and R.M. Suter. Three-dimensional α colony characterization and prior-β grain reconstruction of a lamellar Ti-6Al-4V specimen using near-field high-energy X-ray diffraction microscopy. *Journal of Applied Crystallography*, 48(4):1165–1171, 2015.

[128] J. C. Williams, R. G. Baggerly, and N. E. Paton. Deformation behavior of HCP Ti-Al alloy single crystals. *Metallurgical and Materials Transactions A*, 33(3):837–850, 2002.

[129] S.L. Wong and P.R. Dawson. Influence of directional strength-to-stiffness on the elastic-plastic transition of fcc polycrystals under uniaxial tensile loading. *Acta Materialia*, 58(5):1658–1678, 2010.

[130] S.L. Wong, M. Madivala, U. Prahl, F. Roters, and D. Raabe. A crystal plasticity model for twinning- and transformation-induced plasticity. *Acta Materialia*, 118:140–151, 2016.

[131] S.L. Wong, M. Obstalecki, M.P. Miller, and P.R. Dawson. Stress and deformation heterogeneity in individual grains within polycrystals subjected to fully reversed cyclic loading. *Journal of the Mechanics and Physics of Solids*, 79:157–185, 2015.

[132] S.L. Wong, J.-S. Park, M.P. Miller, and P.R. Dawson. A framework for generating synthetic diffraction images from deforming polycrystals using crystal-based finite element formulations. *Computational Materials Science*, 77:456–466, 2013.

[133] P.D. Wu, S.R. MacEwen, D.J. Lloyd, and K.W. Neale. Effect of cube texture on sheet metal formability. *Materials Science and Engineering: A*, 364(1-2):182–187, 2004.

[134] X. Wu, S. Kalidindi, C. Necker, and A. Salem. Prediction of crystallographic texture evolution and anisotropic stress–strain curves during large plastic strains in high purity α-titanium using a taylor-type crystal plasticity model. *Acta Materialia*, 55(2):423–432, 2007.

[135] X.L. Wu, K.M. Youssef, C.C. Koch, S.N. Mathaudhu, L.J. Kecskés, and Y.T. Zhu. Deformation twinning in a nanocrystalline hcp mg alloy. *Scripta Materialia*, 64(3):213–216, 2011.

[136] Y. Yang, L. Wang, C. Zambaldi, P. Eisenlohr, R. Barabash, W. Liu, M. R. Stoudt, M. A. Crimp, and T. R. Bieler. Characterization and modeling of heterogeneous deformation in commercial purity titanium. *JOM*, 63(9):66–73, 2011.

[137] M. Zhang, J. Zhang, and D.L. McDowell. Microstructure-based crystal plasticity modeling of cyclic deformation of Ti-6Al-4V. *International Journal of Plasticity*, 23(8):1328–1348, 2007.

[138] S.V. Zherebtsov, G.S. Dyakonov, A.A. Salem, S.P. Malysheva, G.A. Salishchev, and S.L. Semiatin. Evolution of grain and subgrain structure during cold rolling of commercial-purity titanium. *Materials Science and Engineering: A*, 528(9):3474–3479, 2011.